ABSTRACT

Statistical, Random and Fractal Characterizations of Surface Topography with Engineering Applications

by
Gongyao Zhou

Two methods, namely the conventional and fractal geometry methods, are developed for surface topography characterization. The conventional method utilizing statistical and random process techniques is used to study waterjet machined surfaces. In the study the waterjet surfaces are separated into smooth and striation zones, where striation influence is negligible in the smooth zone. It is found that the smooth zone has a random, moderately isotropic texture, with the height distribution nearly Gaussian. In the striation zone the major frequencies of the surface profile power spectra are independent of cutting parameters, while the amplitudes of these frequencies monotonically increase with cutting speed or depth of cut. The effects of cutting speed, depth of cut, orifice diameter, and abrasive size on the surface topography are also studied. This provides useful information for controlling process parameters to obtain smooth finished surfaces. The spectral analysis is used to investigate the structure dynamics of the waterjet machining system. It is found that the vibration of the abrasive waterjet machining system plays an important role in the striation formation.

Manufactured surfaces which have random texture, such as those produced by electrical discharge machining, waterjet cutting, and ion-nitriding coating, can be characterized by fractal geometry. A

Gaussian random fractal model coupled with structure functions is used to relate surface topography with fractal geometry via fractal dimension (D) and topothesy (L). This fractal characterization of surface topography complements and improves the conventional statistical and random process methods of surface characterization, especially in the study of contact mechanics and wear processes. The Gaussian fractal model for surface topography is shown to predict a primary relationship between D and the bearing area curve, while L affects this curve to a smaller degree. Several experiments are performed, and the results support the predicted effects of D and L on the bearing area curve.

Fractal characterization of surface topography is further applied to the study of contact mechanics and wear processes. A fractal geometry model is developed, which predicts the wear rate in terms of fractal parameters D and L for wear prediction. This model shows that the wear rate V_r and the true contact area A_r have the relationship $V_r \propto (A_r)^{m(D)}$, where m(D) is a function of D and has a value between 0.5 and 1. Next the optimum (i.e. the lowest wear rate) fractal dimension in a wear process is studied. It is found that the optimum fractal dimension is affected by contact area, material properties, and scale amplitude. Experimental results of wear testing show good agreement with the predictions based on the model.

STATISTICAL, RANDOM AND FRACTAL CHARACTERIZATIONS OF SURFACE TOPOGRAPHY WITH ENGINEERING APPLICATIONS

by

Gongyao Zhou

A Dissertation
Submitted to the Faculty of
New Jersey Institute of Technology
in Partial Fulfillment of the Requirements for the Degree of
Doctor of Philosophy

Department of Mechanical and Industrial Engineering

January, 1993

APPROVAL PAGE

Statistical Random and Fractal Characterizations of Surface Topography with Engineering Applications

by

Gongyao Zhou

Dr. Ming C. Leu, Dissertation Adviser

Professor, Department of Mechanical and Industrial Engineering, NJIT

Dr. D. Blackmore, Dissertation Co-Adviser

Professor, Department of Mathematics, NJIT

Dr. E. Geskin, Committee Member

Professor, Department of Mechanical and Industrial Engineering, NJIT

Dr. N. Levy, Committee Member

Associate Professor, Department of Mechanical and Industry Engineering, NJIT

Dr. Z. Ji, Committee Member

Assistant Professor, Department of Mechanical and Industrial Engineering, NJIT

BIOGRAPHICAL SKETCH

Author: Gongyao Zhou

Degree: Doctor of Philosophy in Mechanical Engineering

Undergraduate and Graduate Education:

- Doctor of Philosophy in Mechanical and Industrial Engineering, New Jersey Institute of Technology, Newark, NJ, 1992
- Master of Science in Mechanical Engineering, Xi'an Jiaotong University, Xi'an, P. R. China
- Bachelor of Science in Mechanical Engineering, Xi'an Jiaotong University, Xi'an, P. R. China

Major: Mechanical and Industrial Engineering

Presentations and Publications:

Zhou, G., M. Leu, E. Geskin, Y. Chung, and J. Chao "Investigation of Topography of Waterjet Generated Surfaces," Proceedings of the 1992 ASME Winter Annual Meeting, Anaheim, California.

Chao, J., G. Zhou, M. Leu, and E. Geskin "Characteristics of Abrasive Waterjet Generated Surfaces and Effects of Cutting Parameters and Structure Vibration." Submitted to the ASME Journal of Engineering for Industry, October 1992

Zhou, G., M. Leu, and D. Blackmore "Fractal Geometry Model for Wear Prediction." Submitted to International Journal of Wear, September 1992.

Zhou, G., M. Leu, and D. Blackmore "Fractal Characterization of Surface Topography and Implementation in Surface Contact." Submitted to ASME Journal of Tribology, July 1992.

Zhou, G., M. Leu, and S. Dong "Measurement and Assessment of Topography of Machined Surfaces." Proceedings of the ASME

Winter Annual Meeting, Dallas, Texas, November, 1990.

Park, Y., M. Leu, and G. Zhou "Macintosh IIx and IBM PC Based Automatic Control Laboratory." Journal of Computers in Education, Division of ASEE, Vol. X, No. 3, July-Sep., 1990.

Zhou, G., and Y. Park "Study of Servo Motor Control System." Instruction Manual for a Laboratory Course, Mechanical Engineering Department of NJIT, September 1989.

This dissertation is dedicated to

my wife Yan Shi, my son David Zhou, and my family

ACKNOWLEDGEMENT

The author first takes this opportunity to thank his adviser, Professor Ming C. Leu, for his continuous support and guidance. Professor Leu's insisting "find something new" and "always stand at the forefront of a research field" led the author to the fulfillment of his doctoral research. Professor Leu's constructive criticism and spirit of never giving up pushed the author to achieve at a level that was more than he imagined possible.

The author will never forget the great help which he received from his co-adviser, Professor Denis Blackmore. He is extremely intelligent and knowledgeable not only in his field of mathematics but also in applications of mathematics to engineering and science. In addition to general guidance, he also provided concrete advice and deep discussions. He is an excellent advisor and a good new friend.

Special thanks to Professor E. Geskin for introducing the author to the field of waterjet machining, and for being so helpful to the author in writing papers and reading his thesis.

The author sincerely thanks Dr. T. Vorburger, an expert in surface engineering and precision measurement. In the course of many helpful discussions he provided good advice. He also provided the experimental facilities which the author needed .

Thanks to Professors B. Koplik, J. Droughton, H. Herman, R. Chen, and R. Dubrovsky, for their support and help. Thanks also to Professors N. Levy and Z. Ji for reviewing this thesis, and to Mrs. Marcia Eddings for her kindness and good wishes.

The author wants to give special thanks to Mr. J. Chao. We had

a very good time and made great progress in cooperating with each other in the study of waterjet machining processes. He provided the author with the experimental data and figures for section 2.6 of chapter 2 of this dissertation.

The author, in his four-year doctoral study, had a good time associating with his fellow students. With them he had a lot of fun, and from them he learned many things. The author thanks H. Wong, I. Shih, J. Chao, Y. Chung, Z. Zhang, Ning Li, Q. Kim and K. Pak.

It is hard for the author to fully express his gratitude to his family: his wife Yan Shi and his son David. Their encouragement, help and love supported the author through many struggles and difficult times during his four-year doctoral study. In recognition, the author dedicate this thesis to them.

Finally the author would like to thank his mother and brother. Although they are far away from here, their support and best wishes warm his heart all the time.

TABLE OF CONTENTS

Chapter **Page**

Chapter Page

Chapter Page

LIST OF TABLES

LIST OF FIGURES

Figure Page

Figure Page

Figure Page

LIST OF SYMBOLS

A	area size of a island
A_a	apparent contact area
A_c	true contact area
A_r	total area of islands
A_r^*	normalized true contact area
A_{re}	elastic contact area
A_{rp}	plastic contact area
$B(\hat{z})$	normalized bearing area ratio
$B(t)$	Brownian motion distance
C, C_i	constants
c_i	constants
D	fractal dimension
d	wear distance
E	elastic modulus
G	scale amplitude
G^*	normalized scale amplitude
g	a constant
H	hardness
I_i	invariants composed by PSD moments
K	wear coefficient
K_e	elastic wear coefficient
K_p	plastic wear coefficient
L	Topothesy
L_i	length sequence of a fractal set
M	magnification of length for fractal set

M_i the ith order PSD moments

m mean of a Gaussian distribution

N number of segments in a fractal set

P( ) probability function

p flow pressure under normal and tangential stresses

p_m flow pressure under static load

Q material property factor

R_a average surface height

R_q root-mean-square surface height

R_{sk} skewness of surface height

R_{ku} kurtosis of surface height

S measuring area

$S(\omega)$ power spectrum

S_L area of the largest island

S_c critical area for distinguishing elastic and plastic deformation

s shear strength

T total friction force

V wear volume

V* normalized wear rate

V_r wear rate

W load

α a parameter related with fractal dimension D

β slope of equation (3.11)

ϕ a profile function

ψ material constant

λ displacement

μ friction coefficient

σ_y yield strength

ω round frequency

$\Phi( )$ a surface function

CHAPTER 1
INTRODUCTION

Tribology is a multi-disciplinary science which involves the study of interfacial actions in friction, lubrication, and wear phenomena. The importance of tribology for economic savings in modern technological development is now universally realized. The applications of tribology knowledge have been widespread in the such fields as material science, machinery design, biomedical engineering, space engineering, and electromagnetic information storage mechanisms (Jost 1990; Bhushan 1991). Characterization and analysis of surface topography play a crucial role in tribology.

The methodology of surface measurement and evaluation has been developed for more than 50 years. In the last half century, with the rapid development of precision instruments and measurements, and the emergence of a large amount of new technologies, it has become clear that surface characterization and analysis are not only important in tribology but also in the study of thermal and electrical conductance, optical scattering, electromagnetic radiation, superconductivity etc. Roughly speaking, surface measurement and evaluation have undergone four stages of development: the original single-point measurement method (for example, peak-to-valley height); statistical method (for example, arithmetic average height, root-mean-square height, and autocorrelation function); random process method (for example, power spectrum density moments, mean surface slope and curvature); and the recently developed fractal geometry method (for example, fractal dimension and

topothesy).

This thesis focuses on the methodology used in the study of surface topography characterization and modeling, the functional relationships between surfaces and manufacturing processes, and engineering applications of the methodology in tribology science.

There are two major parts in the thesis. In the first part, a three-dimensional surface evaluation system based on statistical and random process methods is introduced. A specific kind of waterjet generated surface is evaluated. The effects of cutting parameters and structure dynamics on abrasive waterjet (AWJ) generated surfaces are investigated. This study provides useful information in surface quality and manufacturing process control of waterjet machined surfaces.

The statistical and random process methods have some shortcomings in the surface topography study. It has been found that manufactured random surfaces have a multi-scale property and they are fractal (Jordan, Hollins, and Jakeman 1986). These findings imply that random surfaces are non-stationary (Sales and Thomas 1978), non-differentiable (Berry 1980), and the measured parameter values are instrument dependent (Majumdar and Bhushan 1990). These properties have a significant effect on quantitative analysis and evaluations of surfaces. Fractal geometry does not have the above shortcomings and it has great advantages in characterizing surface contact support ability and in modeling of wear mechanism. This is a main topic of part two, the major emphasis of this thesis, where fractal geometry is implemented in surface topography characterization, wear prediction modeling, and wear process testing.

The structure of this thesis is as follows. Chapter 2 applies the statistical and random process methods to a specific kind of surface: waterjet generated surfaces. Several classification and evaluation methods for surface topography are introduced. The principles and technology of waterjet machining and the striation phenomenon are described. Waterjet machined surfaces are evaluated by separating the surfaces into smooth and striation zones. The study is then expanded to include the effects of cutting parameters and structure dynamics on waterjet generated surfaces.

As an introduction to fractal geometry, chapter 3 presents a general description of fractals and explains some basic concepts such as self-similar fractals, self-affine fractals, and fractal dimension. Techniques developed for determining fractal dimensions are discussed. It is observed that the structure function method is very useful as a tool for obtaining fractal dimension and topothesy for fractal sets.

In chapter 4 a Gaussian random fractal model for surface topography characterization is proposed. Based on this model it is found that fractal geometry is directly related to the bearing area curve. Because fractal geometry is a quantitative and concise expression of surface contact support ability, it is possible to use fractal parameters to replace traditional bearing area curves. Experimental results shown agree with the analytical results based on this model.

Since fractal geometry can be used to characterize surface contact support ability, it is practical to apply this method to wear. This is discussed in chapter 5. The fractal property of islands is used

to simulate a real random surface, and the fractal relation of contact asperities is found. Based on the adhesive wear theory a wear prediction model is developed using fractals, and in terms of this model the effects of fractal parameters on wear rate are analyzed. The optimum fractal dimension in wear processes is discussed. The fractal method is implemented in a wear testing process and the results qualitatively support the wear prediction model. Chapter 6 contains conclusions and suggested future work.

CHAPTER 2

CHARACTERISTICS OF ABRASIVE WATERJET GENERATED SURFACES AND EFFECTS OF CUTTING PARAMETERS AND STRUCTURE VIBRATION

2.1 Introduction

Abrasive waterjet (AWJ) machining is an emerging technology which enables the shaping of practically all existing engineering materials. Due to the advantages of AWJ machining such as fast cutting speed, no heat effect zone, and ability to cut harder materials, it has been widely used in many industrial applications. Like other high energy beam cuttings, AWJ cutting has the defect of leaving striation marks on the cut surface. This significantly affects the dimensional accuracy and surface finish. The striation marks on the surface can be improved by adjusting the jet entrance angle (Matsui et al., 1990), slowing down the cutting speed, and using multi-passes cutting (Souda, 1991). However these are not efficient ways and striation can not be eliminated completely. For fully understanding the processes of AWJ machining and seeking a way to enhance dimensional accuracy and surface finish, it is essential to study the characteristics of AWJ generated surfaces.

The topography of AWJ generated surfaces has been studied by several researchers. Based on a flow visualization study of waterjet cutting process, Hashish (1984, 1991), proposed that the waterjet erosion process consists of two cutting regimes. The first regime (on the top of the kerf) is dominated by the cutting wear mode where

penetration occurs in a small impact angle. The second regime (on the bottom of the kerf) is dominated by the deformation wear mode where penetration occurs in a large impact angle. The surface is smooth in the first regime but is marked by striations in the second regime. Based on this study, Tan (1986) suggested a model based on the kinematics/geometry of the cutting process to explain the characteristics of striated surfaces. He showed the modeled results to be in good agreement with experimentally obtained data. Hunt, Kim and Reuber (1988), in conducting an experimental study for AWJ cut metal surfaces involving striations, observed that the surface roughness increases monotonically with increase in depth of cut or cutting speed and that a linear relationship correlates them very well. A similar conclusion was made by Neusen, et al. (1987) in the cutting of metal matrix composites. Kovacevic (1991) used a second-order mathematical model to characterize the surface roughness as a function of several AWJ operation parameters across the entire cut's depth.

Despite the common observation that an AWJ cut surface may consist of two zones of different texture: a smooth zone near the top of the cut and a rough striation zone below some depth from the top, researchers have not studied the texture of a surface in the smooth zone and how it differs from the texture of a surface in the striation zone.

In this chapter we present an experimental study of the topography of AWJ generated surfaces such that we are able to reveal the distinct difference in surface texture between the smooth zone and the striation zone. It is found that the smooth zone has a

homogeneous, random, Gaussian, and moderately isotropic texture. The surface roughness parameters R_a and R_q in this zone depend weakly on depth of cut, cutting speed, and orifice diameter, although they increase monotonically with increasing abrasive particle size. In contrast, the surface roughness and the amplitude of power spectrum in the striation zone increases strongly with increasing depth of cut or cutting speed.

Hashish (1991,1992) presented his recent study of the general characteristics of AWJ machined surfaces. He proposed that there are two types of waviness in AWJ machined surfaces. The first type of waviness is the jet-induced waviness, which exists on the surface dominated by the deformation wear mode. The second type of waviness is the traverse-induced waviness, which may appear in both the cutting and deformation wear zones. In Harshish's paper he also mentioned that some dynamic factors and vibration may be the causes of striation formation. However these causes remain somewhat a conjecture, as pointed out by himself that no quantitative data are available.

In this chapter we shall present a detailed study of the structure dynamics of our AWJ machine to find out the role of the vibration of the AWJ machining system in striation formation.

2.2 Evaluation of Surface Topography

2.2.1 Classification of Surfaces

Classification of surfaces can be done as depicted in Figure 2-1 (Nayak, 1971; Zhou, Leu, and Dong, 1990). Surfaces of solids can be

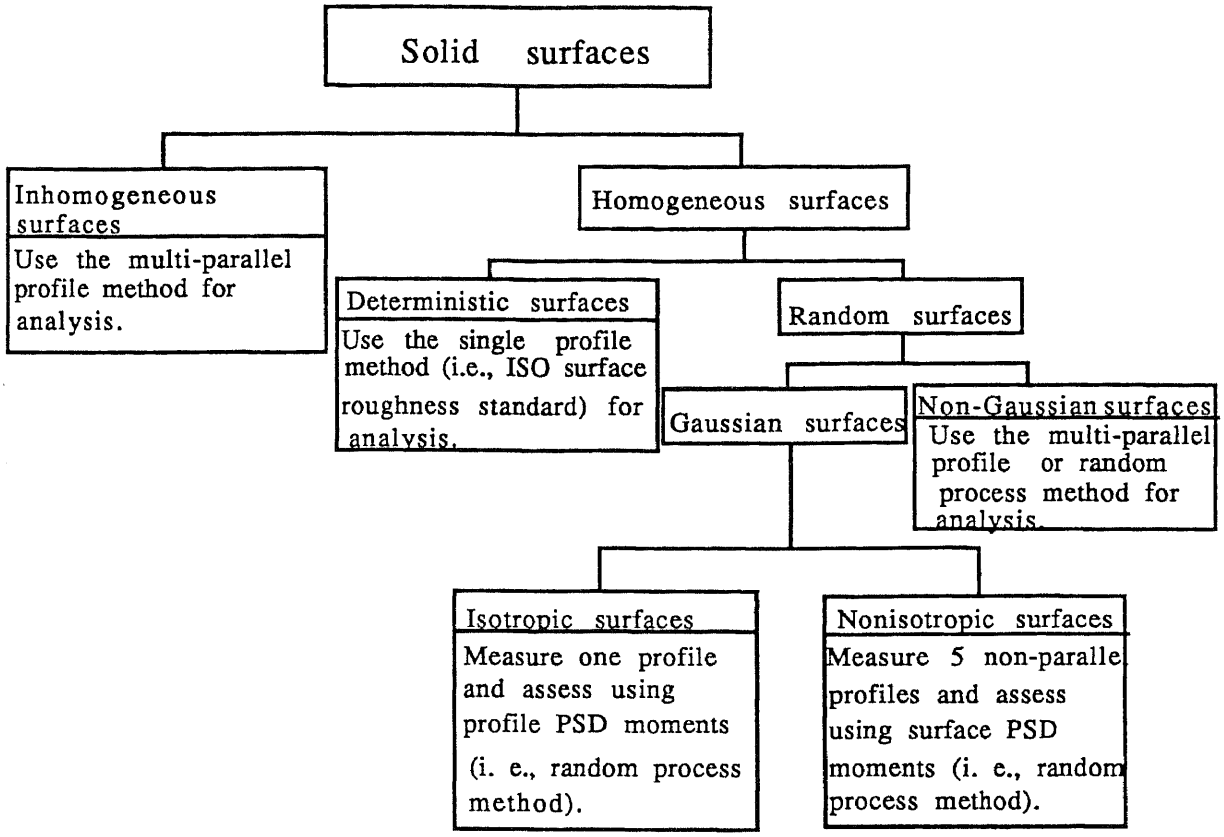

Figure 2-1 Classification and assessment of solid surfaces

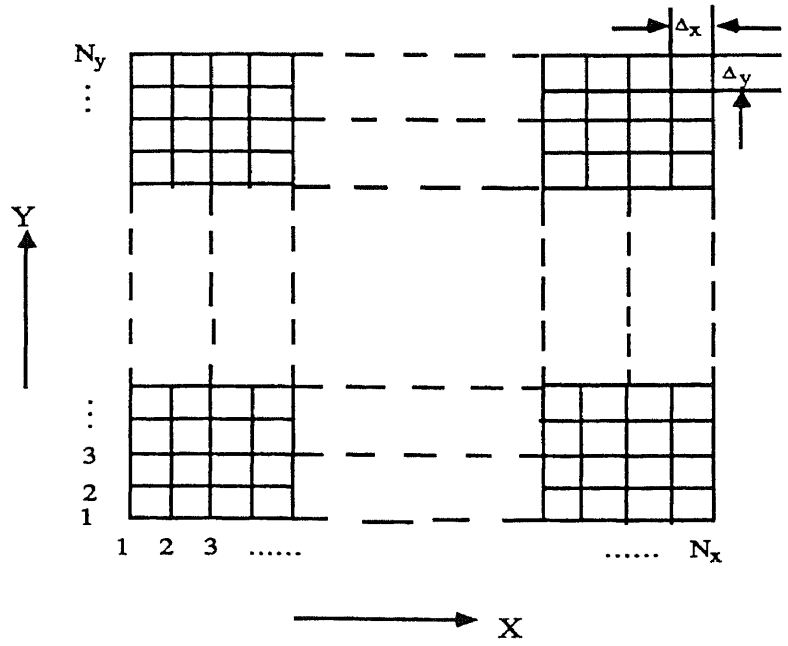

Figure 2-2 Sampling grids for the multi-parallel profile method

divided into homogeneous and inhomogeneous surfaces. For homogeneous surfaces the statistical properties of surface texture are invariant with respect to translation of surface of examination. Homogeneous surfaces can be separated into deterministic and random surfaces. The texture of deterministic surfaces has strong periodicities. The method of measuring and assessing deterministic surfaces are described in the ISO standard of surface roughness (1966). The current surface evaluation practice is often based on the assumption that a surface in question is homogeneous and deterministic.

Random surfaces can be further divided into Gaussian and non-Gaussian surfaces based on the distribution of surface heights (Thomas, 1982b). Gaussian surfaces can be isotropic or nonisotropic. If the statistical characteristics of surface texture are invariant to direction of surface profile measurement, the surface is termed isotropic. For Gaussian isotropic surfaces, it suffices to measure one profile and use its power spectral density (PSD) moments to assess the whole surface (Longuet-Higgins, 1957; Nayak, 1971). For Gaussian nonisotropic surfaces, several non-parallel profiles should be sampled and their PSD moments used for assessment (Longuet-Higgins, 1962; Nayak, 1973).

To classify an unknown surface the following procedure can be used. First, single-profile measurements can be made on different locations of the surface to identify surface homogeneity. For inhomogeneous surfaces, a multi-parallel profile method can be used for evaluation. Autocorrelation functions can be obtained for further

examination of homogeneous surfaces (Peklenik, 1967). If the surface is random, the next test is to evaluate height distribution. If this evaluation shows that the height distribution is Gaussian, the next step is to evaluate whether the surface is isotropic or nonisotropic.

2.2.2 Methods of Surface Topography Evaluation

2.2.2.1 Surface Parameters

The multi-parallel profile method constitutes the extension of the conventional 2-D profile measurement technique (American National Standard, 1985) to 3-D surface texture measurement. Essentially, dense parallel profiles are obtained for evaluating the surface texture. The sampling grid pattern for the multi-parallel profile method is illustrated in Figure 2-2. The probe of a profilometer traverses along the X direction to obtain a profile and returns to the starting point. It is then displaced Δy along the Y direction before measuring the second profile, and so on. In Figure 2, N_X is the number of sampling points on each profile, N_y is the number of sampled profiles on the surface, Δx is the sampling interval in X direction. Once the data array has been obtained, various surface parameters can be computed for the surface evaluation.

The first step in computing surface parameters involves the identification of a reference plane for a surface under evaluation. The least square technique can be used for identifying this plane. After the reference plane (Ax+By+C) has been identified, the surface height $\underline{Z}(x, y)$ can be expressed relative to this plane as

$$Z(x, y) = \underline{Z}(x, y) - (Ax + By + C) \tag{2.1}$$

The obtained Z(x, y) data allow determining all the surface roughness parameters as in the 2-dimensional case involving single profiles. The following four surface roughness parameters will be used in this study.

1) Average surface height

$$R_a = \frac{1}{S} \int \int |Z(x, y)| dxdy \tag{2.2}$$

where S is the surface area of concern.

2) Root-mean-square surface height

$$R_q = \left(\frac{1}{S} \int \int (Z(x,y))^2 \, dxdy\right)^{1/2} \tag{2.3}$$

3) Skewness

$$R_{sk} = \frac{1}{S R_q^3} \int \int (Z(x,y))^3 dxdy \tag{2.4}$$

4) Kurtosis

$$R_{ku} = \frac{1}{S R_q^4} \int \int (Z(x,y))^4 dxdy \tag{2.5}$$

2.2.2.2 Isotropy Identification

There exist methods for identifying surface isotropy. Nayak (1973) proposed the γ criterion

$$\gamma = \left(\frac{I_2 - (I_2^2 - 4I_3)^{1/2}}{I_2 + (I_2^2 - 4I_3)^{1/2}} \right)^{1/2} \qquad 0 \le \gamma \le 1 \qquad (2.6)$$

where I_2 and I_3 are statistical invariants which are composed by second-order power spectrum density (PSD) moments (see Appendix A). For an isotropic surface, $\gamma = 1$. For a surface whose profiles have very long crests, $\gamma = 0$. Sayles and Thomas (1979) proposed the following alternate formula:

$$\gamma' = \sqrt{\frac{M_{2min}}{M_{2max}}} \qquad 0 \le \gamma' \le 1 \qquad (2.7)$$

where M_{2min} and M_{2max} are the minimum and maximum second-order PSD moments. The autocorrelation function (Kubo and Peklenik, 1968) and spatial spectrum (Majumdar and Bhushan, 1990) analyses could also be used for isotropy identification, but they can only provide qualitative characterization.

2.3 Waterjet Cutting Technology

2.3.1 Principle of Waterjet Machining

Waterjet cutting involves the compression of water to an extremely high pressure (up to 379.5 MPa) and subsequently forcing the water through a small orifice (0.1016 to 0.508 mm in diameter) to impact on the workpiece at a velocity which may approach 750 meters per second. The water stream causes rapid erosion of the workpiece and generates a kerf slightly wider than the orifice diameter. The effective power of the water stream is determined by the water pressure and orifice diameter. By adding a granulated abrasive material to the focused water stream, the ability of the stream to erode hard and high-density materials is greatly enhanced. A schematic diagram of AWJ system is given in Figure 2-3.

2.3.2 Striation Phenomenon

A specific feature of AWJ cutting is the formation of striation marks below a relatively smooth area on the machined surface. Figure 2-4. shows that the AWJ generated surface may contain two main zones: a comparatively homogeneous upper zone, a lower zone containing continuously increasing striation marks. Similar complexity in surface texture has been observed on surfaces generated by other manufacturing methods such as by a laser beam (King and Powell, 1986). Significant striation lines appear when the ratio of the available energy of jet to the required energy of material destruction drops below a critical value. This ratio depends on the cutting speed, depth of cut, flow rate and particle velocity. The amplitude of striation marks increases as the distance of cut increases.

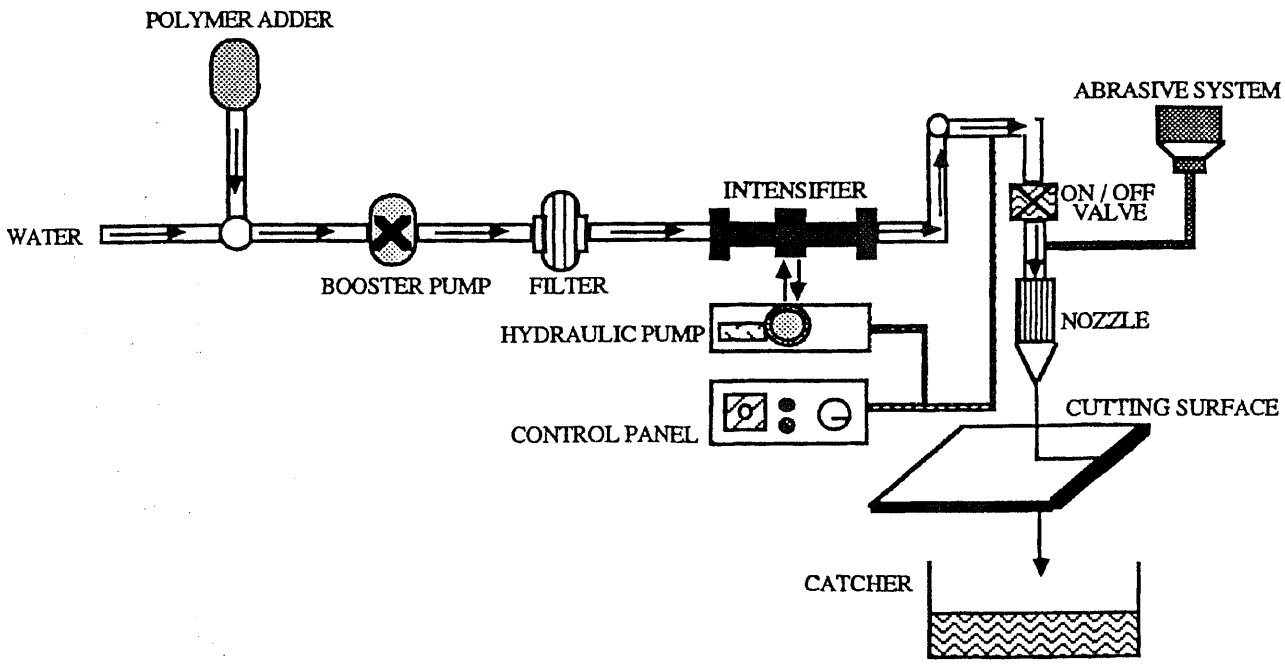

Figure 2-3 Schematic of abrasive waterjet cutting

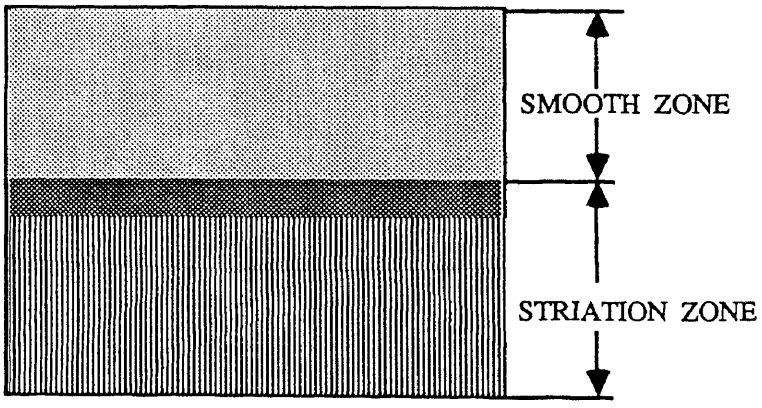

Figure 2-4 Two zones of AWJ cut surface

2.4 Evaluation of Waterjet Generated Surfaces

2.4.1 Characterization of Surface Topography in Smooth Zone

The Ingersoll Rand Streamline waterjet cutting system was used in the experiment. Six workpieces were investigated after having been machined. Their manufacturing specifications are listed in Table 2-1. The system for measuring surface topography is shown in Figure 2-5. The textures of the machined surfaces are shown in Figure 2-6.

We first evaluated the homogeneity of the generated surfaces. The variation in R_a and R_q in different areas of the surface revealed the existence of homogeneous (smooth) and inhomogeneous (striation) regions.

The second step was to evaluate the stochastic property of the smooth, homogeneous region of the surface. The autocorrelation functions of the surface profiles measured in 0° (parallel to the moving direction of the cutting head) and 90° are shown in Figure 2-7. For all of the measured profiles the autocorrelation function decreases from 1 to 0 rapidly with increase in correlation length λ and then oscillates around the X axis. This indicates that the texture of the smooth part of the surface is dominantly random.

The third step involved evaluating whether the random surface is Gaussian or not. The ideal Gaussian surface's probability distribution graph has a bell shape with the skewness equal to zero and kurtosis equal to three. The graphs obtained as shown in Figure 2-8 (a) to (f) indicate that for practical purposes the studied surfaces

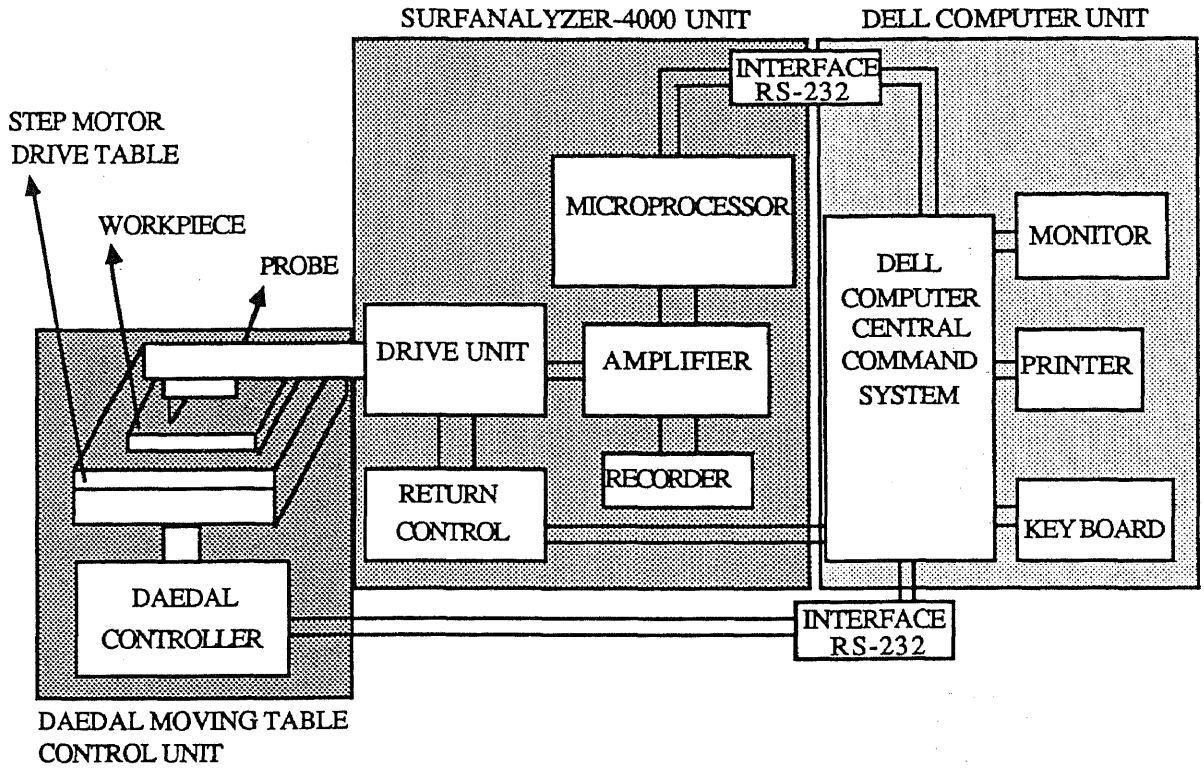

Figure 2-5 The measuring system for 3-D surface topography

Table 2-1 Materials and operation conditions of the six AWJ workpieces

Workpiece	Material	Pressure (MPa)	Orifice (mm)	Nozzle (mm)	Cut Speed (mm/min)	StandOff (mm)	Depth (mm)	Abrasive (Garnet)
WJ1	Steel	331.2	.254	.762	7.6	1.5	63.5	#80
WJ2	Steel	331.2	.254	.762	15.2	1.5	63.5	#80
WJ3	Titanium	345	.254	.762	25.4	1.5	20.32	#120
WJ4	Titanium	345	.254	.762	101.6	1.5	20.32	#120
WJ5	Stainless steel	345	.254	.762	25.4	1.5	12.7	#80
WJ6	Stainless steel	345	.254	.762	50.8	1.5	12.7	#80

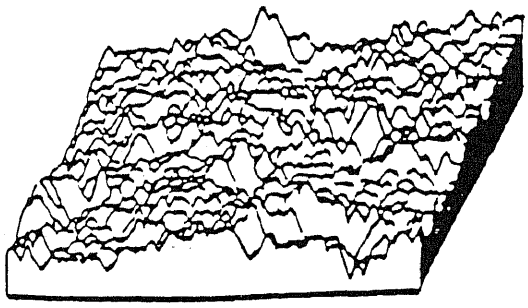

(a) WJ1 (Steel)

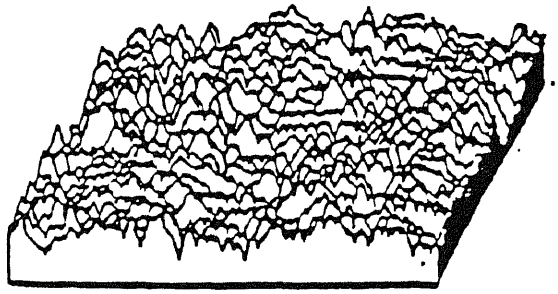

(b) WJ2 (Steel)

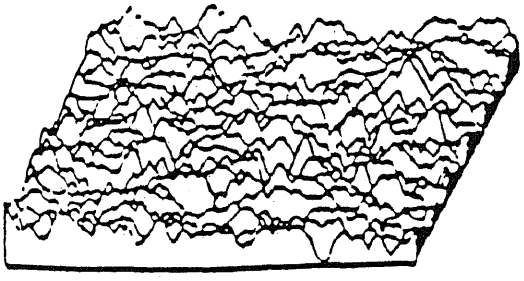

(c) WJ3 (Titanium)

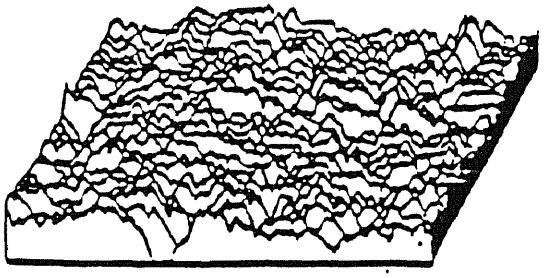

(d) WJ4 (Titanium)

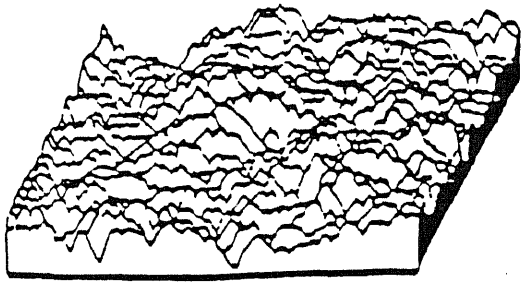

(e) WJ5 (Stainless steel)

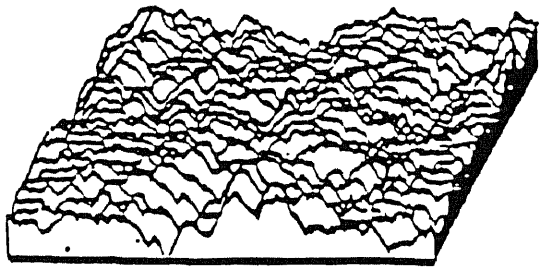

(f) WJ6 (Stainless steel)

Figure 2-6 Topographies of six waterjet cut workpieces measured from smooth zones

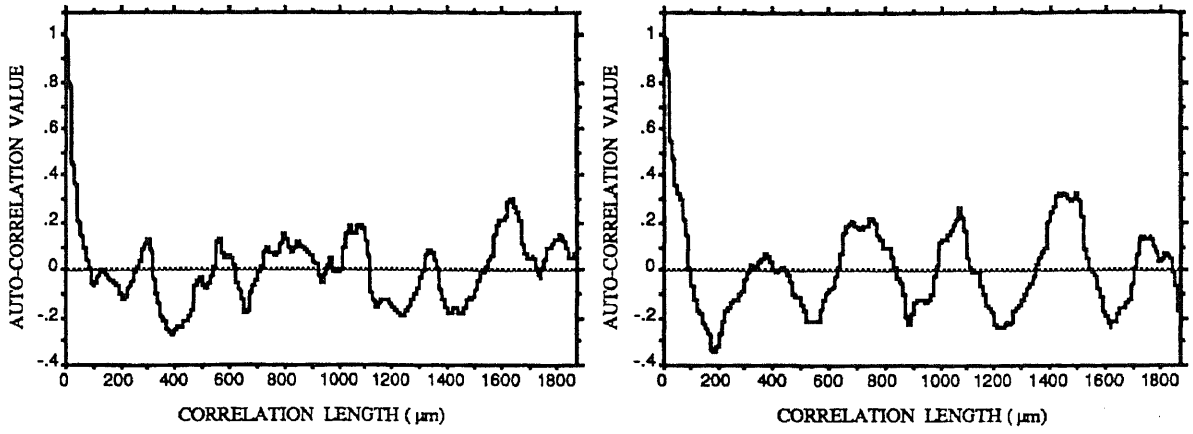

(a) WJ1, 0°

(b) WJ1, 90°

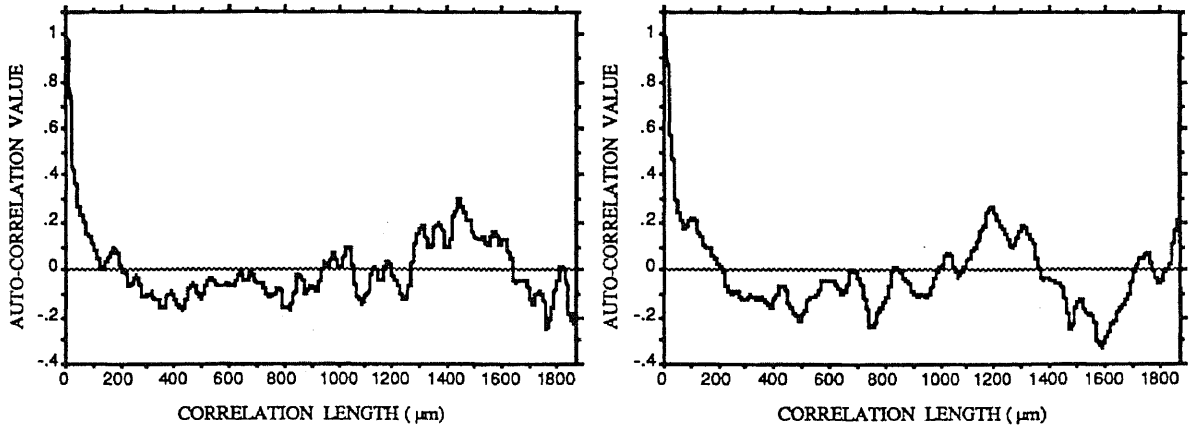

(c) WJ2, 0°

(d) WJ2, 90°

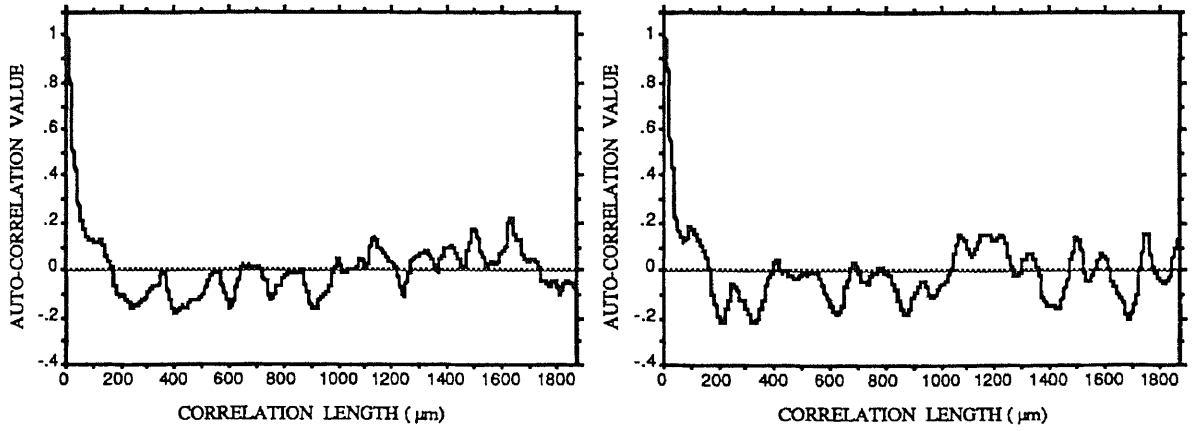

(e) WJ3, 0°

(f) WJ3, 90°

Figure 2-7 Autocorrelation functions of surface profiles of three waterjet cut workpieces

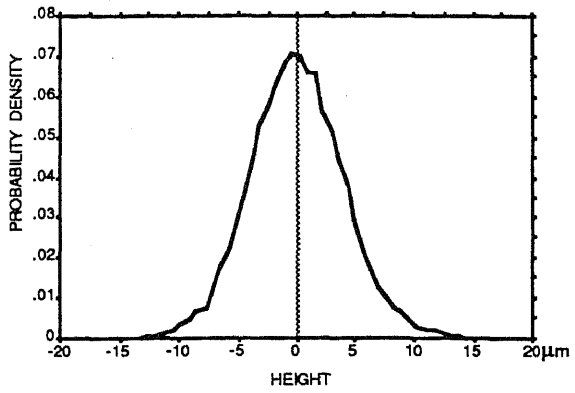

(a) WJ1, σ=3.83 µm, R_{ku}=3.173, R_{sk}=.108

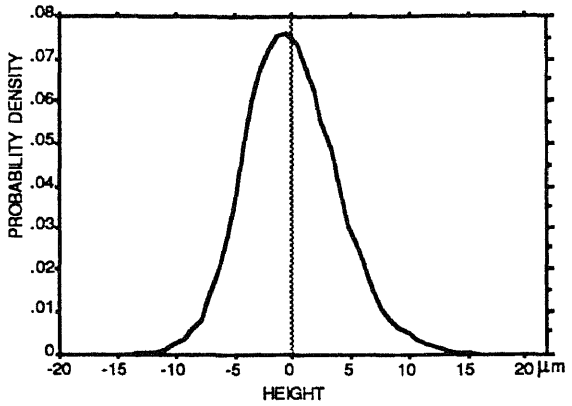

(b) WJ2, σ=3.91 µm, R_{ku}=3.31, R_{sk}=.29

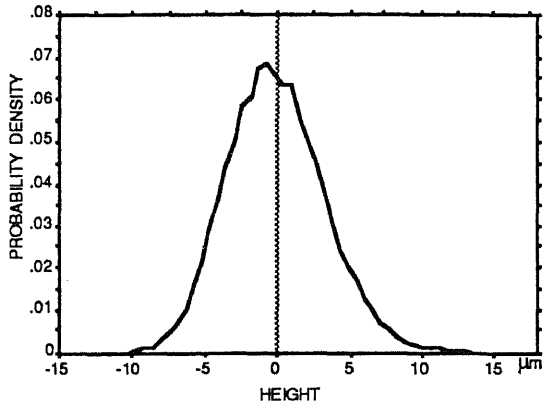

(c) WJ3, σ=3.3 µm, R_{ku}=3.289, R_{sk}=.336

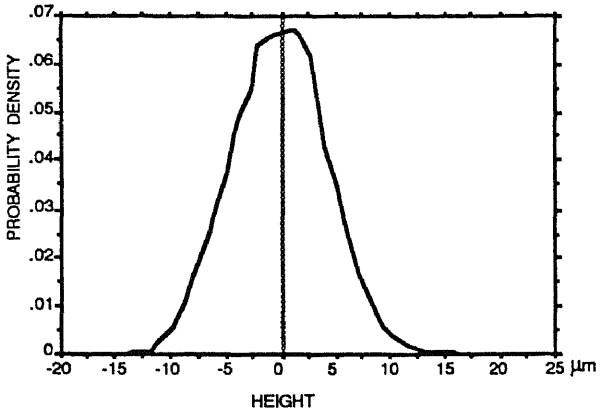

(d) WJ4, σ=4.27 µm, R_{ku}=3.12, R_{sk}=0.102

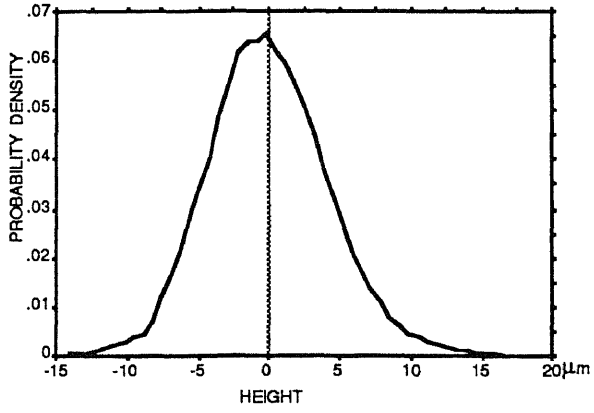

(e) WJ5, σ=4.11 µm, R_{ku}=3.34, R_{sk}=.265

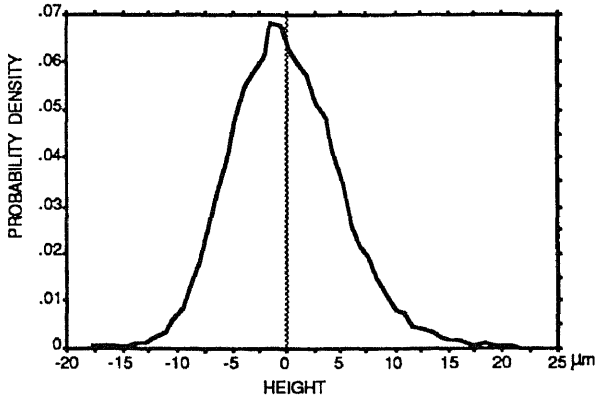

(f) WJ6, σ=5.01 µm, R_{ku}=3.53, R_{sk}=0.361

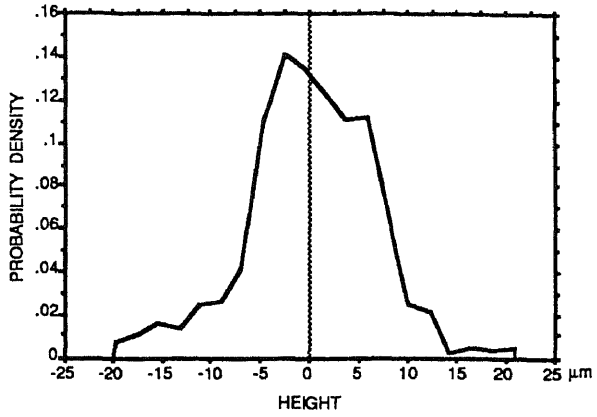

(g) A surface with small striation marks σ=6.3 µm, R_{ku}=3.8, R_{sk}=-0.26

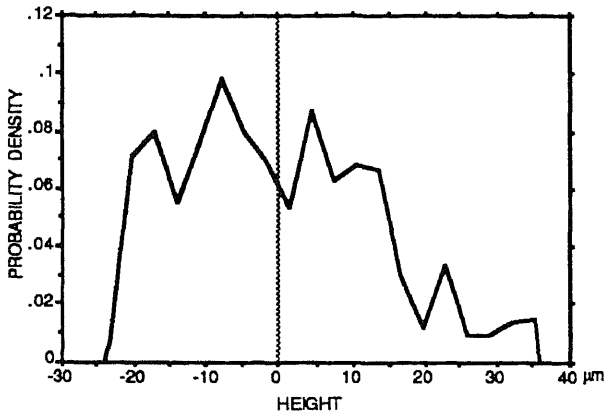

(h) A surface with heavy striation marks σ=13.1 µm, R_{ku}=2.5, R_{sk}=0.46

Figure 2-8 Amplitude distribution graphs of waterjet cut workpieces, (a)-(f) from smooth zone, (g)-(h) from striation zone

Table 2-2 γ and γ' values for AWJ, EDM (electrical discharge machined) and GRD (ground) surfaces

PARAMETER	γ	γ'
EDM 1	0.934	0.93
EDM 2	0.873	0.843
WJ 1	0.665	0.64
WJ 2	0.8566	0.653
WJ 3	0.56	0.55
WJ 4	0.446	0.5
WJ 5	0.722	0.72
WJ 6	0.79	0.74
GRD 1	0.168	0.24
GRD 2	0.24	0.247
GRD 3	0.21	0.21

meet these requirements, thus these surfaces are of the Gaussian type. As a comparison, Figure 2-8 (g) and (h) are two distribution graphs for surface profiles from the transition zone and striation zone depicted in Figure 2-4. Obviously these are not of Gaussian distribution.

The isotropic property of the generated surface in the smooth zone was also evaluated. Based on equations (2.6) and (2.7), γ and γ' values of the six AWJ workpieces were calculated. They are listed in Table 2-2. For comparison, γ and γ' values for two surfaces generated by electrical discharge machining (EDM) and three surfaces generated by grinding were also calculated. They are also listed in Table 2-2. It is clear that EDM surfaces are strongly isotropic and grinding surfaces are strongly anisotropic (Sayles and Thomas, 1979). The γ and γ' values of AWJ surfaces are between those of EDM surfaces and those of grinding surfaces, and they are closer to those of EDM's. This suggests that the texture of AWJ surfaces is moderately isotropic.

The values of several surface parameters were calculated for the smooth regions of the six AWJ generated surfaces and they were compared with those of the surfaces generated by milling and turning; see Table 2-3. The comparison shows that the values of R_a and R_q of AWJ generated surfaces are comparable to those generated by conventional milling and turning techniques. However, the values of R_{sk} and R_{ku} are quite different. This is because AWJ surfaces are of random, Gaussian type, but the other two types of surfaces are deterministic and periodic. Gaussian and isotropic surfaces are preferred in many engineering applications due to their uniform

property. Thus there is a good potential for the use of AWJ machining as a replacement for turning, milling, and other conventional shaping processes.

Table 2-3 Parameter values of surfaces generated by waterjet, turning, and milling processes (the values for turning and milling were each averaged from five workpieces).

Workpiece	R_a μm	R_q μm	R_{sk}	R_{ku}
WJ1	3.035	3.83	0.108	3.17
WJ2	3.09	3.90	0.29	3.3
WJ3	2.63	3.3	0.337	3.289
WJ4	3.42	4.27	0.102	3.127
WJ5	3.25	4.11	0.265	3.34
WJ6	3.94	5.01	0.362	3.53
TURNING	3.48	4.36	0.556	2.31
MILLING	3.49	4.12	0.498	2.20

2.4.2 Power Spectrum Analysis for Striation Zone

We have also used power spectrum analysis to study the surface texture in the striation zone. We examine the frequency and amplitude characteristics of the power spectrum and their relations with cutting speed and depth of cut. The results of this study are presented below.

2.4.2.1 Frequency Characteristics

The influence of depth of cut on the frequency content of power spectrum of an AWJ surface is shown in Figure 2-9. Eight profiles were sampled at the depths from 2 mm (top surface) to 16 mm

(bottom surface) in the cross striation direction on an AWJ surface. The dominant frequencies are the same (1 HZ) for all of the eight profiles. This means that the depth of cut has no effect on the dominant frequency of power spectrum of the striation surface.

The influence of cutting speed on the dominant frequency of power spectrum was also examined. Four workpieces were cut in different speeds of 6, 8, 10, and 12 in./min., respectively. Their striation (spatial) wavelengths can be determined easily by counting the number of striation marks in a unit length. If the striation wavelength and cutting speed for each surface are considered, the dominant frequency of power spectrum can be found for all the surfaces. For these four workpieces their dominant frequency of striation are the same. This means that like the depth of cut, the cutting speed is found to have no apparent effect on the dominant frequency of power spectrum.

2.4.2.2 Amplitude Characteristics

Figure 2-10 (a) and (b) show the amplitude of the dominant frequency of surface profile power spectrum for several surfaces generated at different depths of cut and different cutting speeds. It can be seen that the larger the depth of cut or cutting speed, the larger this amplitude.

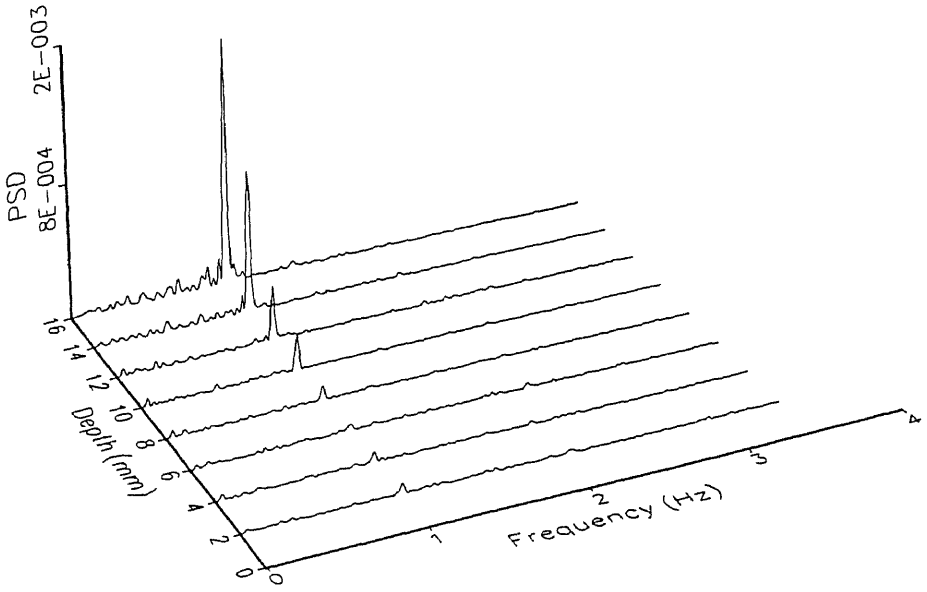

Figure 2-9 Power spectra of profiles obtaines from the striation zone of a surface at different depths from the top

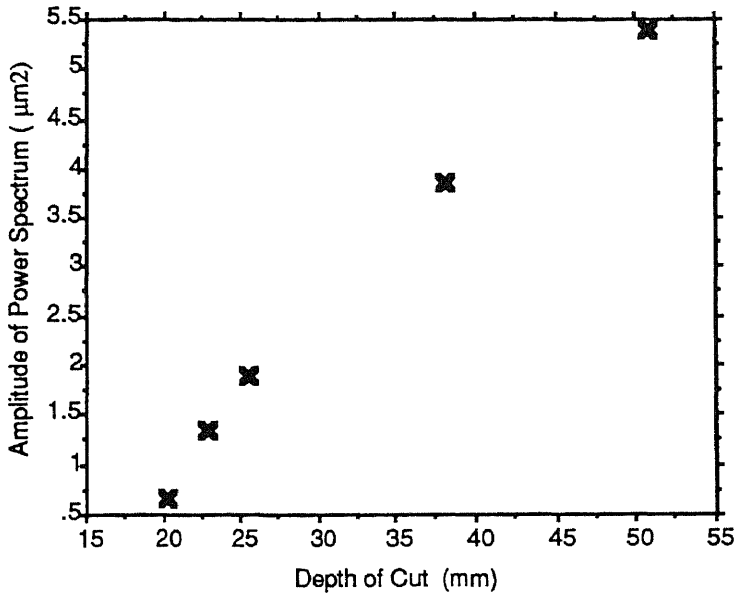

(a)

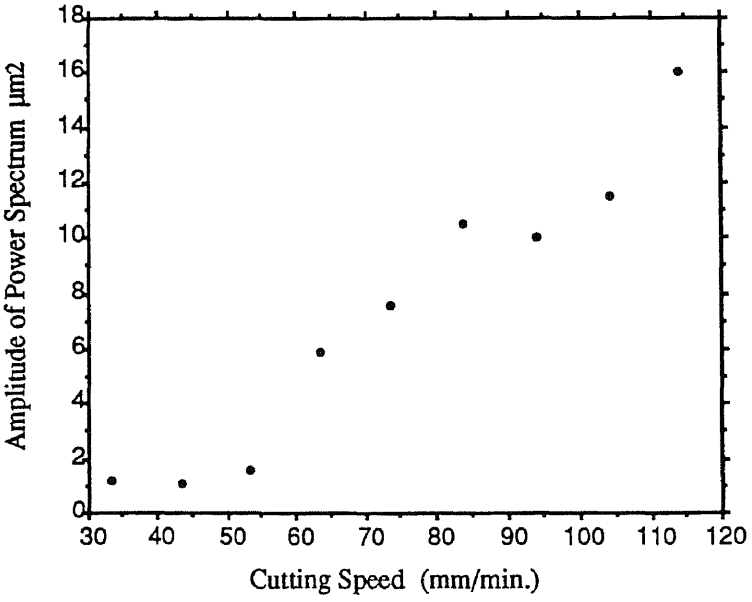

(b)

Figure 2-10 Amplitude of dominant frequency of profile power spectrum as a function of (a) depth of cut (b) cutting speed

2.5 Relations of Surface Roughness with Cutting Conditions

2.5.1 Effects of Cutting Parameters

In this subsection we shall study the effects of cutting parameters on the whole waterjet cutting surface including both smooth and striation zones. The effects of operational parameters including depth of cut, cutting speed, orifice diameter, and abrasive size on the generated surface were investigated for 35 steel specimens. Table 2-4 lists the values of parameters that are used in the study.

Eleven of the specimens were machined at various depth of cut (Table 2-4) while the rest of the cutting condition was fixed. Surface profiles were sampled from the top, middle and bottom portions of each specimen. Figure 2-11 shows the functional relations of surface roughness parameters R_a and R_q with depth of cut. Generally speaking, the roughness of the top portion of the surface is independent of the depth of cut (see R_{a1} and R_{q1} data). For the bottom portion of the surface, depth of cut clearly affects surface roughness (see R_{a3} and R_{q3} data). There exists a critical depth of cut, beyond which the relationship is: the larger the depth of cut the rougher the generated surface, and below which the depth of cut has almost no effect on the surface roughness. Essentially, below a certain depth of cut the entire machined surface is smooth with negligible striation effect. Above this depth of cut, however, striation becomes significant and the surface can be divided into a smooth zone and a striation zone. Under the condition stated in Figure 2-11, the critical depth of cut is about 18 mm. Machining at a depth of cut

lower than this would generate surfaces which are entirely smooth.

For studying the effect of cutting speed on surface roughness, twelve of the steel specimens were machined at different cutting speeds (Table 2-4) with the values of other cutting parameters fixed. Again, three profiles were sampled from the top, middle, and bottom potions of each specimen. Figure 2-12 shows the relations between surface roughness and cutting speed. They have very similar shapes to those between surface roughness and depth of cut in Figure 2-11. The roughness of the top portion (which is smooth) is not strongly affected by cutting speed, but the roughness of the bottom portion (with striation) is strongly affected by cutting speed. There is also a critical cutting speed, below which the entire surface is smooth and above which the surface consists of a smooth zone and a striation zone. For the condition stated in Figure 2-12, this critical speed is about 45 mm/min.

The result of surface evaluation for varying orifice diameter is depicted in Figure 2-13. The values of R_a and R_q for the upper portion of the surface are approximately constant, while the roughness of the bottom portion increases dramatically as the orifice diameter becomes less than 0.125 mm, the critical value of orifice diameter in this experiment. Again, this result demonstrates that the roughness of the upper part of the surface is invariant with respect to the operating condition.

In testing the effect of abrasive particle size, the above three sets of experiments were used to help select the values of the operation parameters so that the surfaces generated are entirely smooth. The selected condition was: cutting speed = 25.4 mm/min,

cutting thickness = 12.7 mm, and orifice diameter = 0.2286 mm. No significant striations were observed in any of these surfaces. Figure 2-14 shows that both R_a and R_q increase monotonically with increase in particle size. This relation can be explained from the mechanism of surface formation by impinging abrasive particles. Our previous study (Geskin et al., 1989) showed that the material removal by AWJ is due to the superposition of dimples generated by individual particles. Thus the roughness of the generated surface is a function of particle size. The test result indicates that the roughness parameters R_a and R_q of the generated surface are proportional to abrasive particle size.

Table 2-4 Values of cutting process parameters used in the experiments

Cutting Speed Test		Depth of Cut Test		Orifice Diameter Test		Abrasive Size Test	
Specimen	Speed (mm/min)	Specimen	Depth (mm)	Specimen	Diameter (mm)	Specimen	Size (μm)
CS1	12.7	CT1	5.08	OD1	0.1016	AS1	120
CS2	22.9	CT2	7.65	OD2	0.1270	AS2	175
CS3	33.0	CT3	10.16	OD3	0.1524	AS3	277
CS4	43.2	CT4	12.70	OD4	0.1778	AS4	384
CS5	53.3	CT5	15.24	OD5	0.2032		
CS6	63.5	CT6	17.78	OD6	0.2286		
CS7	73.7	CT7	20.32	OD7	0.3048		
CS8	83.8	CT8	22.86	OD8	0.3556		
CS9	94.0	CT9	25.40				
CS10	104.1	CT10	38.10				
CS11	114.3	CT11	50.80				
CS12	127.0						

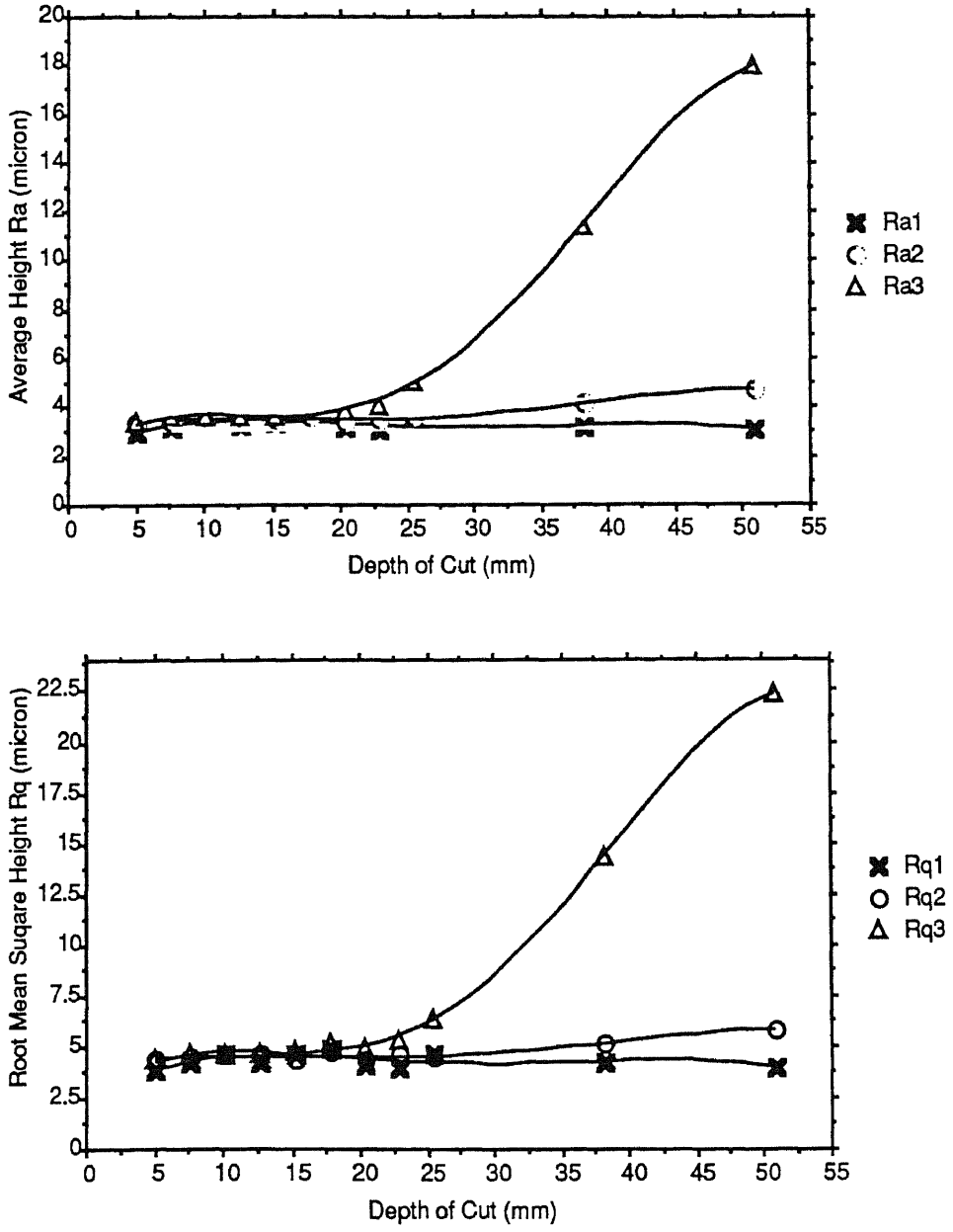

Figure 2-11 Surface roughness in relation to depth of cut. R_{a1} and R_{q1} are for the top surface, R_{a2} and R_{q2} for the middle surface, and R_{a3} and R_{q3} for the bottom surface. The cutting condition is: water pressure = 317.4 MPa, cutting speed = 20.3 mm/min., sapphire nozzle diameter = 0.2286 mm, carbide tube diameter = 0.8322 mm, abrasive size = 80# Garnet, abrasive flow rate = 199.5 g/min, and stand-off distance = 1.5 mm.

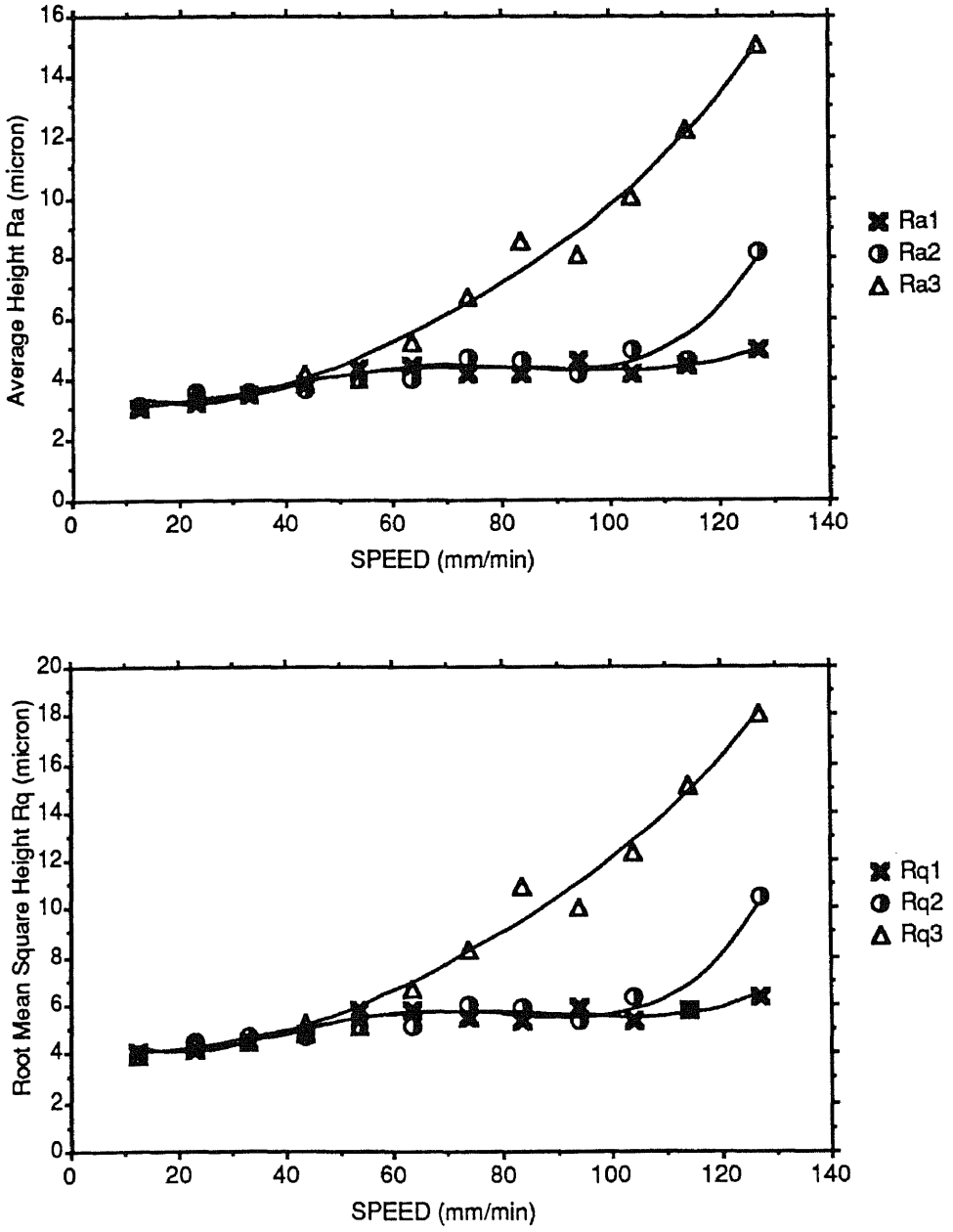

Figure 2-12 Surface roughness in relation to cutting speed. The cutting condition is: water pressure = 317.4 MPa, cutting thickness = 12.7 mm, sapphire nozzle diameter = 0.2286 mm, carbide tube diameter = 0.8322 mm, abrasive size = 80# Garnet, abrasive flow rate = 199.5 g/min, and stand-off distance=1.5 mm

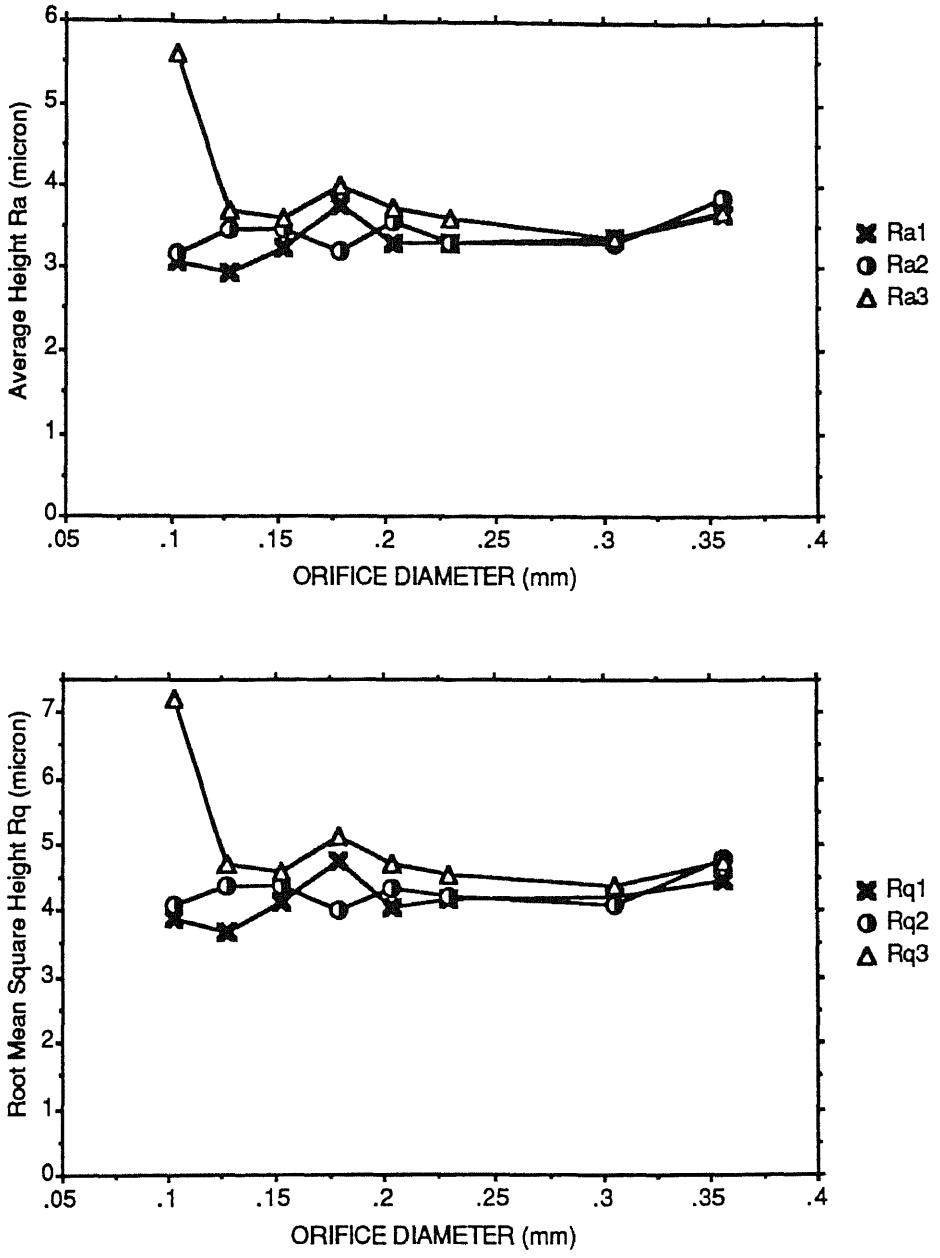

Figure 2-13 Surface roughness in relation to orifice diameter. The cutting condition is: water pressure = 331.2MPa, cutting thickness = 12.7 mm, cutting speed = 25.4 mm/min., carbide tube diameter = 0.8322 mm, abrasive size = 80# Garnet, abrasive flow rate = 214 g/min and stand-off distance = 1.5 mm

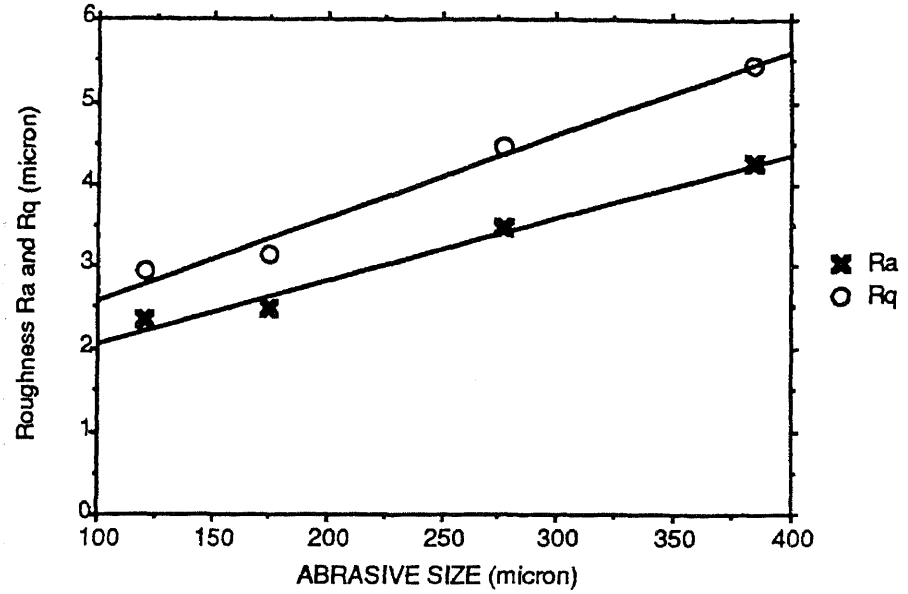

Figure 2-14 Surface roughness in relation to abrasive size

2.5.2 Discussion

We have found from the experiments that the roughness of the upper part of the examined surface is invariant with respect to the operation condition. The formulation of a mathematical model predicting the characteristics of this smooth region is part of our on-going study. Here we simply provide an explanation for this observation.

The surface generated by AWJ contains a region where the direction of the jet does not change in the course of the jet penetrating into the workpiece. The jet penetration depth is determined by the balance of the available energy of the jet and the required energy of material destruction. The available jet energy is determined by the condition of jet formation, such as water pressure and orifice diameter, and the condition of jet-workpiece interaction,

such as cutting speed and depth of cut.

The jet penetrates into the workpiece only if the available energy of the jet is dissipated and eventually approaches the material destruction energy required. This determines the depth of jet penetration. The conditions of surface generation in the regions of excessive jet energy are identical at different portions of the surface, thus the generated surfaces are homogeneous.

Our study shows that the smooth portions of the generated surfaces are fairly isotropic. The surface generated by AWJ is formed by the superposition of micro dimples created by individual abrasive particles. The large number of dimples and grooves determines the isotropy property of the generated surface. The roughness of this surface depends on the size of grooves.

The operation parameters (orifice diameter, cutting speed, and depth of cut, etc.) which determine the available energy of the jet do not affect the surface topography if the jet has sufficient energy such that the entire penetrated surface is homogeneous and isotropic. The conditions under which the available jet energy and the required material destruction energy become comparable determine the critical values of the operation parameters.

2.6 Effects of Structure Dynamics on Striation Formation

2.6.1 Experimental Observations

The mechanism of striation formation is a main topic in characterization and modeling of waterjet machined surfaces.

According to Hashish's (1984, 1991) observation the striation occurs only at the lower part of the surface which is mainly due to the erosion mode changes along the penetrated direction and the whole cutting process is cyclic in natural. This conclusion is based on some video pictures recorded by a high speed movie camera in the direction perpendicular to the traverse direction. What can be seen from the pictures are only the projections of the cutting processes to a plane (i.e. a two dimensional visualization). However from our experiments it is noticed that the jet is off the cutting plane at the bottom of the kerf, so the cutting process is not in a two-dimensional plane but in a three-dimensional space. The striation marks appear at the upper portion of the surface can also be seen in some cases. This means that a further explanation of striation formation is necessary.

The driving mechanism of the waterjet machining system made by Ingersoll-Rand is shown in Figure 2-15. A five axes gantry robot is the main feature of this machining system. The cutting head is mounted on the gantry. The translation along the X-axis is provided by motor X and a pinion-rack system. The translations of Y and Z axes are provided by motors Y and Z, and two motorized ball-screws. Two rotation axes are perpendicular to each other; one rotates around Y-axis and the other around Z-axis. The five axes motions are controlled by Allen Bradley 8200 series CNC controller. Figure 2-16 (a) and (b) are the power spectral density graphs of two surfaces cut in Y and X directions by using the AWJ machine, respectively. It is found that when the cutting is in the Y direction a single peak spectrum is observed, whereas when cutting is in the X direction a

multi-peak spectrum is observed. Comparing the amplitudes of the two spectra, the surface cut in the Y direction shows much larger amplitude than the sample cut in the X direction (approximately 20 times). Comparing the textures of the two surfaces, it was find that although they were machined in the same cutting parameters and same material, they have quite different striation patterns. When the cutting is done in the Y-axis, the surface shows more regular and periodic striation and larger amplitude than the surface cut in the X-axis. According to Hashish's (1984) erosion model or Tan's (1986) geometry/kinematics model, there should be no difference in the striation patterns by using the same cutting parameters. From our observations, the only difference between these two cutting processes is that the AWJ machining system has different driving mechanism in X and Y directions. From these observations it is suggested that the two different striation patterns are possibly caused by the driving mechanism. To find out what is the effect of structure dynamics on the striation formation we did the following testings.

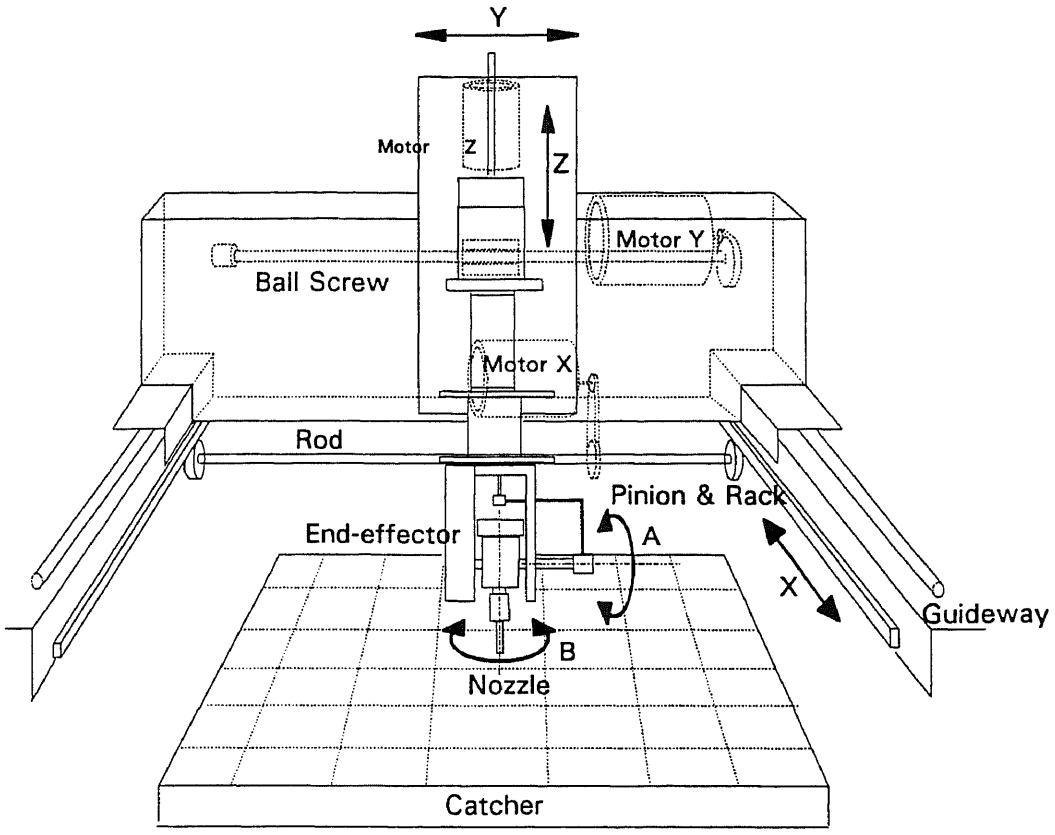

Figure 2-15 Schematic of the 5-axis gantry robot

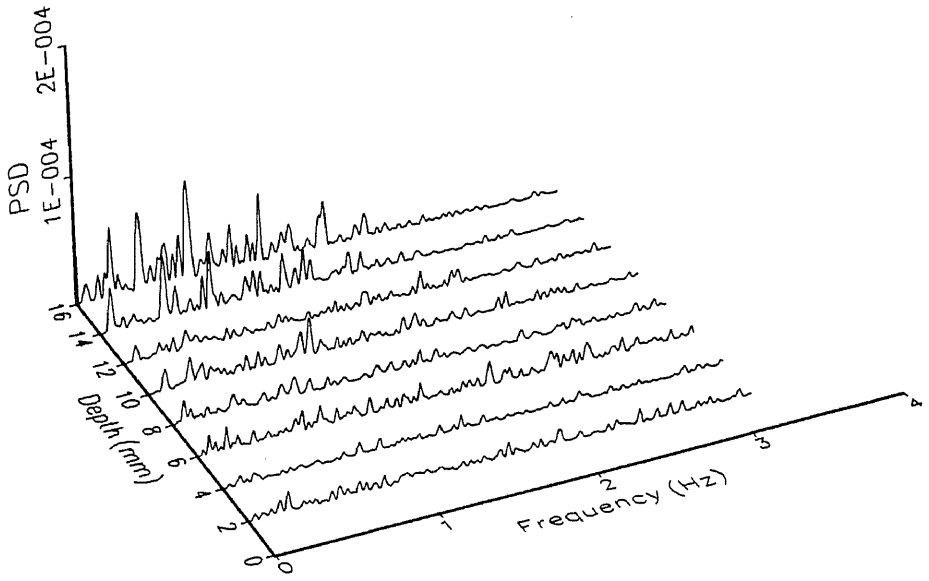

(a)

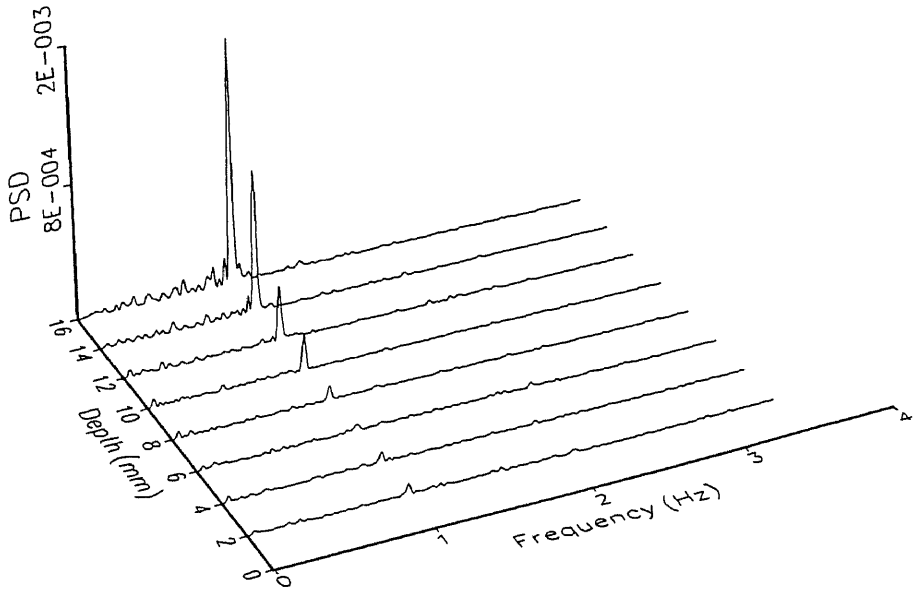

(b)

Figure 2-16 Power spectral densities measured in different depths of two samples with cutting speed 80 mm/min. in (a) Y and (b) X directions on the 5-axis machine

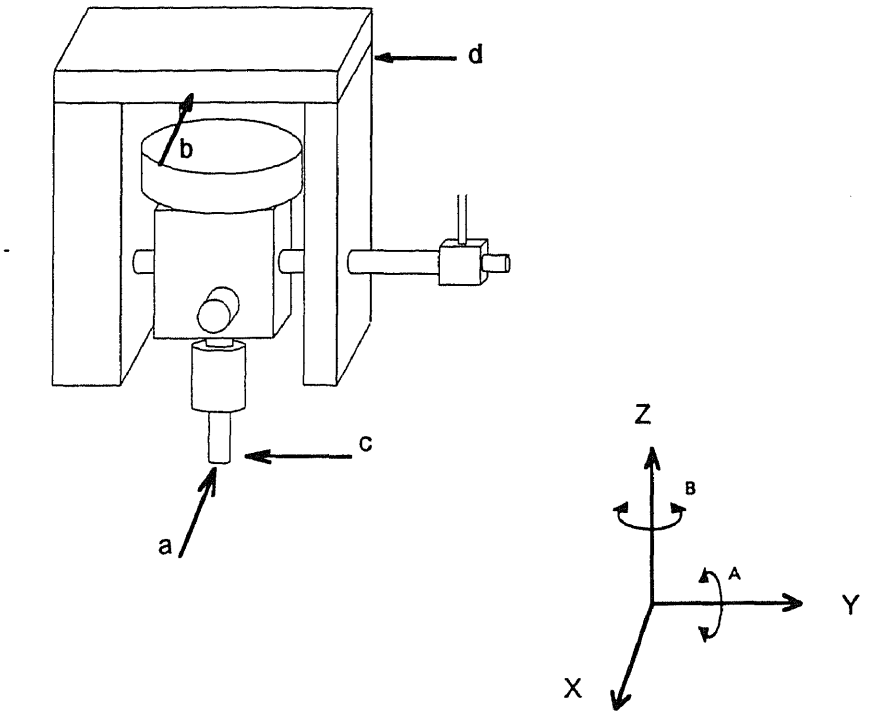

Figure 2-17 The schematic of the end-effector

2.6.2 Vibration Testing

Experiments were done by just turning the drive of the robotic system and the jet on without moving the robot arms, and by measuring the vibrations at the four positions of the end-effector as shown in Figure 2-17. The vibrations and their power spectral densities of the four positions are shown in Figure 2-18. It was found from the figure that the same vibration frequency in the X direction can be measured from positions a and b, but this vibration can not be found in the perpendicular Y direction of positions c and d. The vibrations in the X direction show much larger amplitudes than the vibrations in the Y direction. The dominant frequency of the vibration in the X direction is 1 Hz and this matches with the striation frequency, whereas the frequencies of the vibrations in the Y direction show a random behavior. Because the vibration of 1 Hz is much lower than the natural frequency of the robotic system and their PSD have nearly the same vibration magnitude at positions a and b, the vibrations at these two positions should be in-phase. Thus the bigger compliance of the nozzle head in X direction is not the reason of the formation of the periodic striation.

2.6.3 Effect of the Motor Driving System

By examining the motor-driving system of the system (see Figure 2-15), two possible vibration sources for causing regular striation in the Y direction were identified. Two motors that used to drive the translations in the X and Y directions are mounted on the frame of the gantry robot. They both rotate along the Y axis and their motions are coupled with the roll mode of the robot, so the vibration only

happens in the X direction. There is no motor rotation about the X axis and the stiffness of the structure in Y direction is relatively high, so there is no periodic vibration in the Y direction. By further analysis we found that the translation for Y axis is acted by a pair of ball-screw. This kind transmission has high position resolution, small backlash, and vibration. The translation for X axis is acted by a pair of pinion-track and it has lower position resolution, larger backlash, and vibration. We also measured vibration frequency of motor X, it was found that its rotator had a vibration frequency of one Hz. All of these suggest that when cutting in the Y or X direction the vibration of motor X or motor X is the main source of the striation formation on the waterjet generated surfaces for our AWJ cutting system.

The vibration of an AWJ machining system plays an important role in the generation of the striation marks. For our Ingersoll-Rand waterjet machine, the vibrations of motor X and motor Y are the main cause of striation formation. To decrease the vibration and improve surface quality the possible ways are the isolation of motors with the robot arms, and the design of vibration absorbers.

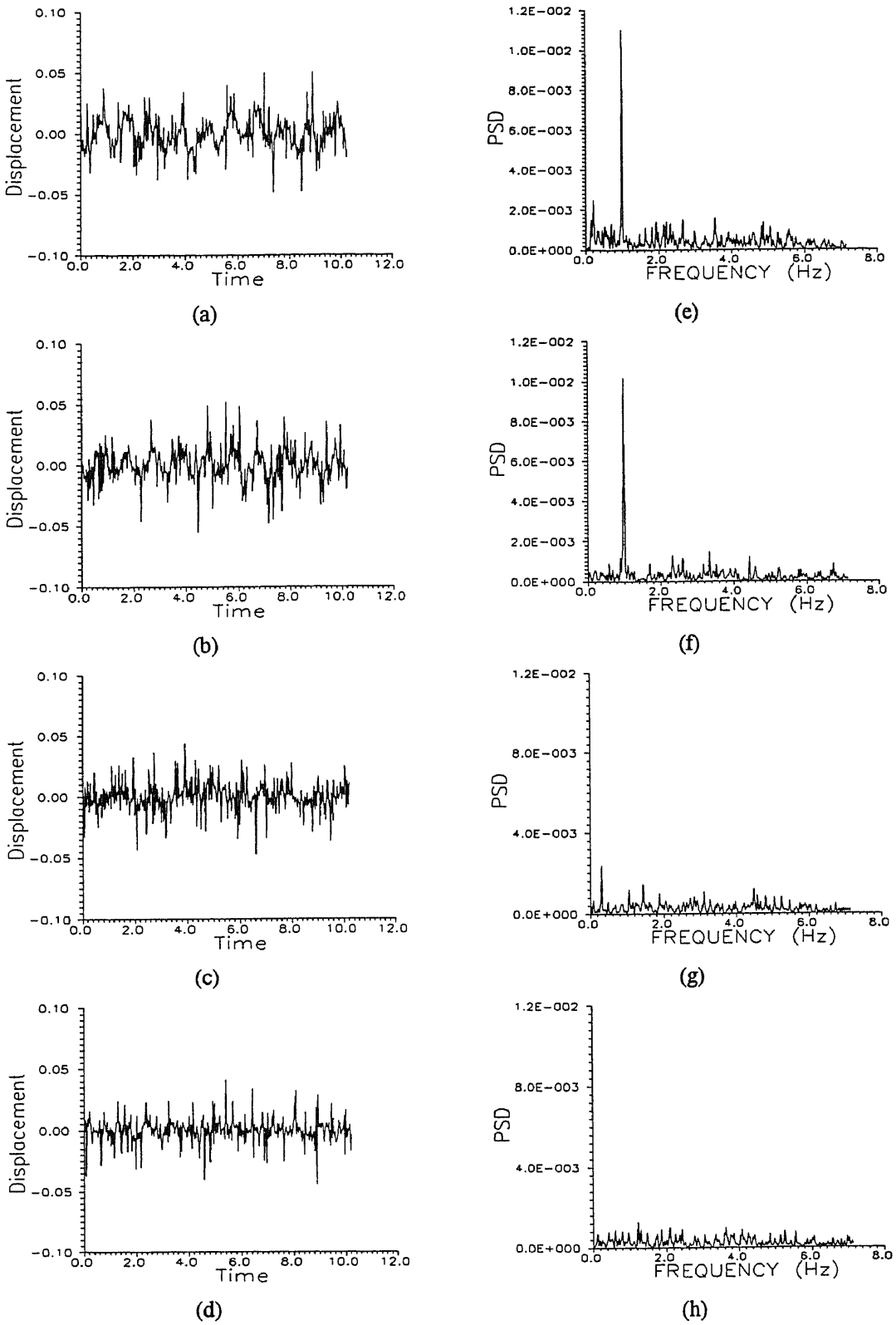

Figure 2-18 (a), (b), (c) and (d) are the displacements measured at the positions a, b, c, and d shown in the figure 2-17 ; (e), (f), (g), and (h) are the power spectral densities of (a), (b), (c), and (d).

2.7 Chapter Conclusion

AWJ surfaces can be separated into two parts: the smooth zone and the striation zone. The proportions of these two zones on a surface depend on the cutting condition described by cutting speed, depth of cut, and orifice diameter. By controlling the cutting conditions, a surface can be totally smooth with no striation zone, or can be completely dominated by striations. By the use of autocorrelation functions, surface height distributions, and isotropy identification criteria, it is concluded that the surface topography of the smooth zone is random, Gaussian, and moderately isotropic.

From the profile power spectrum analysis for the striation zone of an AWJ surface, it is found that the dominant frequency of this spectrum is independent of cutting speed and depth of cut. The amplitude of the spectrum increases monotonically as depth of cut or cutting speed increases.

The parameters R_a and R_q are strongly related to depth of cut and cutting speed for the striation zone of an AWJ surface. Their values increase rapidly as depth of cut or cutting speed increases. In the smooth zone, the dependence of these parameters on depth of cut or cutting speed is from weak to negligible. These properties can be utilized to define cutting process conditions in which a high quality smooth surface can be obtained. For example, if the cutting speed is less than 45 mm/min., the depth of cut less than 18 mm, and the orifice diameter larger than 0.125 mm, a very fine surface can be generated on a steel workpiece by AWJ machining.

The vibration of an AWJ machining system plays an important role in the generation of striation marks. In our 5-axis waterjet

machine, the vibration of the machine structure is the main cause of striations. This vibration originates from the driving motor and is not due to structure resonance.

CHAPTER 3
FUNDAMENTALS OF FRACTAL GEOMETRY

3.1 Chaos—A New Science

Over the last decade or so, physicists, biologists, astronomers and economists have created a new way of understanding the growth of complexity in nature. This new science, called chaos, offers a way of seeing order and pattern where formerly only the random, erratic, and unpredictable, in short the chaotic, had been observed. The science of chaos cuts across traditional scientific disciplines, tying together unrelated kinds of wildness and irregularity: from the turbulence of weather to the complicated rhythms of the human heart, from the design of snowflakes to the whorls of windswept desert sands. *Fractal geometry* is the most significant approach in the science of chaos. Fractals have blossomed tremendously in the past few years and helped reconnect pure mathematics research with both the natural science and computing. Within the last 5-10 years fractal geometry and its concepts have become central tools in most of natural science: physics (Mandelbrot and Ness 1968), chemistry (Avnir, Farin, and Pfeifer 1984), biology (Goldberger, Rigney and West 1990), geology (Peitgen and Saupe 1988), meteorology (Mandelbrot 1982), material science (Avnir, Farin and Pfeifer 1985), and tribology (Ling 1990; Manjumdar 1990). In this dissertation the emphasis is on tribology.

Fractal Geometry is an improvement and development of Euclidean geometry, a natural geometry of the physical world. Euclidean geometry describes ordered objects such as points, curves,

surfaces and cubes using dimensions of 0, 1, 2, 3, respectively. But the real world is never so ideal and simple. Shapes such as coastlines, mountains, landscape and clouds are not easily described by traditional Euclidean geometry. Fractal geometry provides an excellent description of many natural shapes and it is not like Euclidean shapes which have one, or at most a few, characteristic sizes or length scales (the radius of a sphere, the side of a cube), fractals, like coastlines, possess no characteristic sizes and scales. Natural shapes are complex and hard to describe, but they often possess a remarkably simplifying invariance under changes of magnification. This statistical self-similarity is the essential quality of fractals in nature. It may be quantified by a fractal dimension, a number that agrees with our intuitive notion of dimension but need not be an integer.

The concept *Fractal Geometry* was first proposed by Mandelbrot (1976). The word *'fractal'* corresponds to the verb meaning "to break;" i.e. to create irregular fragments. The original idea to use fractals came from Mandelbrot's question, "How long is the coast of Britain?" (1967). Seacoast shapes are examples of highly complicated curves such that each of their portions can, in a statistical sense, be considered as a reduced scale image of the whole. Coastlines, when measured with increased precision (finer scale), would furnish lengths ten, hundred or even thousand times as great as the length read off a school map. Figure 3-1 illustrates this property based on Richardson's investigated results (1961). The most significant features of this kind of fractal phenomena are

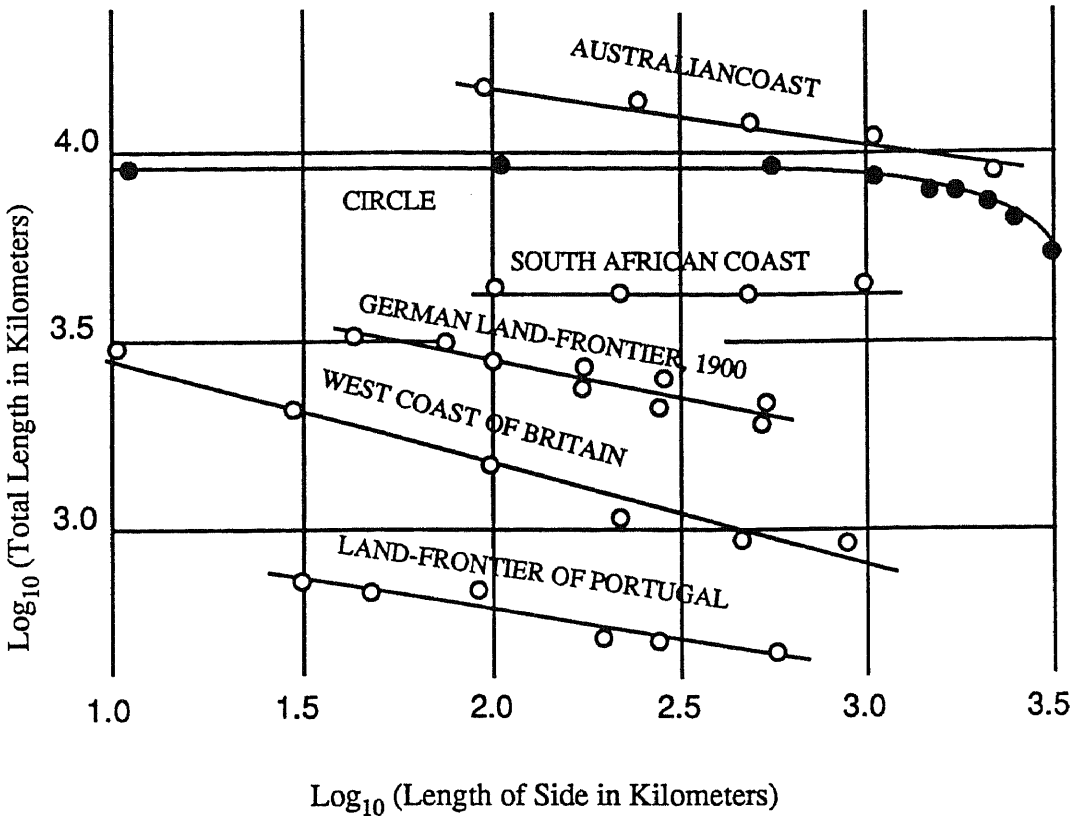

Figure 3-1 Length infinity of coastlines

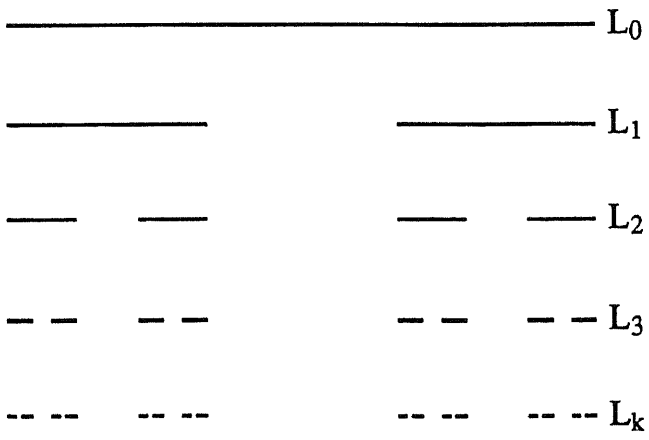

Figure 3-2 Cantor Set

length infinity and statistical self-similarity. Some examples such as boundaries of countries and shapes of mountains and clouds have the same fractal property. For a better understanding of self-similarity, its mathematical description will be introduced next.

3.1.1. Self-Similarity

The middle third Cantor set is one of the best known and most easily constructed fractals; nevertheless it displays many typical fractal characteristics. It is constructed from a unit interval by a sequence of deletion operations, see Figure 3-2. Let L_0 be a unit length. Let L_1 be the set obtained by deleting the middle third of L_0 so that L_1 consists of the two intervals and each has length 1/3. Deleting the middle third of these intervals gives L_2; thus L_2 is comprised of four intervals, each of length 1/9. We continue in this way, with L_k obtained by deleting the middle third of each interval in L_{k-1}. Thus L_k consists of 2^k intervals each of length 3^{-k} . Assume the number of intervals is N, the length of each segment is 1/M then the dimension of the Cantor set is

$$D = \frac{\log N}{\log M} = \frac{\log 2^k}{\log 3^k} = 0.631 \qquad (3.1)$$

where M is the magnification. Thus a fractional dimension comes out.

The Koch curve is another well known example; see figure 3-3. Let L_0 be a unit length. The set L_1 consists of four segments obtained by removing the middle third of L_0 and replacing it by the other two sides of the equilateral triangle based on the removed segment.

Construct L_2, L_3, ... L_k by repeating the same procedure as applied to L_1. Thus L_k comes from replacing the middle third of each straight line segment of L_{k-1} by the other two sides of the equilateral triangle. Its structure should look like this: the number of segments is $N= 4^k$, the length of each segment is $1/M = 3^{-k}$. The dimension of the Koch curve can be calculated as

$$D=\frac{\log N}{\log M}=\frac{\log 4^k}{\log 3^k} = 1.26 \qquad (3.2)$$

For a general description of fractal dimension (for self-similar fractals), we have the following definition. For an object of N parts, each scaled down by a ratio 1/M from the whole

$$NM^{-D} = 1 \qquad (3.3)$$

The fractal (self-similarity) dimension D is defined by

$$D=\frac{\log N}{\log M} \qquad (3.4)$$

This kind of purely mathematical sets is called exactly self-similarity. Most of sets in nature do not have such regular segments. They possess similarity in statistical sense. So they are refereed to as statistically self-similar.

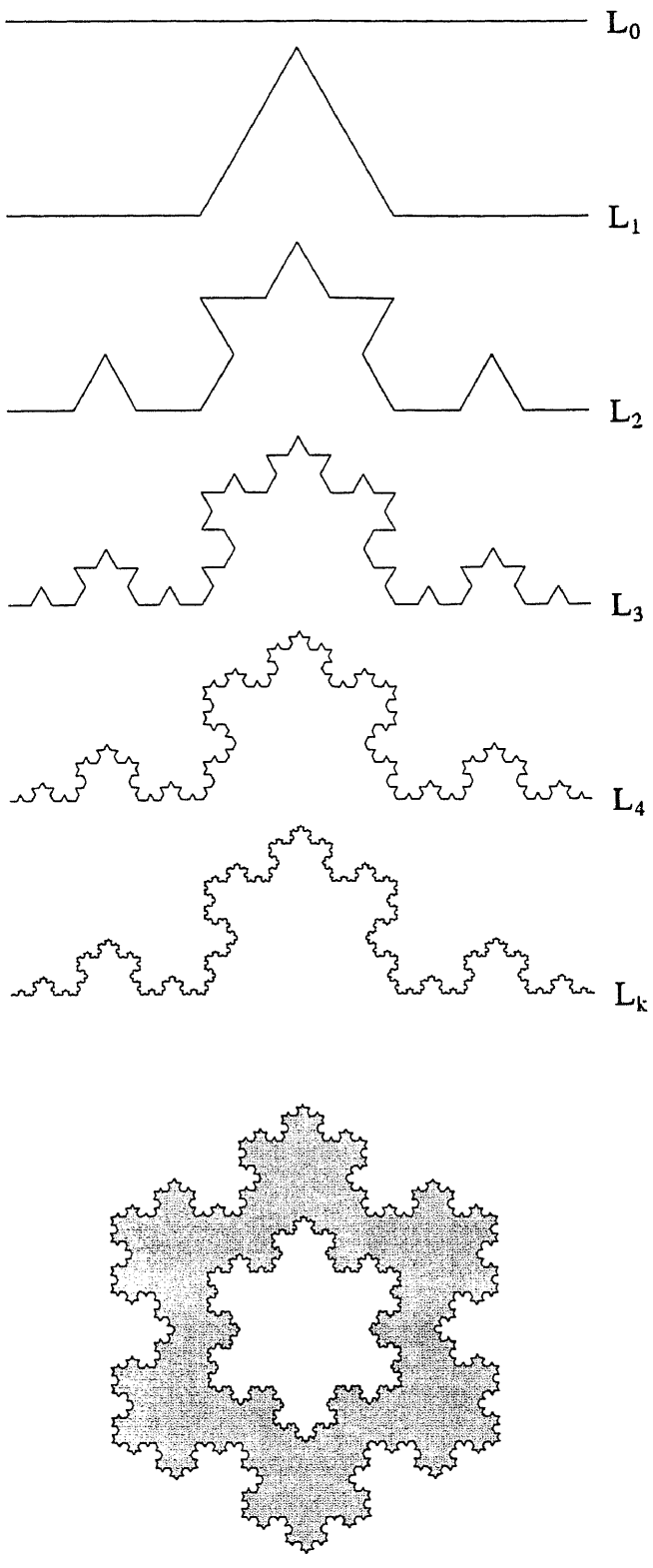

Figure 3-3 Koch curve

3.1.2 Self-Affinity

The definition of self-similarity is based on the property of equal magnification in all directions. However, there are many objects in nature which have unequal scaling in different directions. Wiener's scalar Brownian motion B(t) is a typical example of a self-affine fractal (Mandelbrot 1968). It has different measuring units in the time (t) axis and in the random walking distance (B) axis. Brownian motion has two well-known invariance properties:

1) Setting B(0)=0, the random process B(t) and $b^{-1/2}B(bt)$ are identical in distribution for every ratio b>0. One observes that the rescaling ratios of t and of B are different, hence the transformation from B(t) to $b^{-1/2}B(bt)$ is an "affinity." This is why B(t) is called "statistically self-affine." A very important role is played in fractal geometry by the more general fractional Brownian motions (fBm's) $B_D(t)$, where 0<D<1. If $B_D(0)=0$, the random processes $B_D(t)$ and $b^{-(2-D)}B_D(bt)$ are identical in distribution. The value D=3/2 sets Brownian motion B(t) as a special case of $B_D(t)$.

2) The fBm's possesses the following invariance:

$$<[B(t+\tau) - B(t)]^2> = C|\tau|^{4-2D} \qquad (3.5)$$

where < > represents the statistical average, C is a constant and D is the fractal dimension. This is the most important property and later on it will be used for fractal dimension and topothesy calculations.

Compass dimension

$D = \log(N) / \log(1 / r)$

For a ruler of size r

$N = 1 / r^{D}$

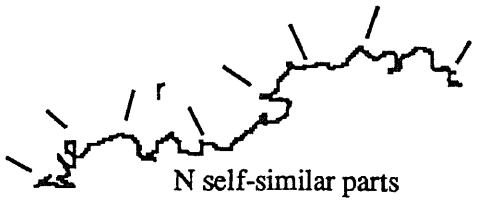

Length of coastlines

Length = r $N = 1 / r^{D-1}$

Box dimension

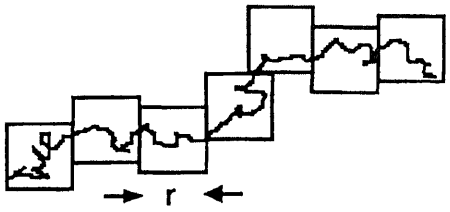

N (r)

Number of boxes (spheres) of size r needed to cover the object

$N(r) \sim 1/r^{D}$

Grid dimension

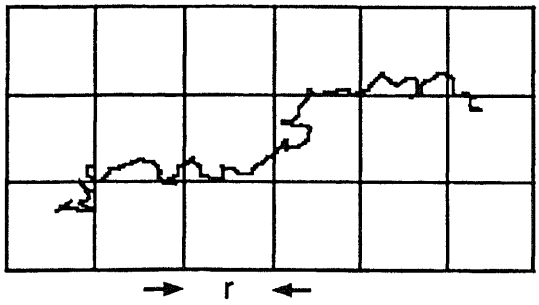

N (r) = number of squares containing a piece of object

Figure 3-4 Some image methods for obtaining fractal dimensions

3.2. Techniques for Obtaining Fractal Dimensions

There are many definitions of dimensions for fractal sets, such as Hausdorff dimension, compass dimension, box dimension, mass dimension, and area-perimeter dimension (Mandelbrot, 1982; Peitgen and Saupe, 1988), and there are several methods for computing each of these dimensions. These dimensions can be most readily calculated from images or graphs for self-similar fractals (see Figure 3-4). However, for self-affine fractals which are not self-similar, the dimension cannot be obtained so readily (Mandelbrot, 1985). In this study, we are mainly concerned with the microtopography of surfaces. The observed magnifications in vertical and horizontal directions usually differ by a factor of 100 to 10,000. The obtained graphs indicate that the surface profiles tend to be only self-affine, not self-similar. Thus other techniques must be used to compute fractal dimensions. If a homogeneous and isotropic rough surface has a fractal dimension D_s and its profile in an arbitrary direction has a dimension D_p, then a simple relation exists between them; namely, $D_s = 1 + D_p$ (Mandelbrot, 1984). In this study all dimensions are calculated from profile measurements. For convenience the subscript p of D_p has been omitted.

3.2.1 Power Spectrum Law of Fractals

Functions with fractal graphs can be obtained by specifying a certain form for their power spectra. Profiles of machined surfaces often lead to power spectra having fractal characteristics (Berry and Lewis, 1980; Mandelbrot, Passoja, and Paullay, 1984; Majumdar and Bhushan, 1990). In particular, the power spectrum has the following

general form:

$$S(\omega) = \frac{q}{\omega^{5-2D}} \tag{3.6}$$

where ω is spatial frequency, q is a constant and D is the fractal dimension of the profile. By plotting the data of S versus ω on doubly logarithmic coordinates, it is observed that if the curve has a large portion close to a straight line then the profile is fractal in this straight line range, and its D can be obtained by $D = \frac{5 - \alpha}{2}$, where α is the slope of the straight line. Figure 3-5 gives such an example using an electrical discharge machined specimen. One problem is that when the power spectrum of a profile is plotted, there are often severe statistical fluctuations on the graph; see Figure 3-5 (a). It is very difficult to find a unique D from this type of graph. Possible sources of these fluctuations are that when a time-domain continuous signal is Fourier transformed, first the signal must be digitized and filtered, and then transformed from time domain to frequency domain. Signal digitization and filter errors, white noise and energy leakage are likely to occur in these processes. An averaged power spectrum of several profiles can be used to improve this technique for obtaining D; see Figure 3-5 (b), (c) and (d). However after the averages are performed, fluctuations still can be observed; it is still a little difficult to determine a unique D from these figures.

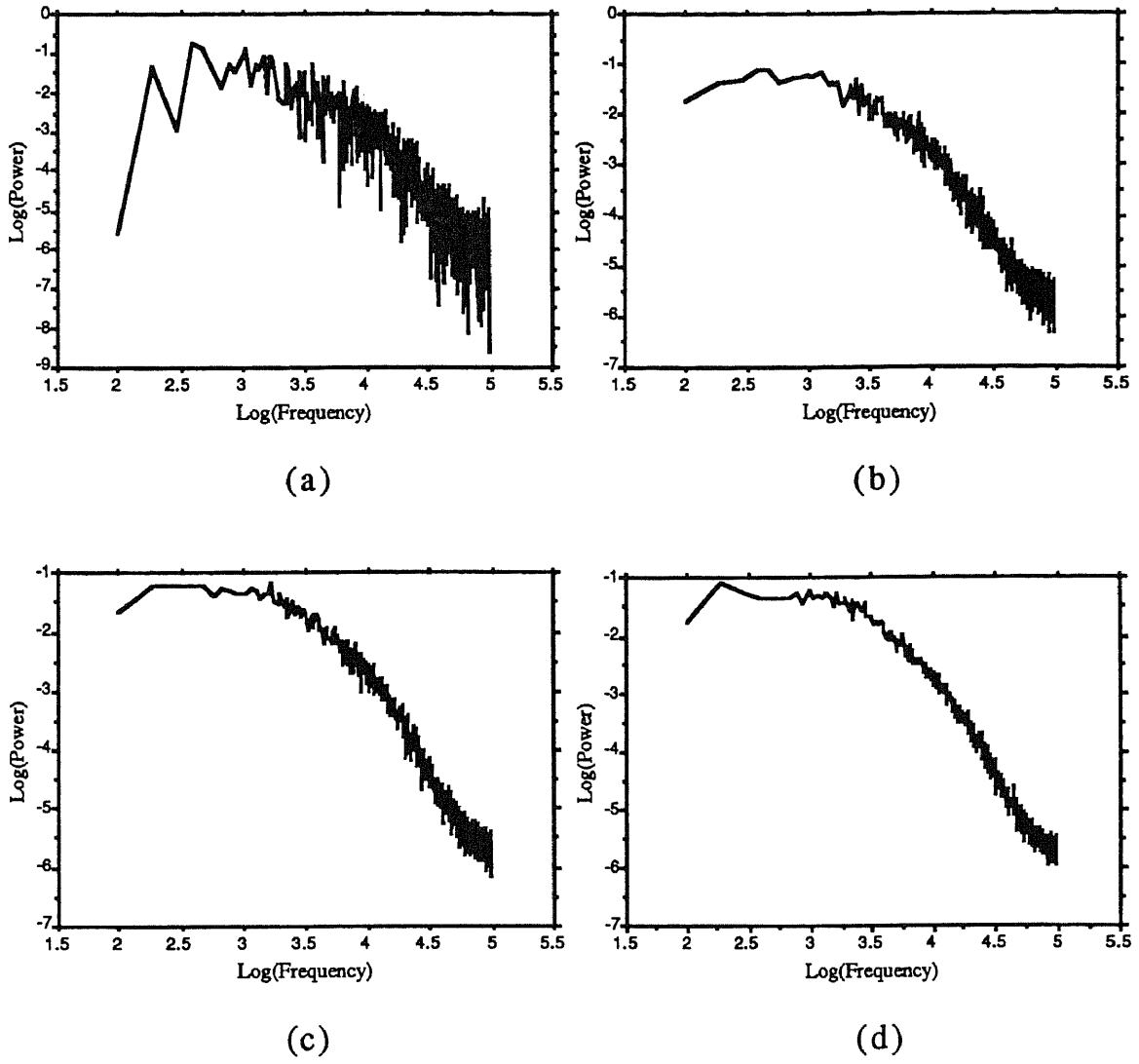

Figure 3-5 Power spectrum of an EDM surface from (a) a single profile, (b) 5 averaged profiles, (c) 10 averaged profiles, and (d) 20 averaged profiles.

3.2.2 Structure Function and Its Use in Determining Fractal Dimensions

Suppose z(x) is a fractal function; it is known (Berry,1979) that the correlation $\langle z(x_1)z(x_2)\rangle$ (and hence the variance $\langle z^2(x)\rangle$) is infinite, and z(x) is not differentiable. Berry suggested that a structure function be used to characterize z(x). The increment [z(x+λ)-z(x)] is assumed to have a Gaussian distribution with the following second moment (called the structure function)

$$\langle [z(x+\lambda) - z(x)]^2\rangle = \frac{2g}{(4-2D)} \sin[\frac{\pi}{2}(2D-3)]\Gamma(2D-3)|\lambda|^{4-2D} + m^2 \quad (3.7)$$

where m is the mean, λ is any displacement along the X direction, g is a constant, D is the fractal dimension of the z(x) function and Γ( ) is the Gamma function. It can be seen that the chords joining z-values separated by a distance λ do have a finite mean square slope. If there exists a displacement λ=L such that the chord relative to m has an r.m.s. slope of unity, then a concise formula can be written:

$$\frac{\langle [z(x+L) - z(x)]^2\rangle}{L^2 + m^2} = 1 \quad (3.8)$$

where L is a characteristic parameter of the fractal function called its topothesy. By comparing equations (3.7) and (3.8), an equation relating the structure function with fractal geometry parameters is derived:

$$\langle [z(x+\lambda) - z(x)]^2\rangle = L^{2D-2}\,|\lambda|^{4-2D} + m^2,\ 1 < D < 2 \quad (3.9)$$

Taking the natural logarithm of both sides of (3.9), we obtain

$$Y = \log(1 + m2) + 2(D - 1)\log L + 2(2 - D)\, X \qquad (3.10)$$

where $Y = \log(\langle[z(x+\lambda) - z(x)]^2\rangle)$, $X = \log|\lambda|$ and $\mu = mL^{1-D}|\lambda|^{D-2}$. If $\mu << 1$, this equation assumes the following (approximate) simpler form:

$$Y = 2(D-1)\log L + 2(2-D)X \qquad (3.11)$$

which we call the structure function equation and from which we find that D and L can be expressed as:

$$D = \frac{4-\beta}{2} \qquad 0 < \beta < 2 \qquad (3.12)$$

$$\log L = \frac{I}{2D-2} \qquad (3.13)$$

where β is the slope of equation (3.11) and I is the Y-intercept of the equation.

The structure function can be used for experimentally computing D and L of fractal surfaces. It can be used to identify whether a surface is fractal or non-fractal. Non-fractal surfaces do not possess the above mentioned properties; in other words, their doubly logarithmic plots either do not have a unique slope β, or the slope lies outside the range of (3.12). To see this we shall look at several examples of surface data which were obtained by using a stylus profilometer. Figure 3-6 (a) shows a saw tooth surface profile,

and (b) is the Log-Log plot of its structure function. Obviously it is not fractal. Figure 3-7 shows the profiles of three electric discharge machined surfaces. The structure function graphs used to calculate their fractal parameters are given in Figure 3-8. It can be seen that they have straight slopes over a large range of correlation length. These observations suggest that the structure function provides an effective method for finding D and L of self-affine fractal sets.

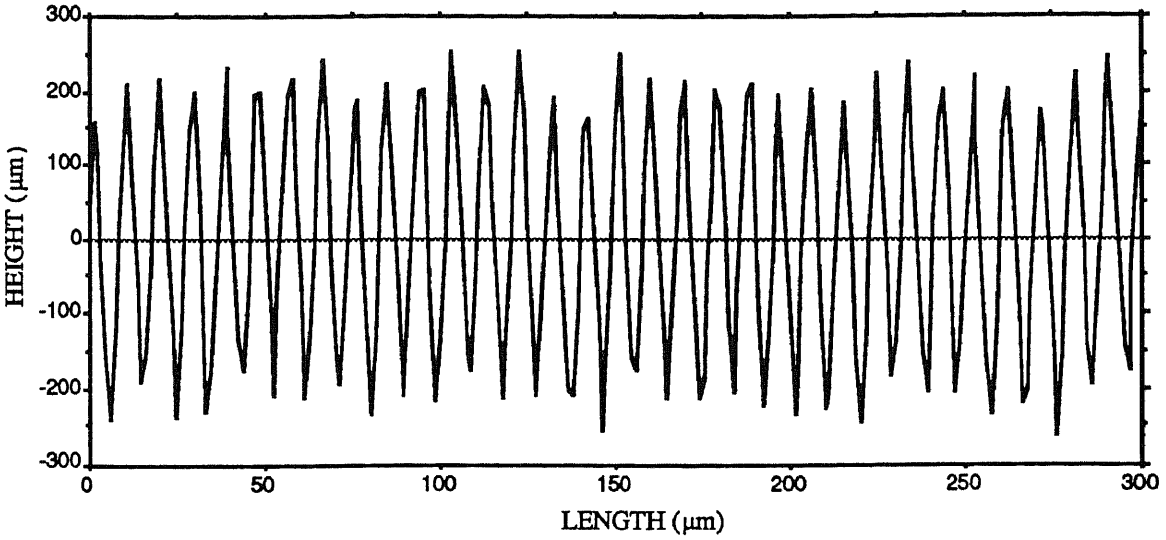

(a)

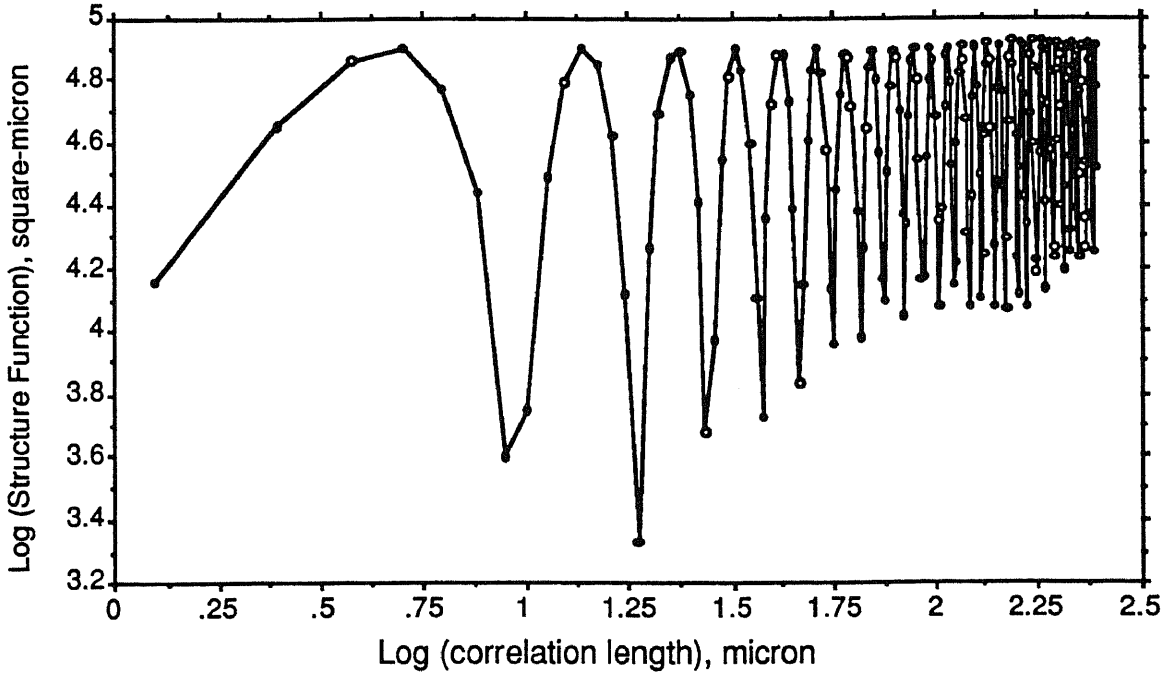

(b)

Figure 3-6 Structure function as an identifier of fractals: (a) a saw-tooth shape profile, (b) log-log plot of structure function of the saw-tooth shape profile.

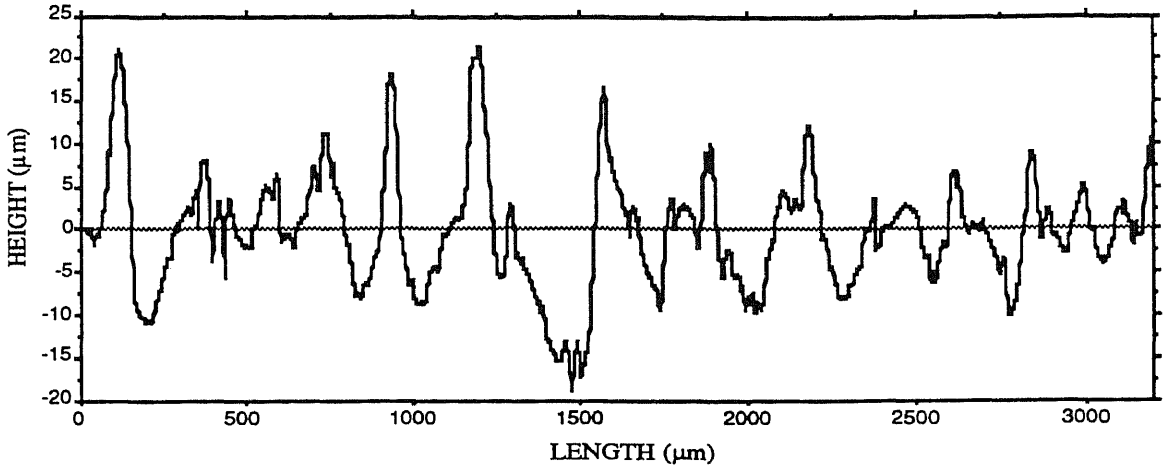

(a)

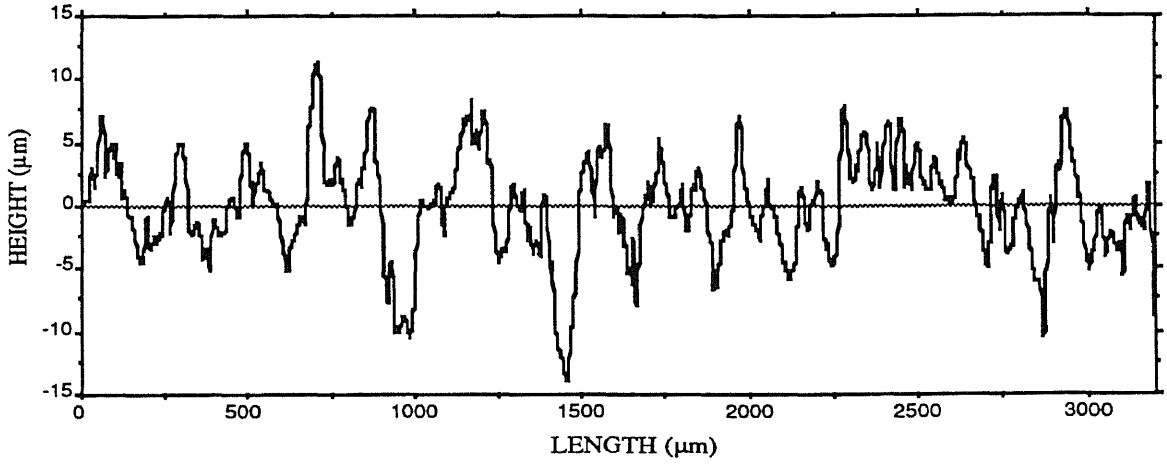

(b)

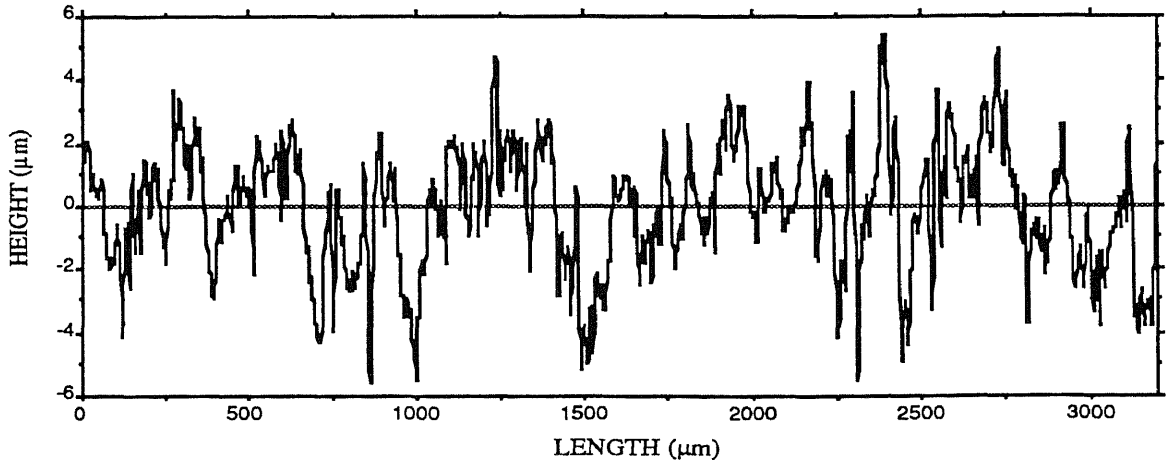

(c)

Figure 3-7 Profiles of three EDM surfaces generated with different process parameters

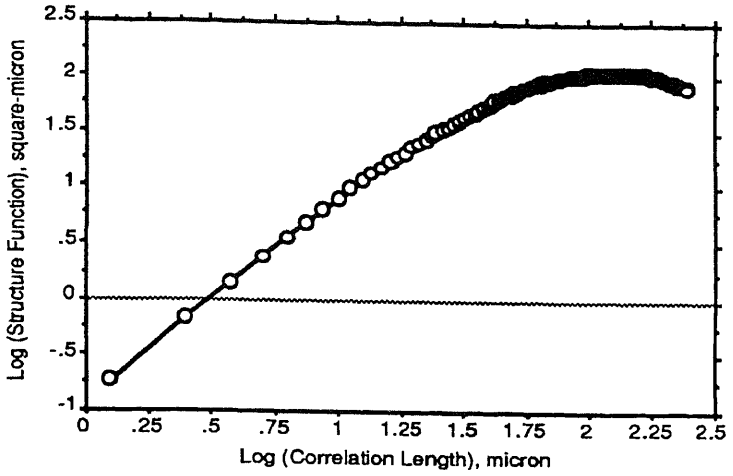

(a)

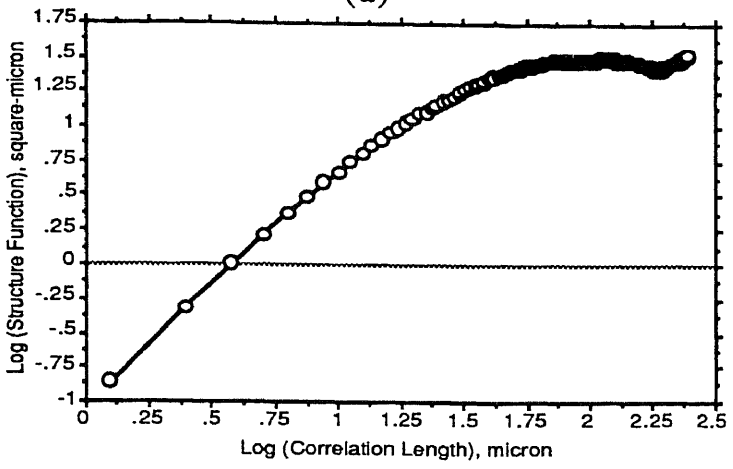

(b)

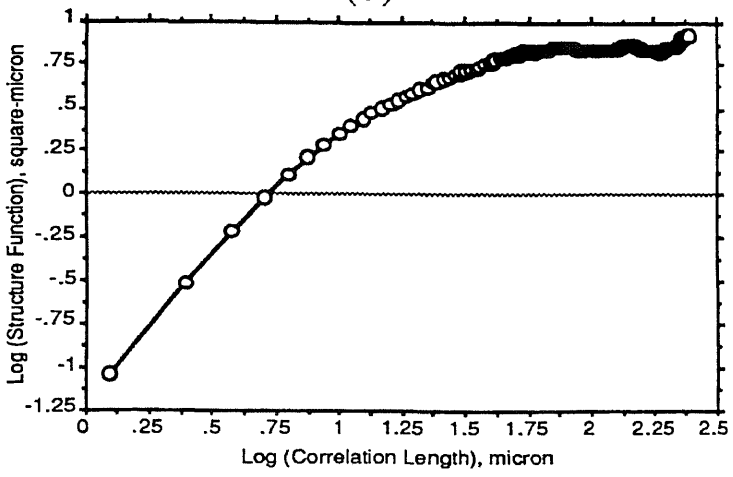

(c)

Figure 3-8 Structure function graph of (a) EDM #1 surface, D=1.252, L=0.0516 μm, (b) EDM #2 surface, D=1.385, L=0.150 μm, and (c) EDM #3 surface, D=1.546, L=0.237 μm.

3.3 Fractal Characterization of Surfaces

Characterization of surface topography has become increasingly important in many engineering fields. The methodology of analyzing surface topography has been developed for more than fifty years (Thomas, 1988; Jost, 1990). Over thirty parameters are used to quantify topography in the International Standard of Surface Roughness. This rash of parameters (McCool, 1987) causes endless disputes about the methods of measurement and evaluation of rough surfaces. Over the last dozen or so years it has been realized (Sayles and Thomas, 1978; Jordan, Hollins, and Jakeman, 1986; Majumdar and Bhushan, 1990) that much of the difficulty in using standard measures of surface roughness stems from the non-stationary and multi-scale nature of surface topography as well as the dependence of the measurements on instruments. The shortcomings of conventional statistical and random process methods have stimulated interest in new approaches to characterizing surface roughness.

Fractal geometry was initially proposed as a means of characterizing surface topography by Mandelbrot (1982, 1984). The application of fractals in surface related phenomena is very recent and shows great potential in such fields as tribology, surface contact mechanics, thermal conductance, optical scattering on rough surfaces, chemical reactivity of surfaces, currents in superconductors (Jordan, Hollins, and Jakeman, 1986; Ling, 1990; Majumdar, 1989; Avnir, Farin, and Pfeifer, 1984), etc. The use of fractal geometry in surface topography analysis is still in a beginning stage. Ling (1990, 1987) proposed an exponential law based on experimental results, and discussed several potential advantages of using fractals for the study

of boundary lubrication. Majumdar (1990, 1989) proposed a fractal surface model based on Weierstrass-Mandelbrot functions to characterize rough surfaces, and gave two major applications in surface contact conductance and electromagnetic wave scattering by rough surfaces. Some other approaches using fractals in engineering analysis of surfaces were also reported (Gagnepain and Roques-Carmes, 1986; Kaye, 1986; Roques-Carmes, et al., 1988; Dauw, et al., 1990). These studies represent attempts to introduce fractals as means of characterizing rough surfaces and they include various methods for computing fractal dimensions. Although a good start has been made in applying fractal geometry to the study of surface topography, there is still much work to do in determining the extent to which fractals can be used to characterize and model surfaces.

3.4. Fractals in Machined Surfaces

Fractal geometry provides an excellent description of many natural shapes. Examples of fractal geometry have been found in the study of coastlines. The features of naturally occurring shapes are often complex and hard to describe by conventional methods, but they sometimes possess a remarkable invariance under changes of magnification. This invariance, which is called self-similarity, may only be valid in a statistical sense, and it is the essential quality of fractals in nature. Fractals are quantified by the fractal dimension D.

Most surfaces used in engineering are initially formed by solidification of a liquid, fracture of a solid, or deposition of materials. These surfaces then undergo multi-event processes such as forming, electric discharge machining, waterjet cutting, and surface coating.

The final texture of the surface is a cumulative result of all the events which have occurred. It has been shown (Mandelbrot, 1982; Majumdar, 1990; Ling, 1990) that the surfaces formed by these processes produce fractal structures. The geometry of rough surfaces has a multi-scale property (Jordan et al., 1986), so it is of great importance to find a scale-independent characterization method to study surface topography. Currently, parameters such as root-mean-squares of height, slope, and summit curvature are commonly used for surface topography characterization. However, the variances of slope and summit curvature depend strongly on the resolution of the measuring instrument and filter (Thomas, 1982a). It is also known that surface topography is non-stationary, therefore the variance of the height is affected by the size of the sample (Sayles and Thomas, 1978). It often happens that for the same surface, instruments with different resolution and sampling length will yield different parameter values.

Fractal dimension is scale invariant, and it yields a robust numerical measure of surface topography, no matter what the instrument resolution and sampling length are. It appears that fractal geometry provides a more reliable and natural method for analyzing surface topography than do conventional methods.

CHAPTER 4

FRACTAL CHARACTERIZATION OF SURFACE TOPOGRAPHY AND IMPLEMENTATION IN SURFACE CONTACT

4.1 Introduction

It has been known from chapter 3 that fractal geometry can be used for surface characterization and that machined surfaces are fractals. A logical step is to model a random surface by fractal geometry and to find the relation of fractal geometry with the conventional surface characterization method. The objectives of this study are to find new applications of fractals to the characterization of surface topography and to uncover insights into the physical significance of fractal parameters in these applications. After reviewing some basic notions in fractal geometry, we postulate a model for surface profiles based on Gaussian random functions. Our model includes the fractal dimension D and the topothesy L as the parameters. It is shown that our model predicts that D has a strong relationship to and L has a relatively weak influence on the bearing area curve. The prediction has been confirmed by experiments. This study indicates that our approach may very well play a useful role in surface contact mechanics.

4.2 Gaussian Random Fractal Modeling of Surface Topography

We shall now describe the mathematical model which will be used to characterize the topography of the surfaces under consideration. This model will then be used to analyze features of surfaces in engineering applications; in particular, we shall make some predictions about the qualitative relationship between the model parameters and bearing area curves.

4.2.1 The Model

Let the surface studied be a rectangle with sides of length a>0 and b>0. We introduce a Cartesian coordinate system so that this sample occupies the planar region

$$R_0 = [0, a] \times [0, b] = \{(x, y) \in \Re^2 : 0 \leq x \leq a, 0 \leq y \leq b\} \qquad (4.1)$$

The surface topography for this sample can be represented by a continuous function $\Phi_0 : R_0 \rightarrow \Re$, so that the surface patch under consideration can be defined by

$$\Theta_0 = \{\Phi_0(x, y) : (x, y) \in R_0\} \qquad (4.2)$$

It is mathematically convenient to extend the surface to the whole plane in a symmetric fashion as follows: We first extend Φ_0 to Φ_1 on $R = [-a, a] \times [-b, b]$ according to the formula

$$\Phi_1(x, y)=\begin{cases}\Phi_0(x, y), & 0\le x\le a,\ 0\le y\le b\\ \Phi_0(-x, y), & -a\le x\le 0,\ 0\le y\le b\\ \Phi_0(-x, -y), & -a\le x\le 0,\ -b\le y\le 0\\ \Phi_0(x, -y), & 0\le x\le a,\ -b\le y\le 0\end{cases} \tag{4.3}$$

Next, we extend continuously along radial directions so that it is zero on the circle

$$x^2 + y^2 = (r_0 + c)^2$$

and beyond. Here $c = (a^2 + b^2)^{1/2}$ and $r_0 > 0$ is a parameter which will be specified in the sequel. To be more precise, we define $\Phi : \Re^2 \to \Re$ by the formula

$$\Phi(x, y) = \begin{cases}\Phi_1(x, y), & (x, y) \in R\\ \rho\Phi_1(x_0, y_0), & (x, y) \notin R,\ x^2 + y^2 < (r_0 + c)^2\\ 0, & x^2 + y^2 \ge (r_0 + c)^2\end{cases} \tag{4.4}$$

where in the middle entry (x_0, y_0) is the point at which the ray from the origin to (x, y) intersects the boundary of R and ρ is equal to $(r_0 + c) - (x^2 + y^2)^{1/2}$ divided by $(r_0 + c) - (x_0^2 + y_0^2)^{1/2}$. Thus we may assume that our sample of the surface is defined over the whole plane by $\Theta = \{\Phi(x, y) : (x, y) \in \Re^2\}$. Note that $\Phi : \Re^2 \to \Re$ is a bounded, continuous function which agrees with Φ_0 on R_0 and vanishes when $x^2 + y^2 \ge (r_0 + c)^2$.

We shall use a Gaussian random function (Rice, 1944, 1945; Berry, 1979) to model the topography Φ of the surface Θ. The plausibility of such a Gaussian model can be argued on at least two levels: On physical grounds, the formation of many types of surfaces can be viewed as deriving from the cumulative effects of a large

number of essentially independent factors which tend to be random and have similar distributions; hence, the viability of a normally distributed model can be inferred from the central limit theorem. In addition, Gaussian models have already been used successfully to predict surface phenomena, as for example in the study of rough surface scattering in Berry (1979). Now to our definition: define Q = [-d, d]x[-d, d] to be a square with d so large that Q contains the disk $\{(x, y): x^2 + y^2 \geq (r_o + c)^2\}$ in its interior. Let Z: Q $\rightarrow \Re$ be a continuous random variable with the following properties:

(i) For every allowable ξ, the random variable $\Delta(x, \xi) = Z(x + \xi, \bullet) - Z(x, \bullet)$ defined on $-b \leq y \leq b$ is normally distributed with mean $m(\alpha, L, \xi) = t|\xi|[(\frac{3-\alpha}{2}) - sL]$ and standard deviation $L^{\frac{3-\alpha}{2}} |\xi|^{\frac{\alpha-1}{2}}$; i.e.,

$$P(\Delta(x, \xi) \leq z) = (2\pi L^{3-\alpha} |\xi|^{\alpha-1})^{-\frac{1}{2}} \int_{-\infty}^{z} \exp\left[\frac{-(\zeta-m)^2}{2L^{3-\alpha}|\xi|^{\alpha-1}}\right] d\zeta \quad (4.5)$$

where α and L are real parameters such that $1< \alpha <3$ and $0 < L$, t ($t<<1$) is a positive scaling parameter indicative of the nominal thickness of the sample, s is a small positive parameter with dimension (micrometers)$^{-1}$, and P denotes the usual probability measure. Z(x, •) denotes the function of y obtained by fixing the first argument of Z at x.

(ii) For every allowable η, the random variable $\Delta(y, \eta) = Z(\bullet, y+\eta)-Z(\bullet, y)$ defined on $-a \leq x \leq a$ is normally distributed with mean $m(\alpha, L, \eta) = t|\eta|[(\frac{3-\alpha}{2}) - sL]$ and standard deviation $L^{\frac{3-\alpha}{2}} |\eta|^{\frac{\alpha-1}{2}}$; i.e.,

$$P(\Delta(y, \eta) \le z) = (2\pi\, L^{3-\alpha} |\eta|^{\alpha-1})^{-\frac{1}{2}} \int_{-\infty}^{z} \exp\left[\frac{-(\zeta-m)^2}{2L^{3-\alpha}|\eta|^{\alpha-1}}\right] d\zeta \quad (4.6)$$

where $Z(\bullet, y)$ denotes the function of x obtained by fixing the second argument of Z at y.

(iii) $\Phi = Z$ on Q and $r_0 = 1$.

The parameter α is related to the fractal dimension of the profiles of the surface topography and it can be proved (Falconer, 1990) that it is also associated with the power spectra of the profiles by the asymptotic formula

$$S(\omega) \sim \frac{q}{\omega^{\alpha}}, \text{ as } |\omega| \to \infty \quad (4.7)$$

It is shown in Berry (1979) that the structure functions of the profiles satisfy (3.7). As mentioned in the preceding section, the parameter L is called the *topothesy* of the surface. We shall refer to the model defined by (i) - (iii) as the *Gaussian fractal model.*

We shall confine our attention to surface profiles along lines parallel to the x-axis. A typical profile is defined by selecting and fixing a $y_0 \in [0, b]$, so that the corresponding profile is represented by the function $\phi(x) = Z(x, y_0)$.

Using (ii), (iii) and the fact that $\Phi(\bullet, -(1+c)) = 0$, we compute that

$$P(\phi \le z) = P(Z(\bullet, y_0) \le z) = P(Z(\bullet, y_0) - Z(\bullet, -(1 + c)) \le z) \quad (4.8)$$

so

$$P(\phi \le z) = (2\pi L^{3-\alpha} \gamma^{\alpha-1})^{-\frac{1}{2}} \int_{-\infty}^{z} \exp\left[\frac{-(\zeta-m)^2}{2L^{3-\alpha}\gamma^{\alpha-1}}\right] d\zeta \qquad (4.9)$$

where $\gamma = y_0 + 1 + c$. Thus ϕ is normally distributed with mean $m = t[(\frac{3-\alpha}{2}) - sL]\gamma$ and standard deviation $\sigma = L^{\frac{3-\alpha}{2}} \gamma^{\frac{\alpha-1}{2}}$; from which we infer that the profile is an example of a nonstationary random process such that the height distribution has a variance ($= \sigma^2$) which increases with sample size c. This observation is in agreement with the conclusions of Sayles & Thomas (1978).

A few words are in order concerning our choice for the mean in the fractal model. It can be seen from a careful inspection of rough surface data in such references as Majumdar & Bhushan (1990) and Thomas (1982b) that typical height distributions of profiles do not, in general, have mean zero. Therefore, it makes sense to postulate a nonzero function of parameters for the mean. The simplest such function, of course, is linear in the parameters α and L. As we shall show in the sequel, $(\frac{3-\alpha}{2})$ is equal to D-1, where D is the fractal dimension, hence it seems reasonable to single out this expression in the mean function. It is reasonable to assume that a flat (non-fractal) surface corresponds to D = 1 and L = 0 and thus the mean will be equal to zero. In view of these remarks, m should be of the form

$$m = c_1(\frac{3-\alpha}{2}) + c_2 L \qquad (4.10)$$

which corresponds to our assumed form of the mean with $c_1 = t\gamma$ and $c_2 = -st\gamma$. Observe that the factors $|\xi|$ and $|\eta|$ in the means of $\Delta(x, \xi)$ and $\Delta(y, \eta)$, respectively, guarantee that the corresponding means go to zero with ξ and η as they should. We have assumed that the coefficient $t\gamma$ is positive and $-st\gamma$ is negative. These choices are based on an inspection of experimental data in the literature and the following mathematically plausible rationale: An increase in the fractal dimension corresponds, in a certain sense, to an increase in the length of the graph of the surface profile ϕ, and as this length increases, a greater portion of points on the graph are forced to lie at larger heights. L can be viewed as a measure of randomness superimposed on a typical fractal profile, and this randomness tends to move profile points to smaller heights. This rather intuitive argument concerning choice of signs is not really essential, because we can simply use profile data to estimate the coefficients independent of any preconceptions about their positions on the real line.

We shall use the surface profile data to estimate the model parameters as follows: Let the measured height distribution data be $z_1,..., z_n$. From this data we can compute $D\text{-}1 = \frac{3-\alpha}{2}$ and L using the structure function method in the preceding section. One obvious equation for the coefficients is

$$m = t\gamma[(D-1) - sL] = \frac{1}{n}\sum_{k=1}^{n} z_k \tag{4.11}$$

Another such equation is

$$[2\pi L^{2(D-1)}\gamma^{2(2-D)}]^{-\frac{1}{2}} \int_{-\infty}^{\infty} \zeta^2 \exp\left(\frac{-(\zeta-m)^2}{2L^{2(D-1)}\gamma^{2(2-D)}}\right)d\zeta =$$

$$= L^{2(D-1)}\gamma^{2(2-D)} + m^2 = \frac{1}{n}\sum_{k=1}^{n} z_k^2 \tag{4.12}$$

From these equations we may solve for m and γ.

If we want to estimate the coefficients in m, we can consider several rough surfaces on samples having the same physical properties and dimensions. To illustrate this, let $\{z_k^{(i)}\}$, $1 \le i \le N$ represent height distribution data from N profiles. Let the corresponding fractal parameters be $D^{(i)}$, $L^{(i)}$, $1 \le i \le N$. Then we can estimate c_1 and c_2 by the least-square solution of the equations

$$m^{(i)} = c_1(D^{(i)} - 1) + c_2 L^{(i)} = \frac{1}{n}\sum_{k=1}^{n} z_k^{(i)} \tag{4.13}$$

4.2.2 Normalized Bearing Area Curve and Fractal Parameters

The concept of the bearing area curve of a surface topography was introduced by Abbott (1933), and six decades of engineering practice have shown that it provides the best qualitative measure of the area of contact between two surfaces, and thus of the rate of wear of two

abutting surfaces which are in motion relative to each other. Figure 4-1 illustrates the bearing area curve which is obtained from the bearing ratio

$$t_h = P(z \geq h) = \int_h^{\infty} p(\tau)d\tau \qquad (4.14)$$

where z is the profile height, p is the probability density of the height, and h is the cutting height from the reference line M-M. By plotting t_h over a range of discrete heights h for a profile, one obtains the bearing area curve as shown in Figure 4-1. For purposes of comparison, we introduce the normalized bearing area curve. In practice, the exact nature of the height distribution of a profile is usually not known, so the normalized bearing area curve can be obtained experimentally as follows: A rather large number of heights are measured over the profile and then scaled (or normalized) by setting the minimum and maximum heights equal to zero and one, respectively. Then the true normalized bearing area curve is approximated by the complementary cumulative frequency distribution of the normalized height data.

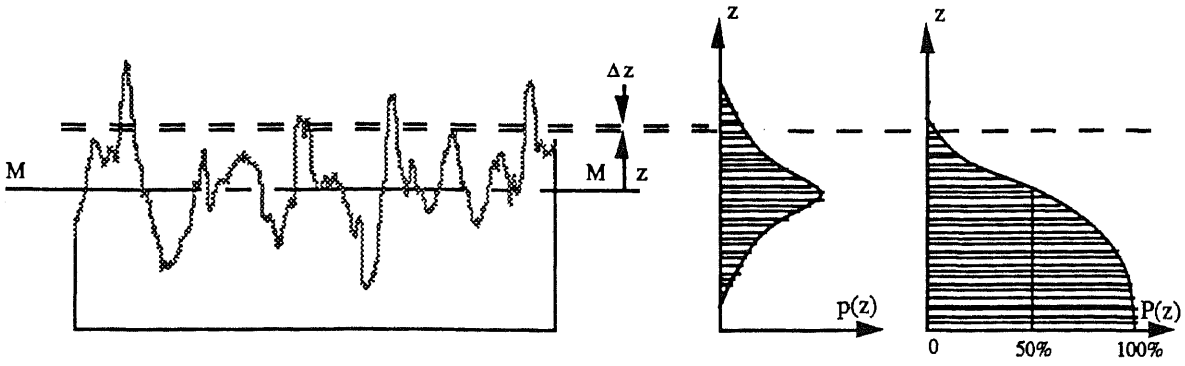

Figure 4-1 Construction of bearing area curve

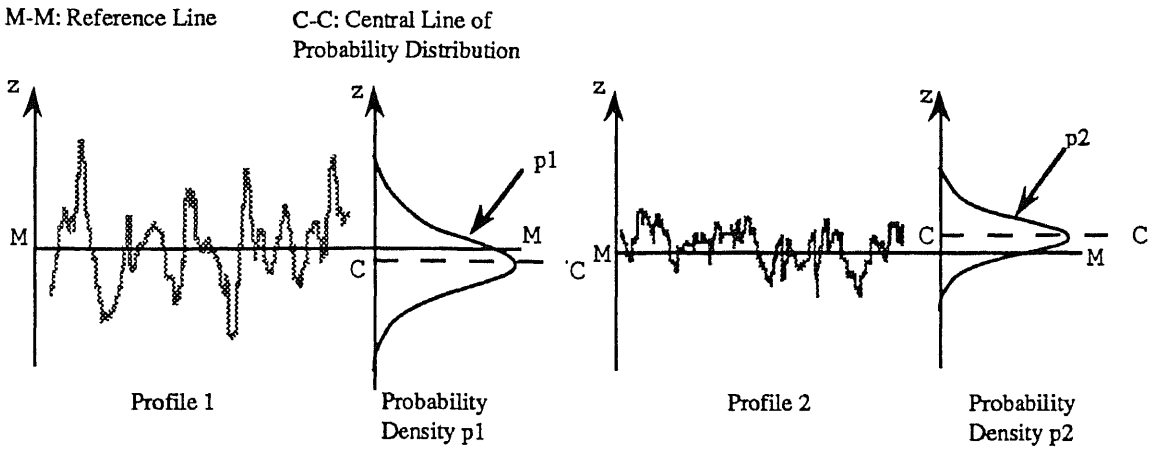

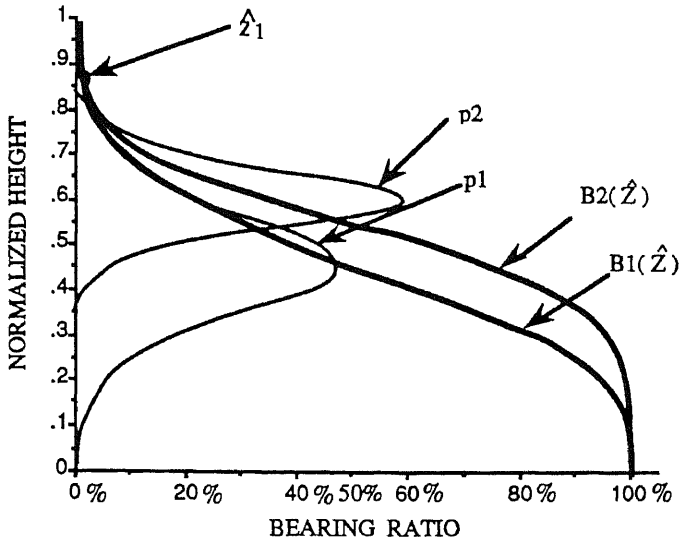

Figure 4-2 Relation between fractal dimension and bearing area curve

It is of interest to determine the relationships between the parameters α and L of the Gaussian fractal model and the bearing curves of the surface profiles. Using standard techniques from fractal geometry, it can be proved (Falconer, 1990) that the graph of the profile function ϕ almost surely has both Hausdorff and box dimension equal to $\frac{5-\alpha}{2}$. By almost surely, we mean that the set of y_o values for which this dimension statement is invalid has probability measure equal to zero. Defining the fractal dimension D to be the common value of the Hausdorff and box dimensions, which are denoted by $\dim_H$ and $\dim_B$, respectively, we have

$$D = \dim_H(\text{graph } \phi) = \dim_B (\text{graph } \phi) = \frac{5-\alpha}{2},$$

almost surely, and hence (4.9) can be rewritten in the form

$$P(\phi \le z) = [2\pi L^{2(D-1)} \gamma^{2(2-D)}]^{-\frac{1}{2}} \int_{-\infty}^{z} \exp\left(\frac{-(\zeta-m)^2}{2L^{2(D-1)}\gamma^{2(2-D)}}\right) d\zeta \quad (4.15)$$

We note here that m can be rewritten as a function of D and L as follows:

$$m(D , L) = t\gamma[(D-1) - sL] = t(1+y_o+c)[(D-1) - sL] \quad (4.16)$$

Thus $\phi = Z(\bullet, y_0)$ has a normal distribution with mean m and standard deviation

$$\sigma = \sigma(D, L) = \left(\frac{L}{\gamma}\right)^{(D-1)}\gamma = \left(\frac{L}{1+y_o+c}\right)^{(D-1)} (1+y_o+c) \quad (4.17)$$

We compute that:

$$\frac{\partial m}{\partial D} = t\gamma \quad \text{and} \quad \frac{\partial m}{\partial L} = -st\gamma \tag{4.18}$$

As $1<D<2$ and $0<L<1$ (μm) for most surface profiles encountered in engineering applications, it is clear that m is a strictly increasing function of the fractal dimension and a strictly decreasing function of the topothesy over the range of values of D and L. Similarly, we compute that

$$\frac{\partial \sigma}{\partial D} = \left(\frac{L}{\gamma}\right)^{(D-1)} \gamma \log\left(\frac{L}{\gamma}\right) \tag{4.19}$$

which is negative over this range of parameters (note that $L < 1 < \gamma = 1+y_o+c$). On the other hand, σ is a strictly increasing function of the topothesy L satisfying

$$\frac{\partial \sigma}{\partial L} = (D-1)(L/\gamma)^{(D-2)} \tag{4.20}$$

In order to relate the fractal parameters to the bearing area curve for our model, we assume that only D and L are allowed to vary for the surface sample under consideration. Suppose that we measure profiles for two samples and find that the fractal parameters are (D_1, L_1) and (D_2, L_2), respectively. The height distribution data is used to obtain the corresponding normalized

bearing area curves $B_1(\hat{z})$ and $B_2(\hat{z})$, where $\hat{z}$ is the normalized height $0 \le \hat{z} \le 1$. If the sample size for each profile is sufficiently large, then the resulting cumulative frequency distribution will be essentially unchanged by the addition of two arbitrarily chosen points to each sample. Hence, we may assume that both samples have the same minimum and maximum heights, so that the same scale factor, which we denote by k, can be used to normalize the height data between zero and one. It may also be assumed that the height interval from minimum to maximum is large enough to contain three σ–bounds on both sides of the means of both distributions. Then we scale each data set and associated Gaussian model as shown in Figure 4-2 in order to obtain the normalized height distributions. Let p_1 and p_2 be the respective probability density functions for the normalized height distribution. Then the normalized bearing area ratios are

$$B_1(\hat{z}) = \int_{\hat{z}}^{1} p_1(\tau)d\tau \quad \text{and} \quad B_2(\hat{z}) = \int_{\hat{z}}^{1} p_2(\tau)d\tau \qquad (4.21)$$

Let $m(D_1, L_1)$, $\sigma(D_1, L_1)$ and $m(D_2, L_2)$, $\sigma(D_2, L_2)$ be the means and standard deviations of the height distributions of the two profiles. It is clear from the model that if $m(D_1, L_1) < m(D_2, L_2)$, then there exists a $\hat{z}_1$ (see Figure 4-2) which is near one such that $B_1(\hat{z}) < B_2(\hat{z})$ for all $0 \le \hat{z} \le \hat{z}_1$. This observation leads naturally to a prediction about the relationship between the fractal parameters and the bearing area curve as follows:

Prediction: *The Gaussian fractal model for surface topography*

defined by (i)-(iii) implies that for two profiles the bearing area curves satisfy $B_1(\hat{z}) < B_2(\hat{z})$ *for all normalized heights* $0 \le \hat{z} \le \hat{z}_1$, *where* $\hat{z}_1$ *is a real number near one, whenever* $m(D_1, L_1) < m(D_2, L_2)$. *If* $s << 1$, *as we predict will be the case, the bearing area curves satisfy this property whenever* $D_1 < D_2$.

4.2.3 Topothesy and Ensemble Variance

The topothesy L can be shown to increase with increasing q in the asymptotic power spectrum formula (4.7), and so it can be viewed as a measure of the strength of each fractal surface profile. We compute that

$$\langle (Z(x+L, \bullet) - Z(x, \bullet))^2 \rangle = E[(Z(x+L, \bullet) - Z(x, \bullet))^2]$$
$$= (2\pi L^2)^{-\frac{1}{2}} \int_{-\infty}^{\infty} \zeta^2 \exp\left(\frac{-(\zeta - m)^2}{2L^2}\right) d\zeta = L^2 + m^2 \qquad (4.22)$$

where $\langle\ \rangle$ denotes the ensemble average of all profiles on the sample taken parallel to the x-axis and E denotes the mathematical expectation of the random variable. Thus, as noted in the preceding section, L can be identified as the distance over which a chord of a profile has an r.m.s. slope of one. There is another interpretation of L which is more directly related to the geometrical features of the surface profiles being investigated. Consider the ensemble of profiles $\{Z(\bullet, y) : 0 \le y \le b\}$ over the surface sample, and take $\phi = Z(\bullet, y_0)$ to be the base profile. It follows from (ii) that the distribution of the profile ensemble about ϕ has variance $L^{3-\alpha} |\eta|^{\alpha-1}$; hence, we have a

nonstationary random process for which L is a measure of the scattering of the ensemble of Gaussian random fractals about the base function ϕ as shown in Figure 4-3. Consequently, we may think of L as representing a secondary level of irregularity or roughness superimposed on the graph of ϕ whose primary fractal irregularity is characterized by the fractal dimension.

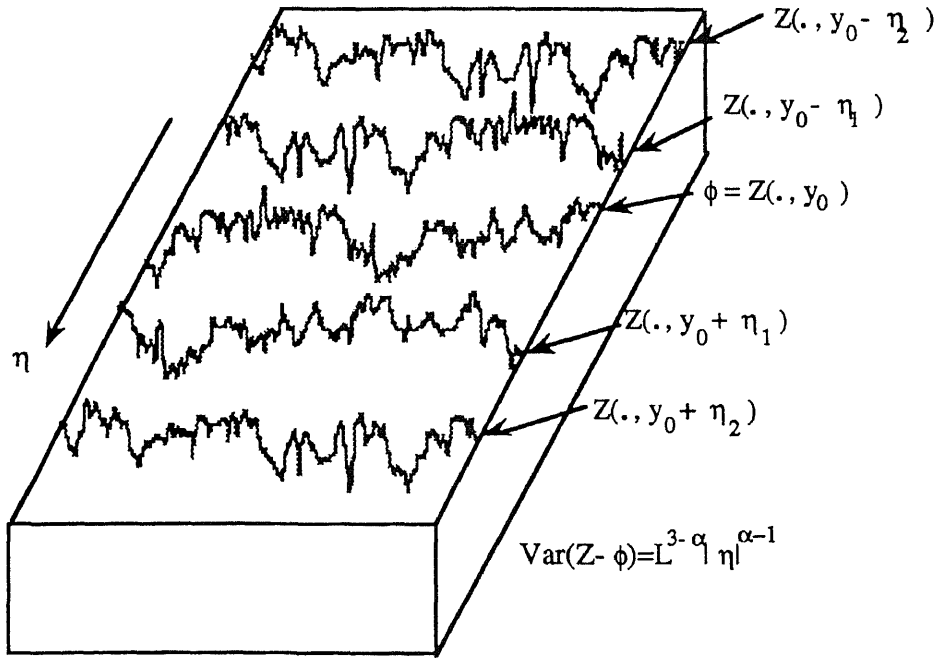

Figure 4-3 The ensemble of Gaussian random fractal profiles

4.3 Experimental Results and Discussion

We have performed measurements on several surface profiles in order to test the validity of the predictions based on our Gaussian model of surface topography and to better understand the physical significance of the fractal parameters D and L.

4.3.1 Relation of Fractal Dimension to Bearing Area Curve

Conventionally, the simplest and most widely recognized parameters of surface roughness are Average Height R_a, Root-Mean-Square Height R_q, and Maximum Peak-to-Valley Height R_{max} (ASME, 1985). It often happens that some surfaces have nearly equal values of R_a, R_q, and R_{max} but their surface features are quite different. For example, BR1 and BR2 in Figure 4-4 are two surface profiles generated by different machining methods. They have nearly equal values of R_a, R_q, or R_{max}. However, the two profiles are quite different. The peaks and valleys of BR2 are fewer and thinner than those of BR1. In wear the number and size of peaks and valleys of surfaces in contact are extremely important features.

The bearing area ratios of these surfaces are calculated by the following procedure. First the sampled profile height data are normalized between 0 and 1, with the lowest point being 0 and highest point being 1. Then the normalized height range is divided into 20 equal divisions. For each division the probability of the height data is computed by dividing the number of data points in this range by the total number of data points. The cumulative

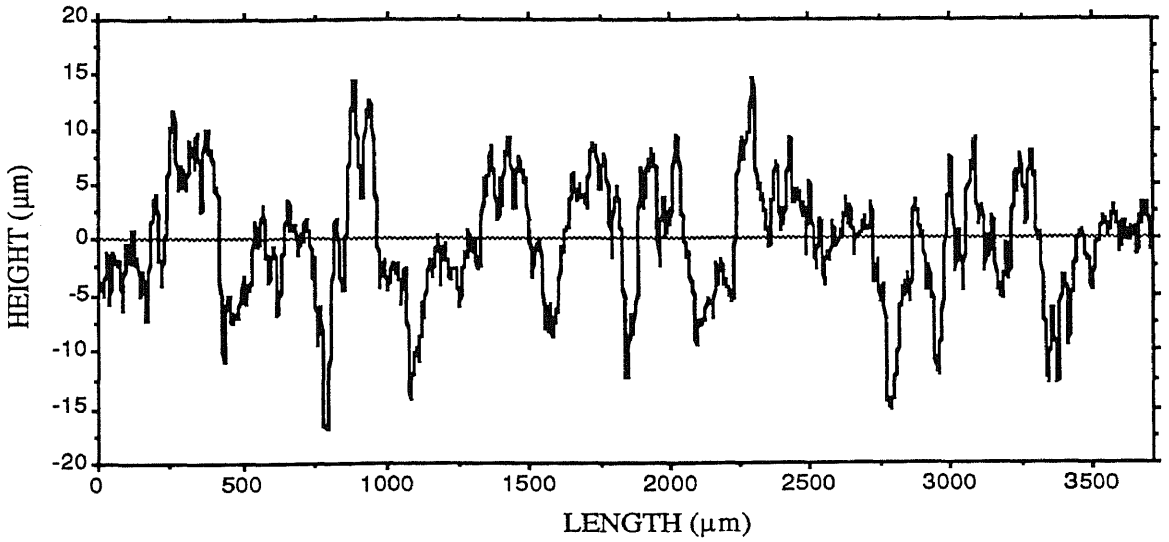

(a)

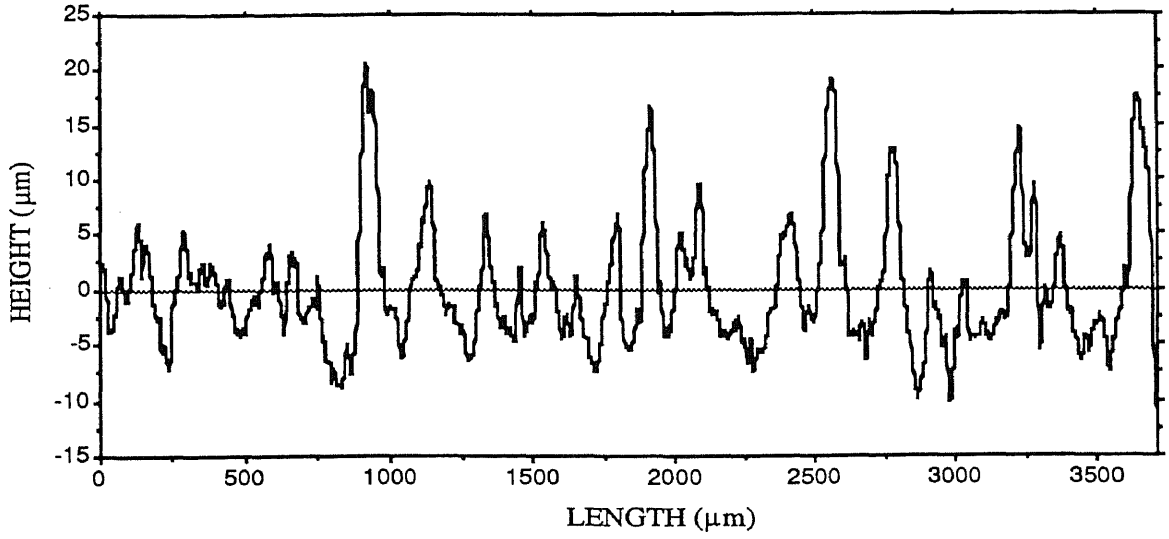

(b)

Figure 4-4 Two profiles having nearly equal values of conventional roughness parameters but different features: (a) profile BR1 generated by waterjet cutting, R_a = 4.26μm, R_q = 5.35μm, and R_{max} = 31.6μm and (b) profile BR2 generated by electrical discharge machining, R_a = 4.25μm, R_q = 5.68μm, and R_{max} = 33.1μm.

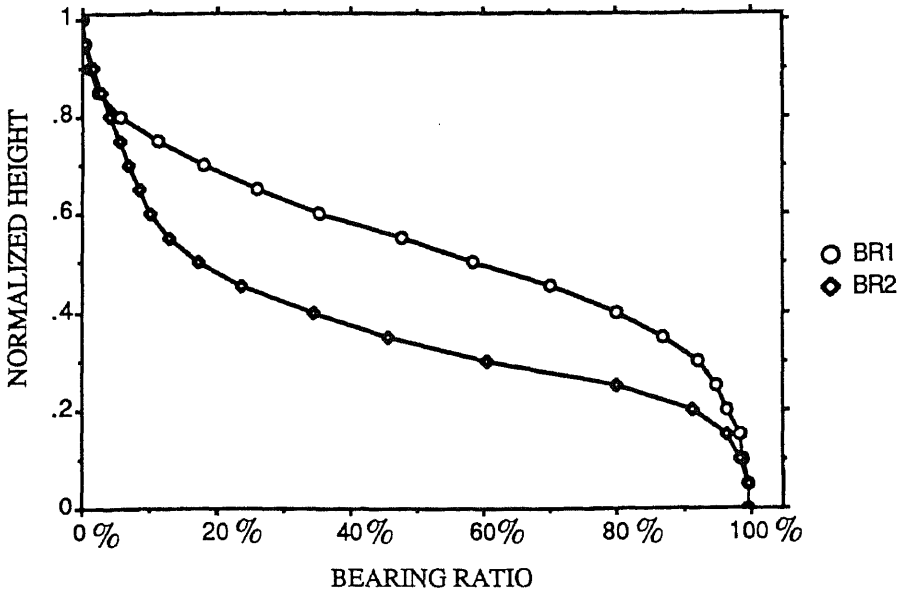

Figure 4-5 Bearing area curves of BR1 and BR2. Their fractal parameters are D_{BR1} = 1.47, L_{BR1} = 0.53 μm and D_{BR2} = 1.34, L_{BR2} = 0.177 μm.

density function forms the bearing area curve. It can be seen from Figure 4-5 that the bearing area curve of BR1 is above that of BR2. This implies that when the surfaces are in contact BR1 has more contact area, i.e. the surface support ability of BR1 is greater than that of BR2.

Another example is given by the two profiles in Figure 4-6. The parameter values of R_a, R_q, and R_{max} for BR3 and BR4 are nearly identical. This time, however, the two profiles are not so obviously different as in Figure 4-4. Figure 4-7 shows their bearing area curves, which imply that BR4 has weaker support ability in surface contact than does BR3.

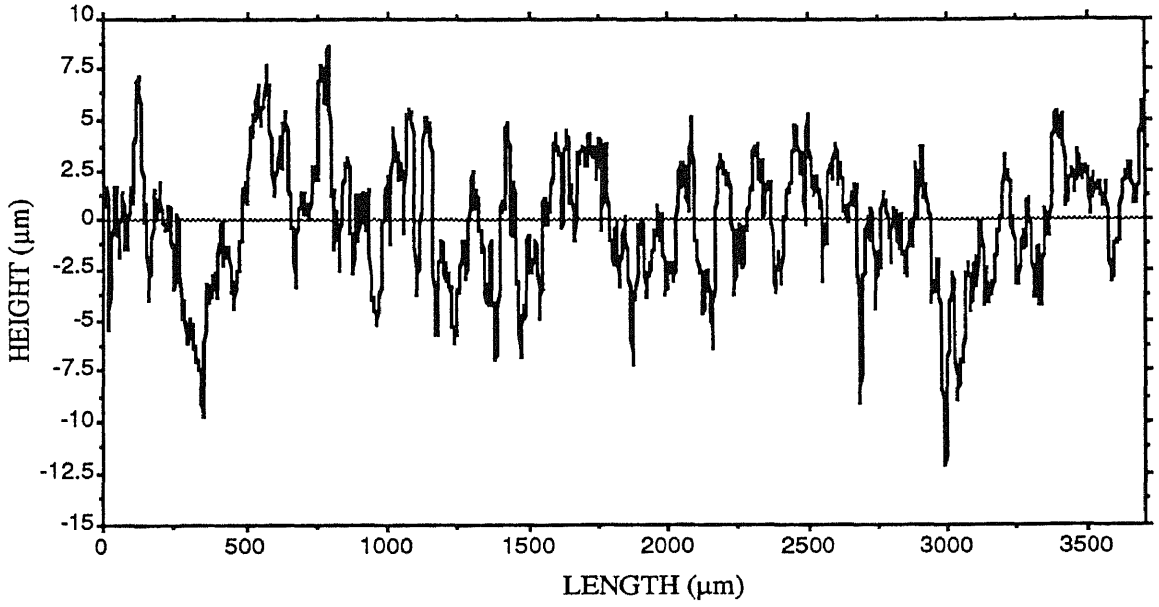

(a)

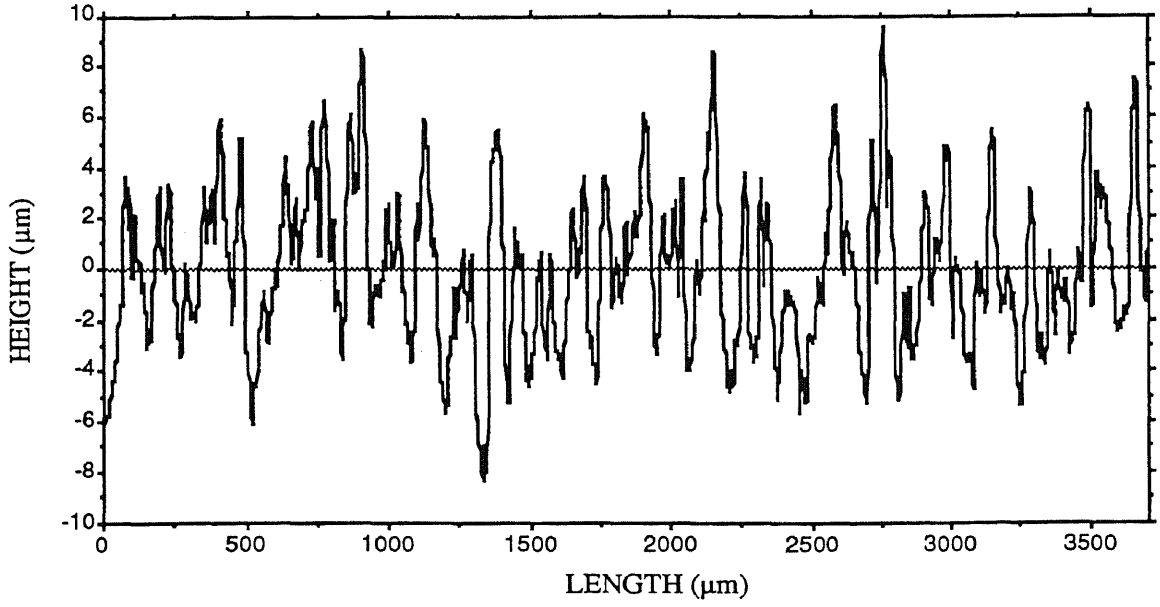

(b)

Figure 4-6 Another two profiles having nearly equal values of conventional roughness parameters but different features: (a) profile BR3 generated by waterjet cutting, R_a = 2.52 μm, R_q = 3.15 μm, and R_{max} = 21.0 μm and (b) Profile BR4 generated by electrical discharge machining, R_a = 2.55 μm, R_q = 3.158 μm, and R_{max} = 22.0 μm.

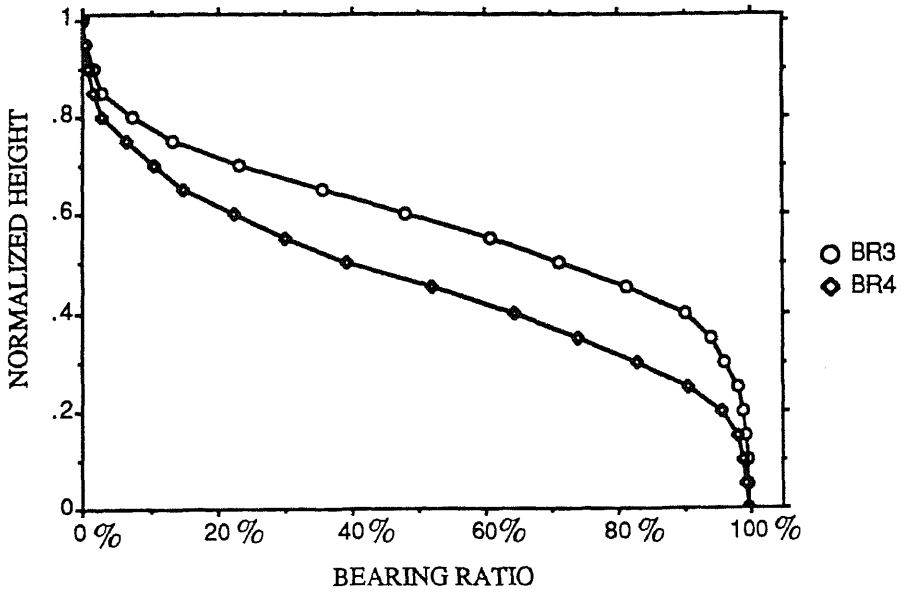

Figure 4-7 Bearing area curves of BR3 and BR4. Their fractal parameters are D_{BR3} = 1.50, L_{BR3} = 0.318 μm and D_{BR4} = 1.42, L_{BR4} = 0.189 μm.

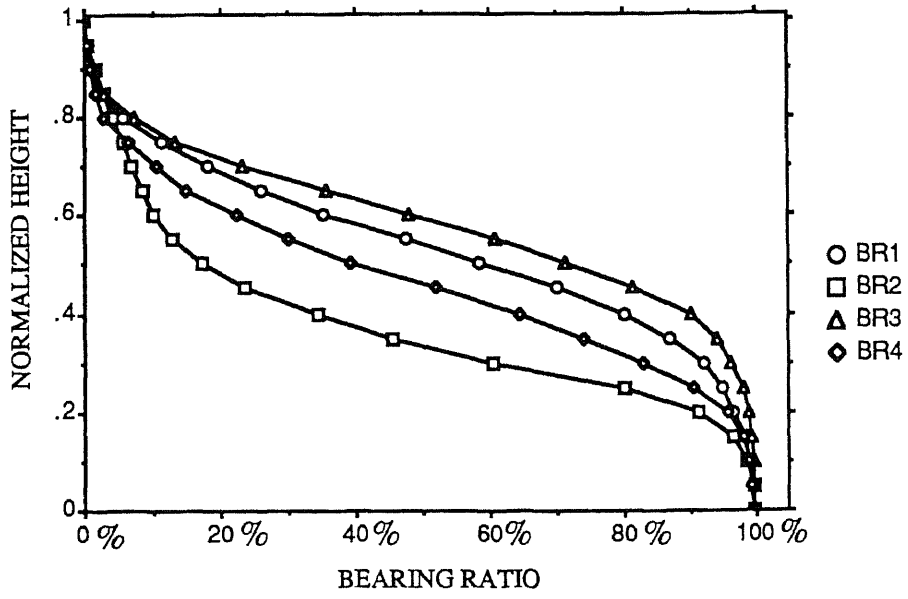

Figure 4-8 Bearing area curves of BR1, BR2, BR3, and BR4 surfaces. Note that $D_{BR3} > D_{BR1} > D_{BR4} > D_{BR2}$ (refer to Figures 4-4, 4-7).

Fractal dimension is a useful measure of surface contact support ability like the bearing area curve. It has an advantage over the bearing area curve in that it characterizes the surface contact support ability by a single number. It is very interesting that not only $D_{BR1} > D_{BR2}$ and $D_{BR3} > D_{BR4}$ in agreement with the sizes of the respective bearing area curves and support abilities, but that the agreement applies to all of the four surfaces, even though the R_a, R_q, and R_{max} values of BR1 and BR2 are very different from those of BR3 and BR4 (refer to Figure 4-8).

The bearing area curves of the three EDM surfaces in Figure 3-6 are plotted in Figure 4-9, which also provides the values of fractal parameters for three surfaces. Again, the fractal dimension has a good agreement with the bearing area curve in characterizing the contact support ability of a surface. As a further test of the predicted dominance of D over L in determining bearing area curves, the data from five EDM samples were used to estimate c_1 and c_2 via (4.13). We found that $c_1 = 0.221$ and $c_1 = -0.0756$. Thus our experimental results are in complete agreement with the Gaussian fractal model with regard to the relationship between fractal dimension and the bearing area curve.

4.3.2 Relation of Topothesy to Bearing Area Curve

Topothesy, which has units of length, can reflect information related to surface height deviation. This relationship was also indicated in the prediction in Section 3.2 using the Gaussian fractal model. In the experimental investigation of this relationship, we use

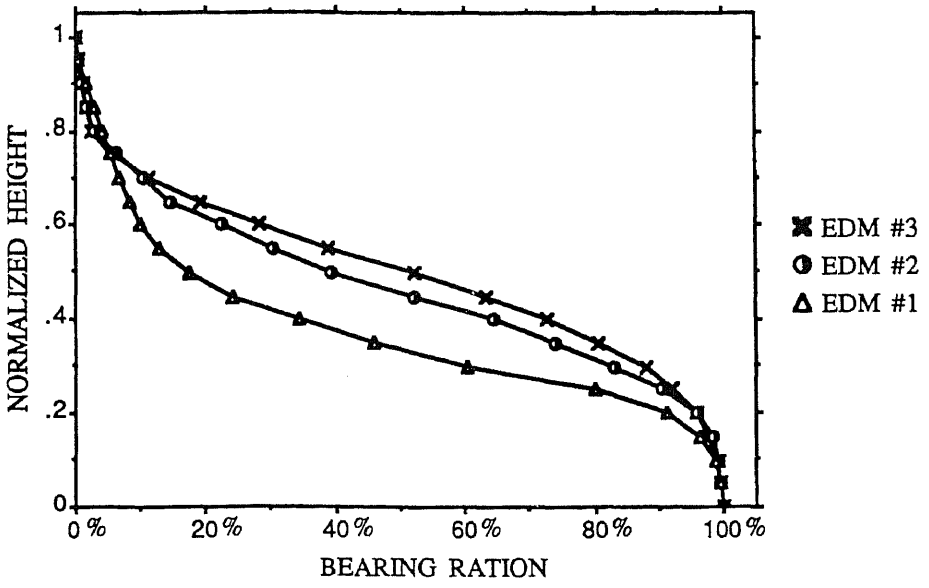

Figure 4-9 Bearing area curves of three EDM surfaces. Their fractal parameters are EDM #1: D = 1.252, L = 0.0516 μm; EDM #2: D = 1.385, L = 0.15 μm; EDM #3, D=1.546, L=0.237 μm.

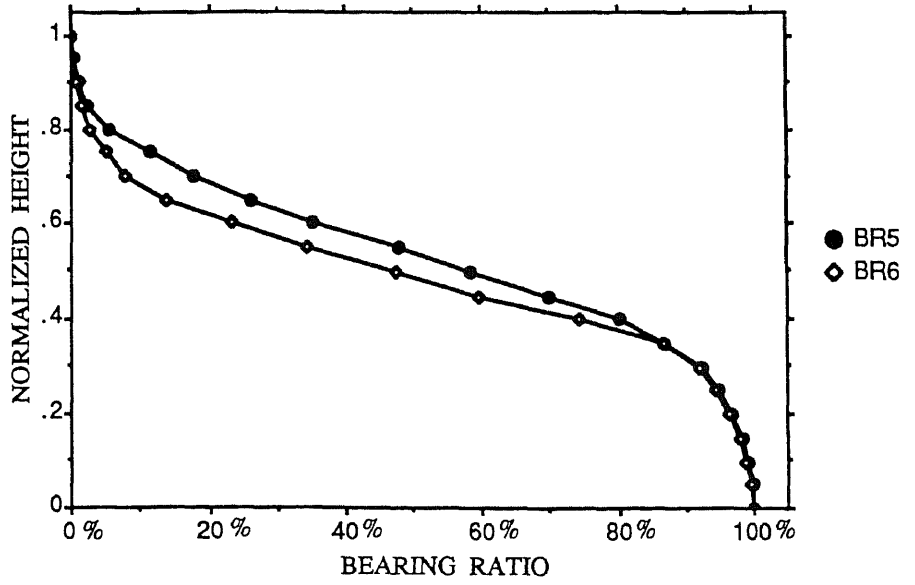

Figure 4-10 Bearing area curves of BR5 and BR6 surfaces. Their fractal parameters are D_{BR5} = 1.453, L_{BR5} =0.0368 μm, D_{BR6} = 1.466, L_{BR6}=0.564 μm.

two surfaces, one is treated by ion-nitriding coating (BR5) and the other is made from waterjet cutting (BR6). They have nearly equal fractal dimensions: D_{BR5} = 1.453 and D_{BR6} = 1.466, but very different topothesies: L_{BR5} = 0.0368 μm and D_{BR6} = 0.564 μm. Figure 4-10 shows that the bearing area curve of BR5 is above that of BR6. This agrees with the predicted relationship since $D_{BR5} \approx D_{BR6}$ and $L_{BR5} < L_{BR6}$. By comparing Figure 4-10 with Figures 4-8 and 4-9, it can be seen that the influence of L on the bearing area curve (and hence the surface contact support ability) is less than that of D, because an increase of L by 15 times produces a smaller difference in the bearing area curve than an increase of D by only a small percentage. Thus the fractal dimension is the primary parameter and the topothesy is the secondary parameter in determining the surface contact support ability. This is consistent with the general agreement among the researchers that the fractal dimension is the major property indicator in surface topography, while the topothesy only reflects small-scale variations.

4.4 Chapter Conclusions

Based on the Gaussian fractal model, we have derived equations to relate the bearing area curve with the fractal dimension D and topothesy L. This analysis leads to the prediction that the bearing area curve shifts higher as D increases or L decreases. The experimental results obtained from a number of waterjet cut, electric discharge machined, and ion-nitriding treated surfaces verify this prediction. The study further reveals that D has a larger effect on the surface contact support ability than L. Thus the fractal dimension can

replace the bearing area curve used in the conventional method for the study of surface contact and wear, and it is more concise and practical since it provides a simple quantitative measure of the contact support ability of surfaces.

The Gaussian fractal model appears to offer a very promising approach to the analysis of surface topography. It also provides additional evidence of the usefulness of fractal geometry for the study of surfaces in engineering applications. Now that fractal geometry has been shown to be useful in describing surface contact and wear both theoretically and experimentally, a logical next step is to find a fractal geometry model for the prediction and control of wear. This will be discussed in the next chapter.

CHAPTER 5

FRACTAL GEOMETRY MODEL FOR WEAR PREDICTION AND APPLICATIONS IN WEAR TESTING

5.1 Introduction

Wear is a process that involves surface contact, stress action, and surface degradation. As a measure of damage to or material removed from a solid surface, wear can be considered to be the result of the surface being stressed mechanically, thermally, and chemically. The cost of wear in the United States has been estimated in the tens of billions of dollars per year. There has been a continuing research effort to gain improved understanding of wear phenomena, to predict wear behavior, and to control wear processes.

When two rough, nominally flat surfaces are brought together, surface roughness causes contact to occur at discrete contact spots. The true contact area is the accumulation of areas of the individual contact spots. For most metals at normal loads this will be only a few percent of the apparent contact area (Greenwood and Tripp 1970). A significant aspect of contact mechanics is that deformation occurs in the region of the contact spots which build up load-related stresses. Typical models of surface deformation are either elastic, plastic or mixed elastic-plastic, depending on nominal pressure, surface topography, and material constants.

Fractal geometry as a tool for the characterization of surface topography has gained much attention in recent years (Gagnepain and Roques-Carmes 1986; Ling 1990; Majumdar and Bhushan 1990).

This is due in part to the observations that fractal geometry can reflect the natural and intrinsic property of random phenomena (Mandelbrot 1982; Peitgen and Saupe 1988; Kaye 1989) and that it can overcome several disadvantages of conventional statistics and random process methods of surface analysis (Majumdar and Bhushan 1990). These advantages suggest, for example, that fractal geometry can be applied to surface contact mechanics. Majumdar and Bhushan (1991) explored these applications in a pioneering study. They gave a fractal representation of surface contact area and derived a fractal model of surface contact mechanics. In chapter 4 a fractal model, which has a clear connection with conventional method for studying surface topography, is developed. This model leads to a concise quantitative representation of the bearing area curve, and it strongly suggests the applicability of fractal geometry to surface contact and wear process analysis.

The objective of the study in this chapter is to establish a fractal model for wear prediction, with which to study the effects of fractal geometry parameters on wear rate.

5.2 Physical Interpretation of Fractal Geometry Parameters

Fractal geometry reveals natural properties of random and unpredictable phenomena. The fractal dimension, D, is the most important aspect of fractals. For different fractal phenomena, the fractal dimension parameter may characterize different properties of fractal sets. For surface topography characterization, fractal parameters can be related to a conventional concept, the normalized

bearing area curve. From the modeling of and experiments with fractal surfaces, it is concluded (see chapter 4) that if D increases or the topothesy L decreases, the normalized bearing area curve will shift higher and that D has a larger effect on the normalized bearing area curve than L. It is well known that the bearing area curve is an indicator of surface contact support ability: the higher the bearing area curve the stronger the contact support ability. Thus the fractal dimension can represent the bearing area curve used in conventional analysis for the study of surface contact and wear, and it is more concise and practical since it provides a simple quantitative measure of the contact support ability of surfaces: the larger the fractal dimension value the stronger the contact support ability.

5.3 Fractal Geometry and Wear Theory

By using the same fractal approach as that developed by Majumdar and Bhushan (1991) in the study of surface contact mechanics, here a fractal model for surface wear processes is developed. This model reveals interesting relationships between wear characteristics and fractal parameters.

5.3.1 Fractal Property of Islands

It has been shown by Archard (1980), Mandelbrot et al. (1984), and Majumdar and Bhushan (1990) that the microtopography of a machined surface is similar to a map of the earth's surface, which has islands in the various bodies of water. When a rough surface is in contact with a flat surface, the flat surface (like an ocean in the

formation of islands on the earth) cuts the rough surface and forms the contact area. This island analogy has been successfully used to study contact mechanics (Majumdar and Bhushan 1991), and we shall therefore employ it to analyze wear. Korcak (1938) proposed an empirical law which can be described as follows. If all the islands of a region are listed by size, then the total number N of islands of size A exceeding S satisfies the following relation:

$$N(A \geq S) = C_3 S^{-B} \tag{5.1}$$

where C_3 is a positive constant and B is a factor shown by Mandelbrot (1982) to be B=D/2, where D is the fractal dimension of the coastlines of the islands. Based on equation (5.1) it can be derived (Majumdar and Bhushan 1991) that the total area of all islands, A_r, can be expressed in terms of the fractal dimension as follows:

$$A_r = \frac{D}{2-D} S_L, \qquad 1 < D < 2 \tag{5.2}$$

where S_L is the area of the largest island.

5.3.2 Fractal Relation of Contact Spots and Asperities

The Weierstrass-Mandelbrot (W-M) function can be used to simulate a fractal surface profile and has the form (Berry and Lewis 1980; Majumdar and Bhushan 1990):

$$z(x) = G^{D-1} \sum_{n=n_1}^{\infty} \frac{\cos(2\pi\gamma^n x)}{\gamma^{(2-D)n}}, \quad 1 < D < 2; \ \gamma > 1 \tag{5.3}$$

where z(x) represents a fractal profile, D is the fractal dimension of the profile, γ is a frequency factor, n is an integer, n_l is the minimum number of n which is determined by the measuring length, and G is a factor called the scale amplitude by Majumdar (1990). It can readily be shown that $L = C_4G$, where C_4 is given by the formula

$$C_4 = \left[\frac{\Gamma(2D-3)\sin(\frac{\pi(2D-3)}{2})}{(2-D)}\right]^{1/(2D-1)} \tag{5.4}$$

For a given surface the fractal dimension D is a fixed number, and hence C_4 is a constant. Thus we see that G is directly related to the topothesy L.

It has been shown (Majumdar and Bhushan 1991) that the critical area S_c that distinguishes the elastic and plastic regimes can be expressed as

$$S_c = \frac{G^2}{(Q\sigma_y/2E)^{2/(D-1)}} \tag{5.5}$$

where σ_y is the yield strength, E is the elastic modulus and Q is a factor that relates the hardness H to the yield strength σ_y as $H = Q\sigma_y$.

If $S_L > S_c$, the real areas of contact in both elastic and plastic deformations need to be considered, and from Majumdar and Bhushan (1991) these contact areas are, respectively:

$$A_{re} = \frac{D}{2-D}(S_L - S_L^{D/2}S_c^{(2-D)/2}) \tag{5.6}$$

$$A_{rp} = \frac{D}{2-D} S_L^{D/2} S_c^{(2-D)/2} \qquad (5.7)$$

5.3.3 Adhesive Wear Theory

There exist many wear theories such as adhesive, abrasive, fatigue, corrosion, and delaminative theories (Archard 1953, 1980; Kruschov 1957; Suh 1973). The origin of all these is Archard's adhesive wear theory (1953). Archard's adhesive wear theory has been widely accepted and utilized (Stolarski 1990; Wu and Cheng 1991), since the derived relationship among the wear volume, sliding distance and contact area has been observed to agree well with experimental results. The mechanism of adhesive wear is consistent with our experimental setup of wear testing, and so we shall use it as the starting point of the analysis which follows. Adhesive wear can be described as follows: materials weld at sliding asperity tips, are transferred to the harder member, possibly grow in subsequent encounters, and are eventually removed by fracture, fatigue or corrosion. It is shown in (Archard 1953) that adhesive wear can be expressed in the form

$$V = KA_c d \qquad (5.8)$$

where V is the wear volume, K is a wear coefficient, A_c is the true contact area, and d is the sliding distance. The true contact area A_c has the relation $A_c = \frac{W}{p}$, where W is the load and p is the flow pressure under combined normal and tangential stresses. According to Tabor (1959) the flow pressure under a static load, p_m, is related

to p by

$$p^2 + 3s^2 = (p_m)^2 \tag{5.9}$$

where s is the shear strength. The adhesive theory of friction (Tabor 1959) leads to the expression

$$s = \frac{\mu W}{A_c} = \frac{T}{A_c} = \mu p \tag{5.10}$$

where T is the total friction force and μ is the coefficient of friction. Substituting (5.10) into (5.9) yields

$$p = \frac{p_m}{(1+3\mu^2)^{1/2}} \tag{5.11}$$

The wear equation now becomes

$$V = K(1+3\mu^2)^{1/2} A_r d \tag{5.12}$$

where $A_r = \frac{W}{p_m}$ is the true contact area under static loading.

As mentioned above, the model of surface deformation usually involves a combination of elastic and plastic effects. It is reasonable to assume that the total true contact area, A_r, is the sum of the elastic contact area, A_{re}, and the plastic contact area, A_{rp}, i.e.,

$$A_r = A_{re} + A_{rp} \tag{5.13}$$

This leads to the following wear volume equation

$$V = (1+3\mu^2)^{1/2} (K_e A_{re} + K_p A_{rp}) d \tag{5.14}$$

where K_e and K_p are the elastic and plastic wear coefficients, respectively.

Notice that in (5.14) the wear coefficient K has been decomposed into elastic and plastic components. It was pointed out by Archard (1980) and Stolarski (1990) that if the deformations are completely plastic, then K is essentially a probability coefficient which represents the cumulative effects of lubrication, sliding speed, temperature, chemical reactions, material properties, etc., and K is independent of the topographies of the surfaces which are in contact. For example, if $K=10^{-3}$ in a completely plastic wear process, then one in a thousand events results in a worn particle. It was, however, observed by Archard (1980) that an actual wear process also includes elastic deformations, and this will introduce a surface topography dependent element to K, i.e. K becomes an A_r dependent coefficient rather than a constant. By decomposing K into elastic and plastic parts, the coefficient K is replaced by the coefficients K_e and K_p, both of which are independent of the geometric features of the contacting surfaces. Thus K_e and K_p can be treated as probability constants. According to Archard's investigations, K varies widely, from 10^{-7} to 10^{-2} in unlubricated wear. If the deformations are completely plastic, the maximum value of K_p is 1/3. The value of K_e

in most wear processes is less than 10^{-3}.

5.4 Wear Prediction Model and Analysis

Here we shall develop a model that relates wear to fractal parameters. By substituting (5.6) and (5.7) into (5.9), the wear volume becomes

$$V=(1+3\mu^2)^{1/2}S_L\left[K_e(1-S_L^{(D-2)/2}S_c^{(2-D)/2})+K_pS_L^{(D-2)/2}S_c^{(2-D)/2}\right]d \quad (5.15)$$

With (5.2) and (5.5), equation (5.15) can be rewritten as

$$V=(1+3\mu^2)^{1/2}A_r\left[K_e-(K_e-K_p)\left(\frac{D}{(2-D)A_r}\frac{G^2}{(Q\sigma_y/2E)^{2/(D-1)}}\right)^{(2-D)/2}\right]d \quad (5.16)$$

For ease in analysis, we normalize the variables in (5.16) as follows:

$$V^*=\frac{V}{dA_a},\ A_r^*=\frac{A_r}{A_a},\ G^*=\frac{G}{(A_a)^{1/2}},\ \text{and}\ \psi=\frac{Q\sigma_y}{2E} \quad (5.17)$$

where A_a is the apparent contact area; V^* is the normalized wear rate; A_r^* is the normalized true contact area; G^* is the normalized scale amplitude; and ψ is a material property constant. With the normalized variables, equation (5.16) can now be rewritten as

$$V^*=(1+3\mu^2)^{1/2}A_r^*\left[K_e-(K_e-K_p)\left(\frac{D}{(2-D)A_r^*}\frac{G^{*2}}{\psi^{2/(D-1)}}\right)^{(2-D)/2}\right] \quad (5.18)$$

We call this the fractal geometry model of wear prediction. With

(5.18) the wear rate V^* can be evaluated as a function of A_r^*, D, G^*, and ψ.

If the area of the largest contact spot S_L is less than the critical area of plastic deformation, i.e., $S_L < S_c$, then only plastic deformation will take place. In that case $K_e = 0$ in (5.18).

5.4.1 Effect of Fractal Dimension on Wear Rate

The effect of fractal dimension on wear rate is a major concern. To numerically investigate how V* is affected by D using equation (5.18), the values of other parameters need to be chosen. Based on the literature (Archard 1980; Majumdar and Bhushan 1990; Stolarski 1990) and the experimental results presented in chapter 4, for ordinary cases the parameter values are chosen as $G^*=10^{-9}$, $\psi=0.01$, $\mu=0.2$, $K_e=10^{-4}$, $K_p=0.1$. Log(V*) is plotted against $\log(A_r^*)$ in Figure 5-1 for various D values. It can be seen that there are two regions of D that have significantly different wear rate behavior. In the first region, for D between 1.15 and 1.5, V* decreases with increasing D. In the second region, for D between 1.6 and 1.9, V* increases slightly

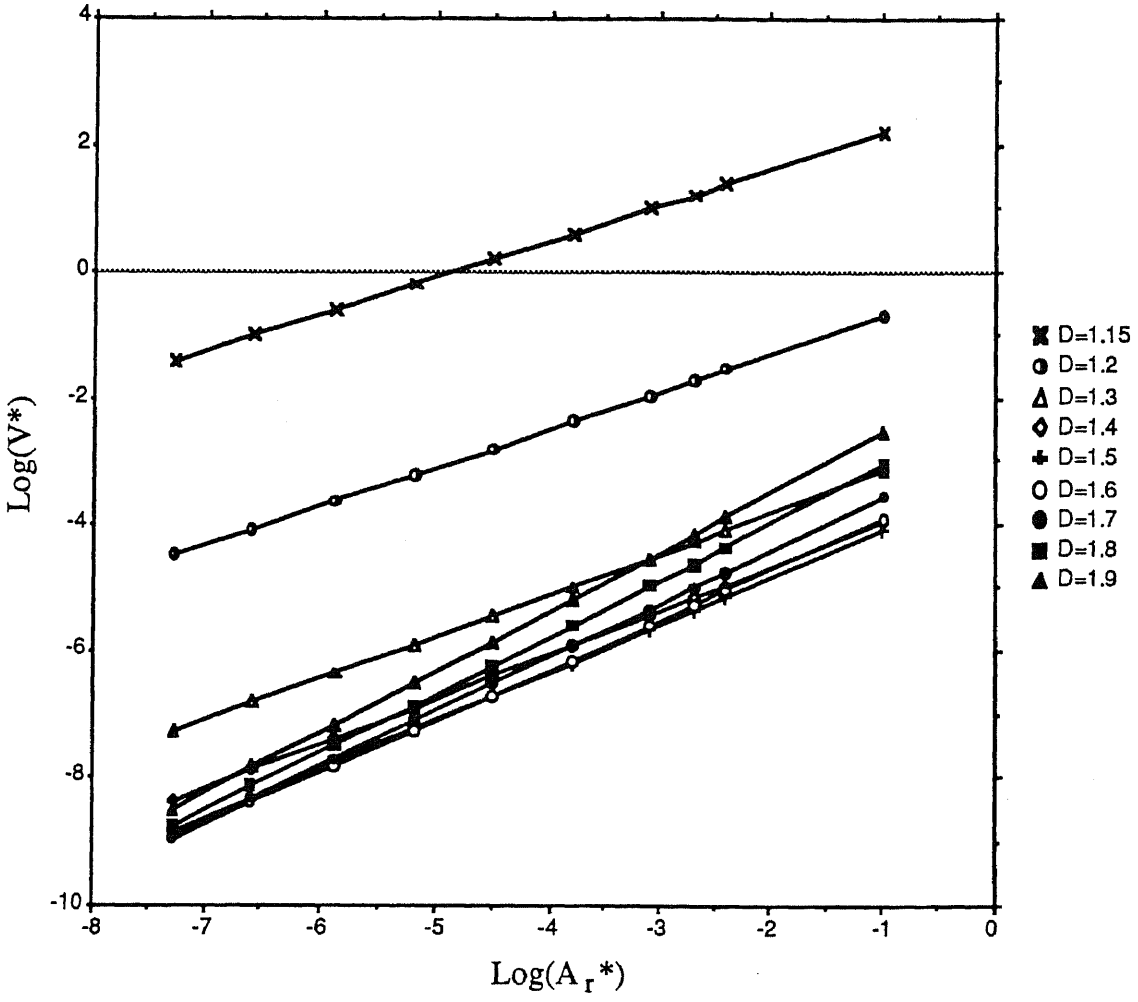

Figure 5-1 Effect of fractal dimension (D) and normalized contact area (A_r*) on normalized wear rate (V*)

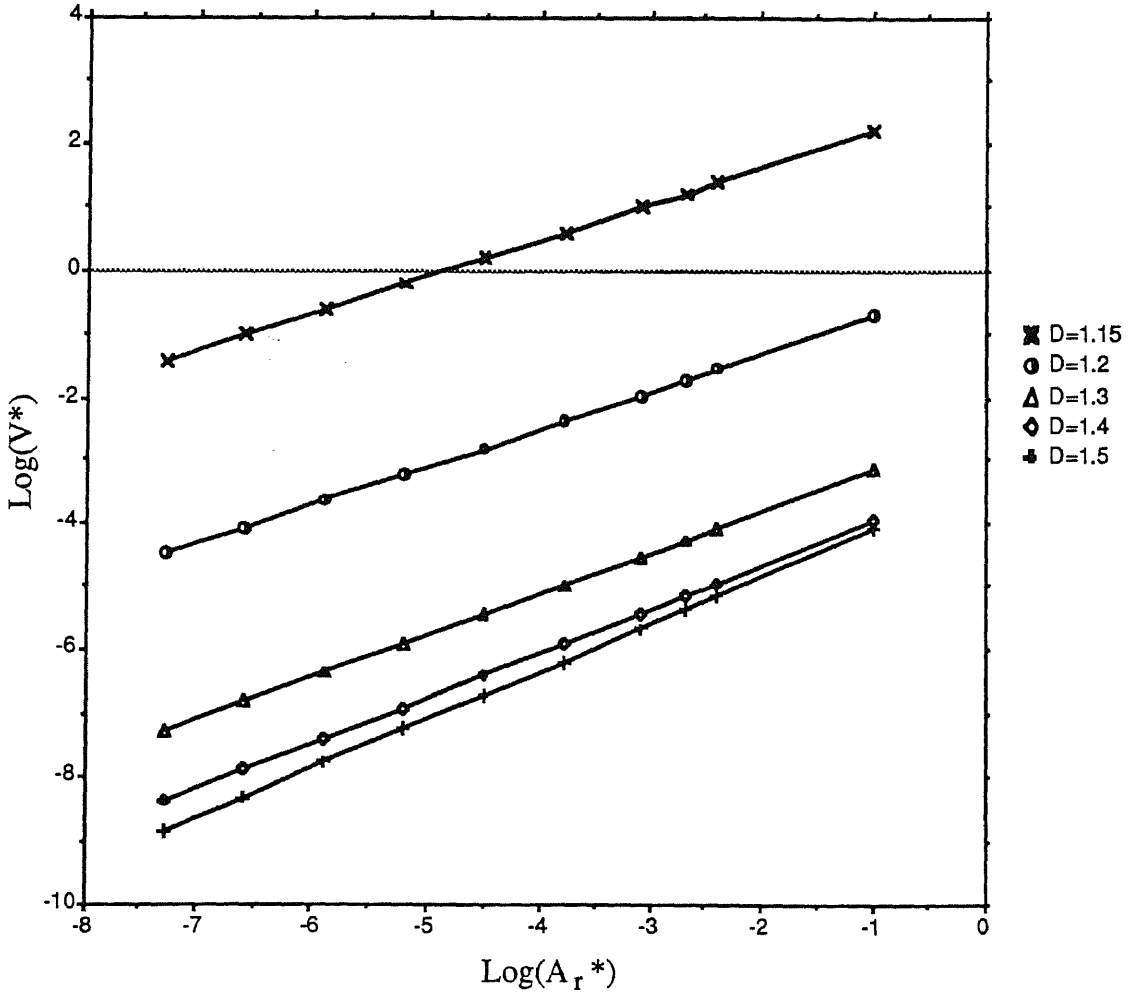

Figure 5-2 The V^*-A_r^* relation for the first range of fractal dimension D: 1.15-1.5

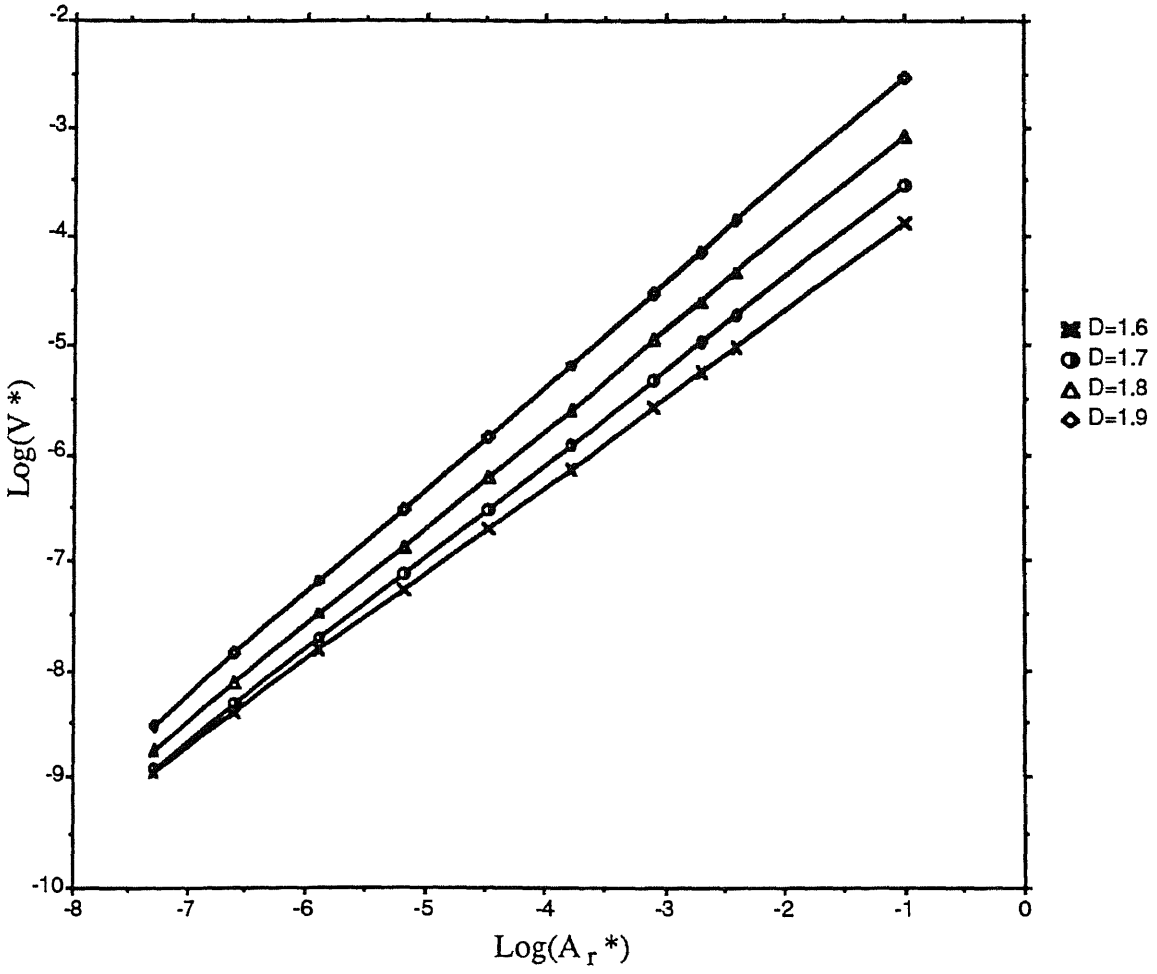

Figure 5-3 The V^*-A_r^* relation for the second range of fractal dimension D: 1.6-1.9

with increasing D. To show this more clearly, the relations in these two regions are plotted separately in Figures 5-2 and 5-3. Figure 5-2 shows that when D increases V* decreases and that this relationship is nonlinear. When D increases from 1.15 to 1.2, an increase of D by only 0.05, V* decreases by an average of 3.2 decades for the range of A_r^* considered. When D increases from 1.2 to 1.3, V* decreases by 2.5 decades. As D increases from 1.3 to 1.4 and from 1.4 to 1.5, the decreases in V* are 1.2 and 0.5 decades, respectively. Figure 5-3 shows that V* increases with increasing D for the range of D between 1.6 and 1.9. This wear rate behavior in the two fractal dimension regions can be explained as follows. When D increases between 1.15 and 1.5, the corresponding bearing area curve will shift higher. This means that there is a larger area involved in the surface contact. Under the same load, the normal contact pressure between the contact surfaces decreases with increasing D, thus the wear rate becomes smaller. When D increases between 1.6 and 1.9, the number of asperities per unit surface area increases and accordingly the tips of the asperities become sharper and weaker. Therefore, despite the fact that the normal contact pressure decreases with increasing D, this results in a larger wear rate.

The above observations can be summarized as follows: For fractal surfaces with $D<1.5$ the surface contact support ability is a dominant character of the wear process; but when $D>1.6$ other factors such as the sharpness of asperities may emerge to exert more influence on the wear rate. It should be noted that the value of D that distinguishes the two regions of wear rate behavior may vary

for different wear parameter values. For example, the D value is about 1.7 for the wear material and process described in Section 5.6.

5.4.2 Dependence of Wear Rate on True Contact Area Under Static Loading

From Figure 5-1, it can be seen that for every D, V* increases exponentially with A_r^*, since each plot is a straight line on the log-log graph. In Archard's equation, the wear rate ($V_r = \frac{V}{d}$) is proportional to the true contact area under static loading, i.e., $V_r \propto A_r$. As he (1980) pointed out, this relationship was based on the assumption that all deformations are plastic and that the asperities are isolated. On the other hand, if all deformations are elastic and the asperities are isolated, the wear rate should satisfy the relation $V_r \propto (A_r)^{2/3}$ (see Archard 1980). If deformations are mixtures of elastic and plastic deformations and the asperities are not isolated, the wear rate can be expected to have the relation $V_r \propto (A_r)^q$, where q is an undetermined constant which is related to the surface topography.

In the wear prediction model (5.16), we have included both elastic and plastic deformations. It is possible to use this equation to predict the power q in the relation $V_r \propto (A_r)^q$. Rewrite equation (5.16) as follows:

$$V_r \propto [K_e A_r - j(K_e - K_p)(A_r)^{D/2}] \tag{5.19}$$

where

$$j = \left(\frac{D}{(2-D)} \frac{G^2}{(Q\sigma_y/2E)^{2/(D-1)}}\right)^{(2-D)/2} \tag{5.20}$$

For a typical case encountered in engineering practice, D=1.5, $G=10^{-7}$ m, $Q\sigma_y/2E=0.001$ (for steel material), $K_e=10^{-4}$, and $K_p=0.1$, then j=0.42 and equation (5.19) can be estimated as

$$V_r \propto [10^{-4}A_r - 0.42\ 10^{-4}(A_r)^{D/2}] + 0.042(A_r)^{D/2} = (A_r)^{m(D)} \quad (5.21)$$

or

$$V_r \propto (A_r)^{m(D)} \quad (5.22)$$

where $m(D) \approx D/2$ (note that the other items of A_r in (5.21) are extremely small) is a monotonically increasing function of D and has a value approximately between 0.5 (when D=1) and 1 (when D=2). Once the fractal dimension of a surface is given, m(D) can be determined as a value between 0.5 and 1. By checking the slope of log(V*) versus $\log(A_r^*)$ for each D in Figure 5-1, it is found that these slopes are between 0.6 (when D=1.15) and 0.94 (when D=1.9). These slopes match with our estimation in (5.22). Additional confirmation of this fractal power proportionality can be found in the experimental results provided by Archard (1953) about 'wear rate over load graphs for brass and stellite pins rubbing on tool steel rings'. Because in the adhesive wear theory the true contact area has the relation with the normal load as $A_r \propto W$, these experimental results also can be used to detect the relation between wear rate and true contact area. Based on these experimental results, for brass material the relation is $V_r \propto (A_r)^{0.98}$, and for stellite $V_r \propto (A_r)^{0.92}$. This is consistent with our predicted fractional power proportionality. These data support the validity of our model, and in

so doing, demonstrate the role which fractal geometry can play in the analysis of wear processes.

5.4.3 Effect of Other Parameters on Wear Rate

The effect of the scale amplitude on wear rate predicted by our model can be observed from Figure 5-4. When G* increases from 10^{-12} to 10^{-6} (with D fixed at 1.5 and the other parameters having the same values as before), V* increases monotonically with G*. This is due to the fact that a larger surface scale amplitude leads to greater plastic deformation wear.

The effect of the material constant ψ on V* is shown in Figure 5-5. It can be seen that V* decreases with increasing ψ (between 0.0001 and 1). This can be explained by the fact that the hardness of material increases with increasing ψ.

5.5 Optimum Fractal Dimensions of Wear Processes

For a surface in a wear process, the most important requirement is low wear rate. Fractal dimension has been shown to be related to surface contact support ability and wear rate via our model discussed above. The fractal dimension of the lowest wear rate is of considerable significance in any wear process. The optimum fractal dimension can be found by differentiating (5.18) with respect to D and setting it to 0, i.e.

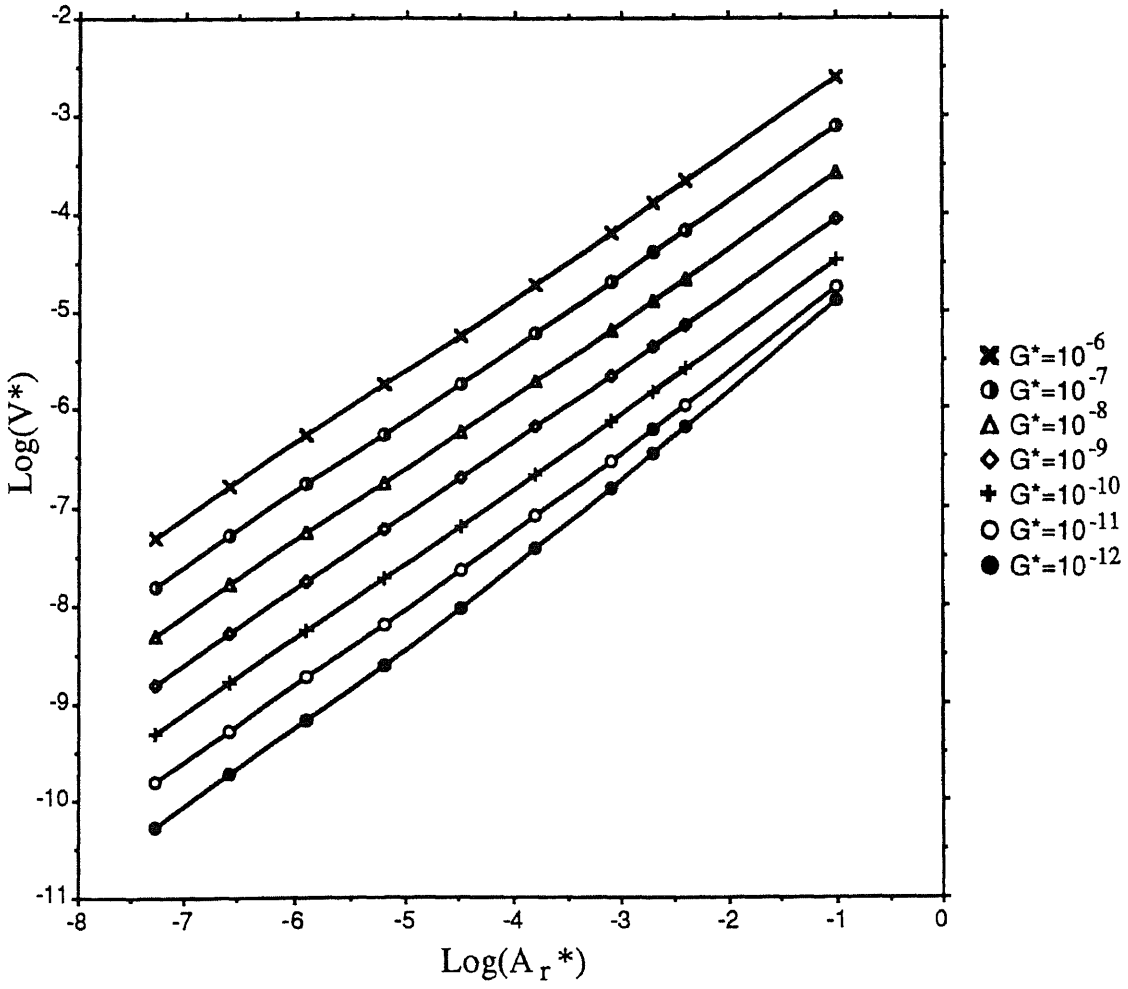

Figure 5-4 Effect of scale amplitude G* on normalized wear rate (V*)

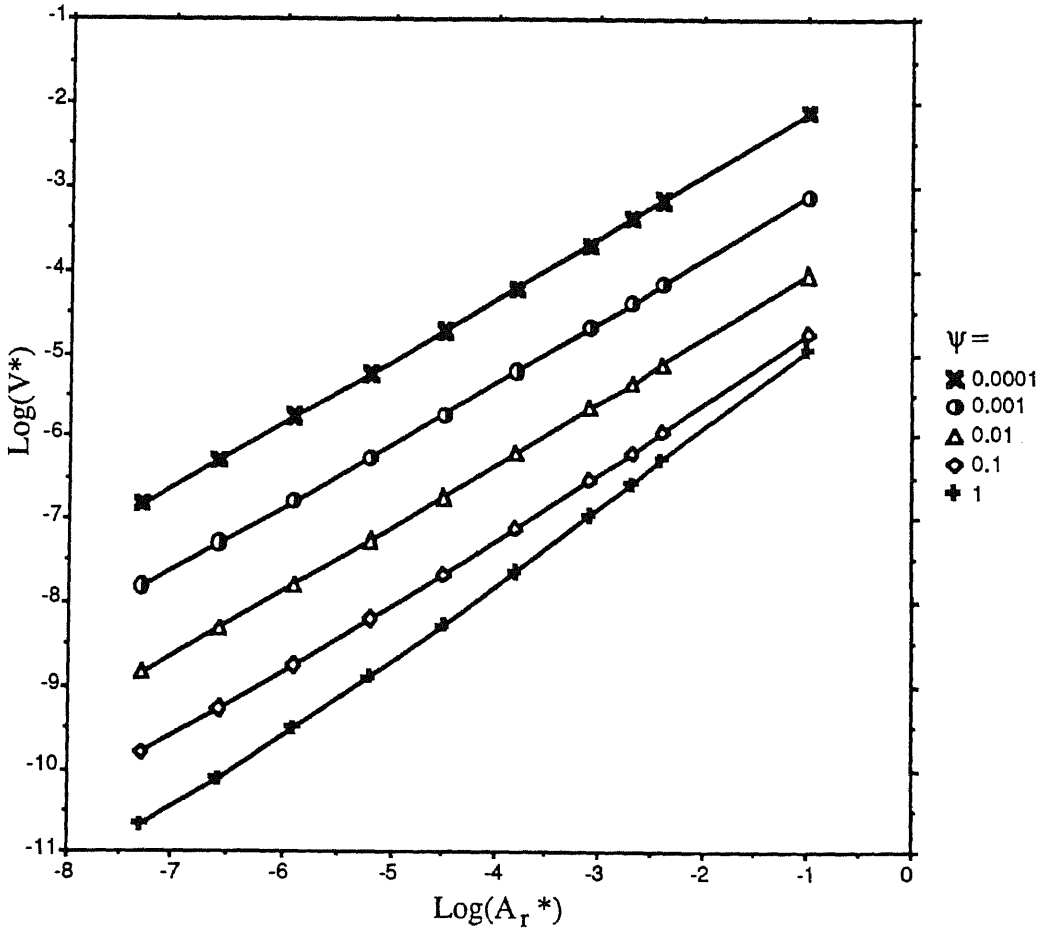

Figure 5-5 Effect of material constant ψ on normalized wear rate (V*)

$$\frac{dV^*}{dD} = (1+3\mu^2)^{1/2} A_r^* (K_p - K_e)\left[\frac{D\, G^{*2}}{(2-D) A_r^* \psi^{2/(D-1)}}\right]^{(2-D)/2}$$
$$\left\{\frac{1}{2}\ln\left[\left(\frac{2-D}{D}\right)\left(\frac{A_r^*}{G^{*2}}\right)\psi^{2(2D-1)/(D-1)^2}\right] + \frac{1}{D}\right\} = 0 \qquad (5.23)$$

From our prior discussions there exist $A_r^* \neq 0$, $K_p \neq K_e$, $G^* \neq 0$ and $1<D<2$, so equation (5.23) leads to

$$\frac{1}{2}\ln\left[\left(\frac{2-D}{D}\right)\left(\frac{A_r^*}{G^{*2}}\right)\psi^{2(2D-1)/(D-1)^2}\right] + \frac{1}{D} = 0 \qquad (5.24)$$

This is a non-linear equation, and solutions for D are functions of three variables: $D = F(A_r^*, \psi, G^*)$. Thus we see that the optimum fractal dimension depends on the true contact area, material property constant, and scale amplitude.

Let us look more closely at (5.23) and (5.24). First, we observe that solving (5.24) for D is equivalent to solving

$$D = \phi(D) = (R^*)^{-1}(2-D)\, e^{2/D}\, \psi^{2(2D-1)/(D-1)^2} \qquad (5.25)$$

where $R^* = G^{*2}/A_r^*$ and e is the base of the natural logarithm. It is easy to see that ϕ is a strictly decreasing function of D on the interval $1< D \leq 2$ such that $\phi(2) = 0$ and $\phi(D) \rightarrow \infty$ as D approaches 1. We conclude, therefore, that (5.25) has a unique solution, say $D = D_m$, in the interval $1 < D \leq 2$ which corresponds to the intersection of the line $y = D$ with the curve $y = \phi(D)$.

Referring back to (5.23), it can be readily shown that $\frac{dV^*}{dD} < 0$

for $1< D< D_m$ and $\frac{dV^*}{dD} > 0$ when $D_m < D \leq 2$. Hence, the minimum value of V^* on $1 < D \leq 2$ is attained at $D = D_m$, so D_m is the optimum value of the fractal dimension. Since it is not possible to obtain a closed form solution of (5.25), it is necessary to use numerical methods to obtain values of D_m.

For finding the optimum dimension D for various A_r^*, Figure 5-6 is obtained by replotting Figure 5-1. It can be seen from this figure that for different A_r^* the optimum D's are different, but they all are roughly in the range 1.45-1.55. The effect of the material constant ψ on the optimum dimension can be found by comparing Figures 5-6, 5-7 and 5-8 which have values of ψ equal to 0.01, 0.1, and 0.001, respectively. In Figure 5-7 (ψ = 0.1), the optimum values of D for the various A_r^* are in the range 1.33-1.4. In Figure 5-8 (ψ = 0.001), the optimum dimensions are in the range 1.58-1.71. All three figures show the same tendency of D as A_r^* decreases from 0.5 to 10^{-6}: the optimum D shifts to a higher value as A_r^* decreases. Also, the figures show that the value of optimal D decreases as ψ increases.

The influence of G^* on optimum dimension can be seen by comparing Figures 5-6, 5-9, and 5-10. The optimum D values are around 1.5, 1.55, and 1.45 for the G^* values of 10^{-9}, 10^{-8}, and 10^{-10}, respectively. The value of D increases as G* increases.

5.6 Implementation in Wear Testing

In this section the wear testing results are presented to qualitatively support the fractal model for wear prediction. In our

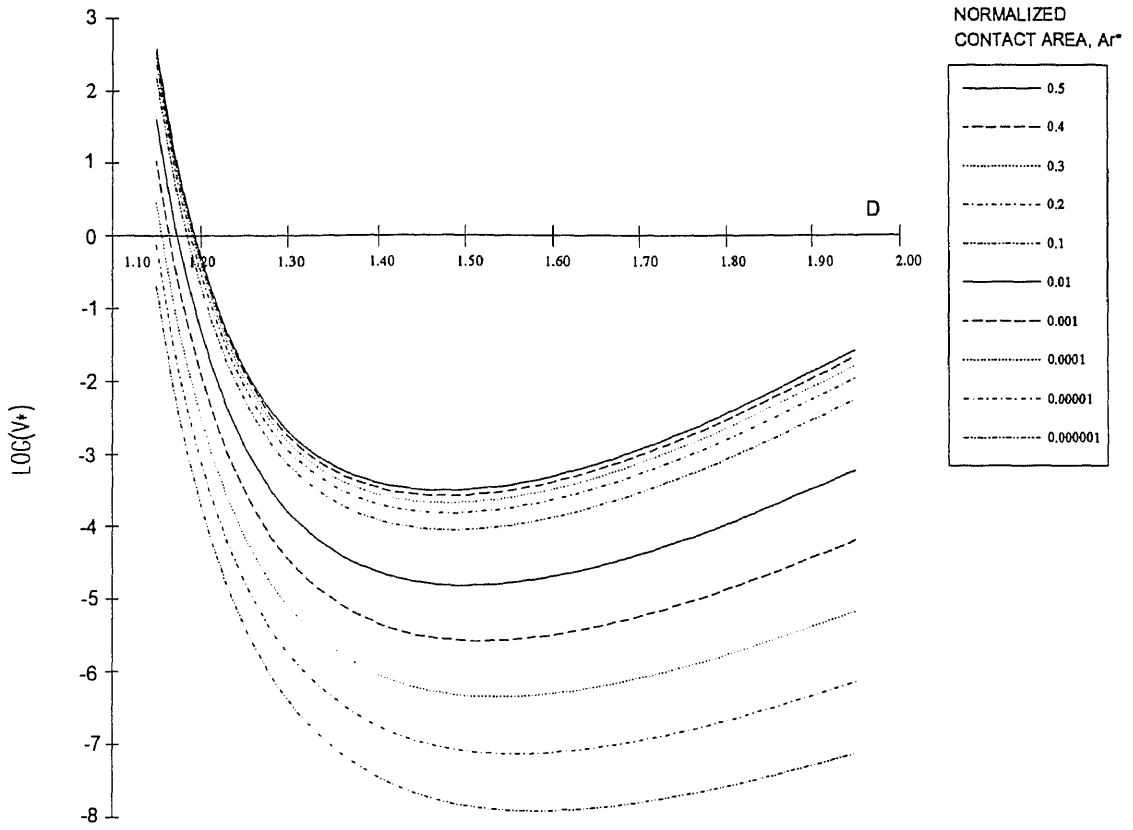

Figure 5-6 Relation of normalized wear rate (V*) to fractal dimension (D) with $\psi = 0.01$, $G^* = 10^{-9}$, and various values of A_r^*

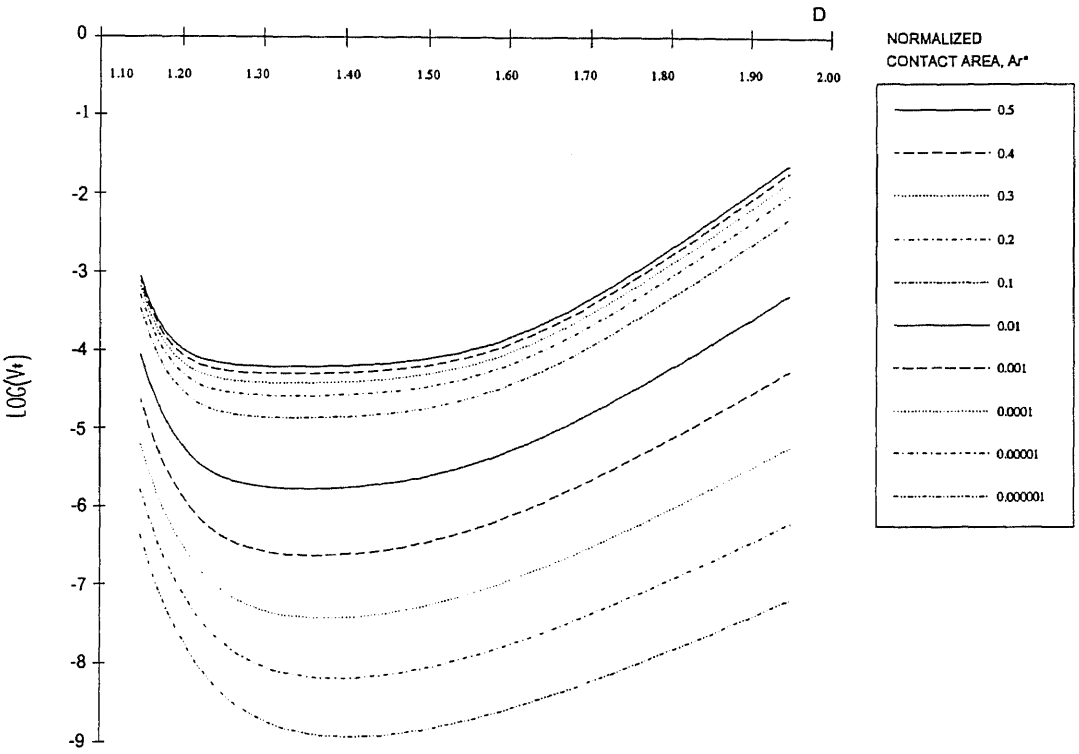

Figure 5-7 Relation of normalized wear rate (V*) to fractal dimension (D) with $\psi = 0.1$, $G^* = 10^{-9}$, and various values of A_r^*

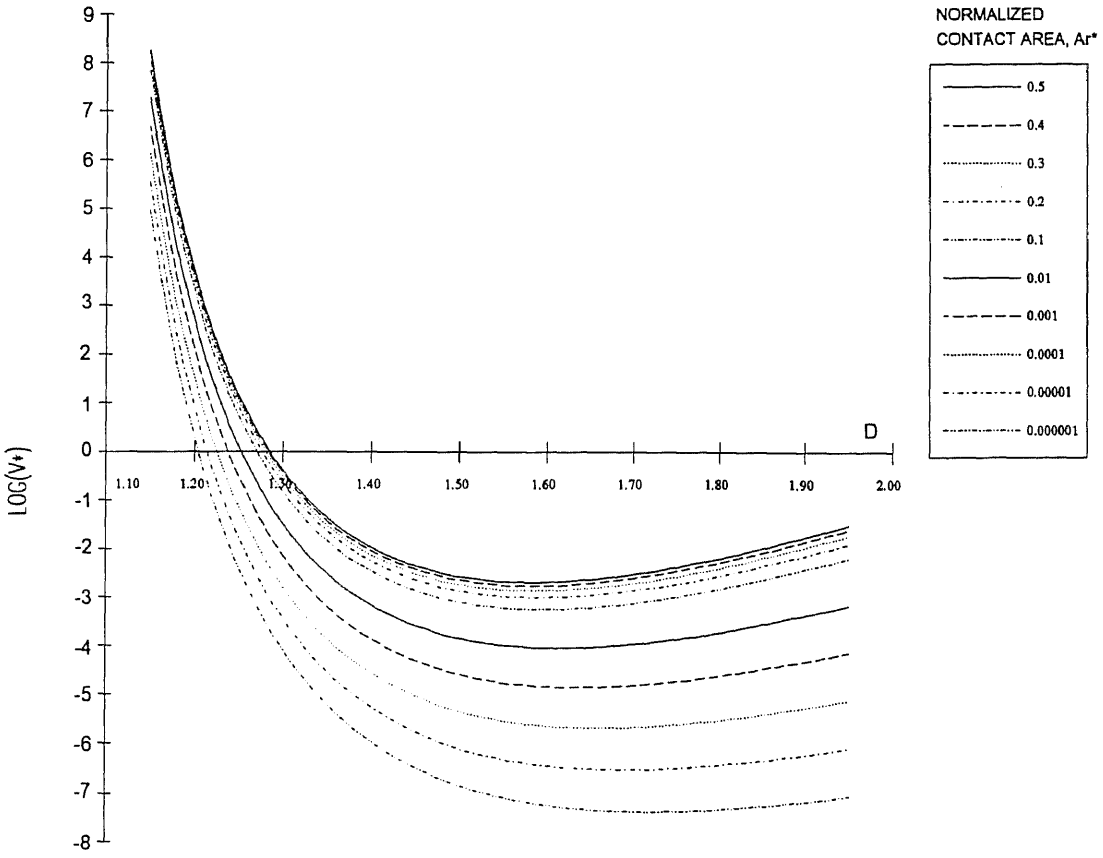

Figure 5-8 Relation of normalized wear rate (V*) to fractal dimension (D) with $\psi = 0.001$, $G^* = 10^{-9}$, and various values of A_r^*

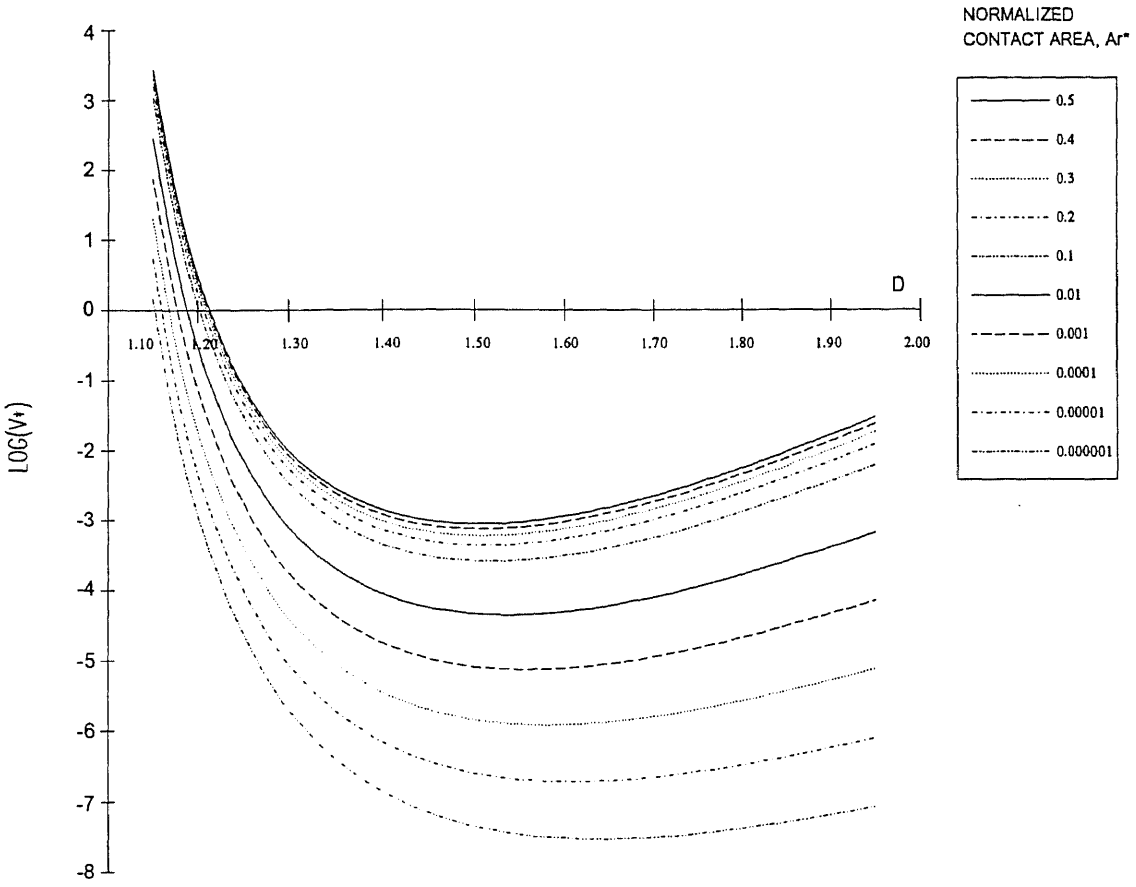

Figure 5-9 Relation of normalized wear rate (V*) to fractal dimension (D) with $G^* = 10^{-8}$, $\psi = 0.01$, and various values of A_r^*

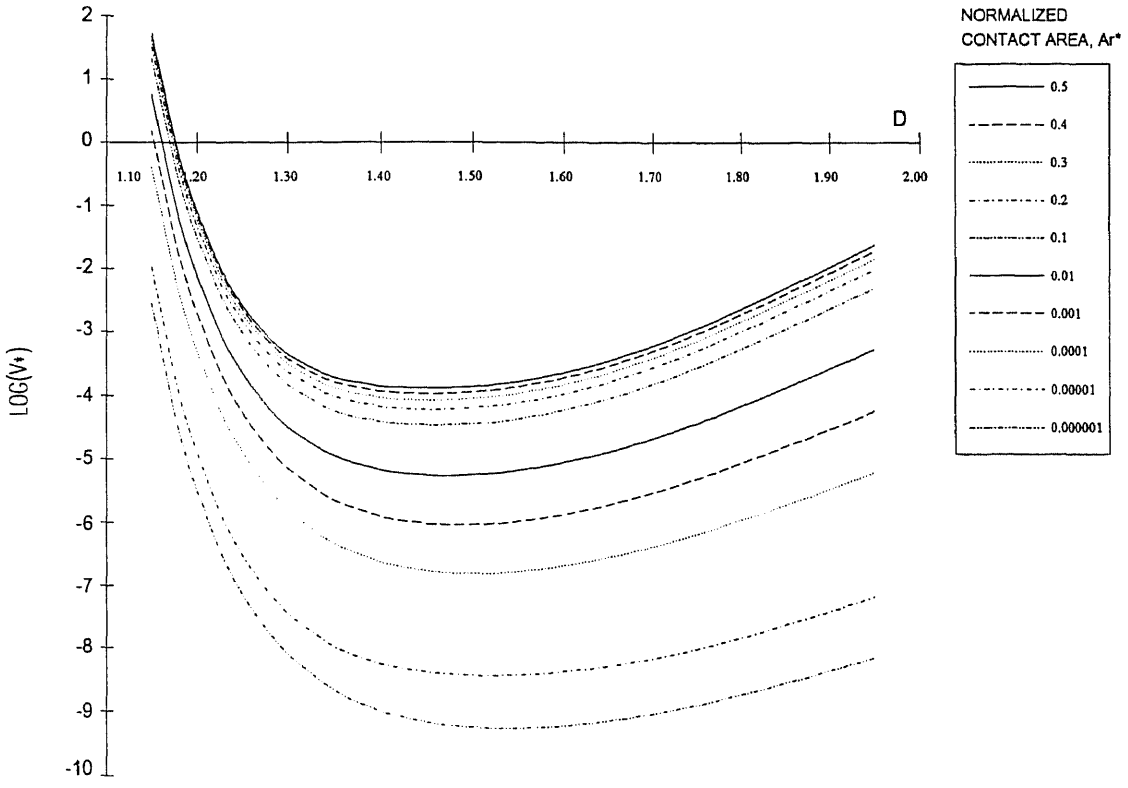

Figure 5-10 Relation of normalized wear rate (V*) to fractal dimension (D) with $G^* = 10^{-10}$, $\psi = 0.01$, and various values of A_r^*

wear testing experiments the wear mechanism (Dubrovsky and Shih 1988) consisted of an alloy steel roller (rotating part) and an ion-nitriding treated shoe (fixed part). When the testing was performed, a load was exerted on the mating surfaces and the wear rate was measured periodically. During the wear process the fractal dimensions of the roller and shoe were obtained using the method of surface topography measurement described in (Zhou, Leu and Dong 1990). The fractal dimensions of four pairs of rollers and shoes were calculated in the experiments and they had very similar values.

The histogram of the wear rate from one of our experiments is shown in Figure 5-11. It can be seen from the figure that during the first 30 minutes of testing the wear rate was fairly high, and then decreased and stayed at a very low rate until 120 minutes had elapsed; after this time the wear rate increased dramatically. These observed changes of wear rate are consistent with the well-known three stages of a wear process: run-in, mild wear, and severe wear and they can be explained as follows. At the beginning of the wear process the two contact surfaces were fresh and they had very sharp peaks. When they interacted with each other, the sharp layers were worn off gradually. So in this stage (the run-in stage) the wear rate was a little higher than that in the subsequent stage. After the first stage the surfaces became smoother and thus had a larger contact area and a smaller contact stress. This resulted in a stable and very low wear rate. This is the second stage (the mild wear stage) which was between 30 and 120 minutes. The third stage (the severe wear stage) existed after 120 minutes. In this stage there existed large shear and normal stresses on the contact surfaces because of

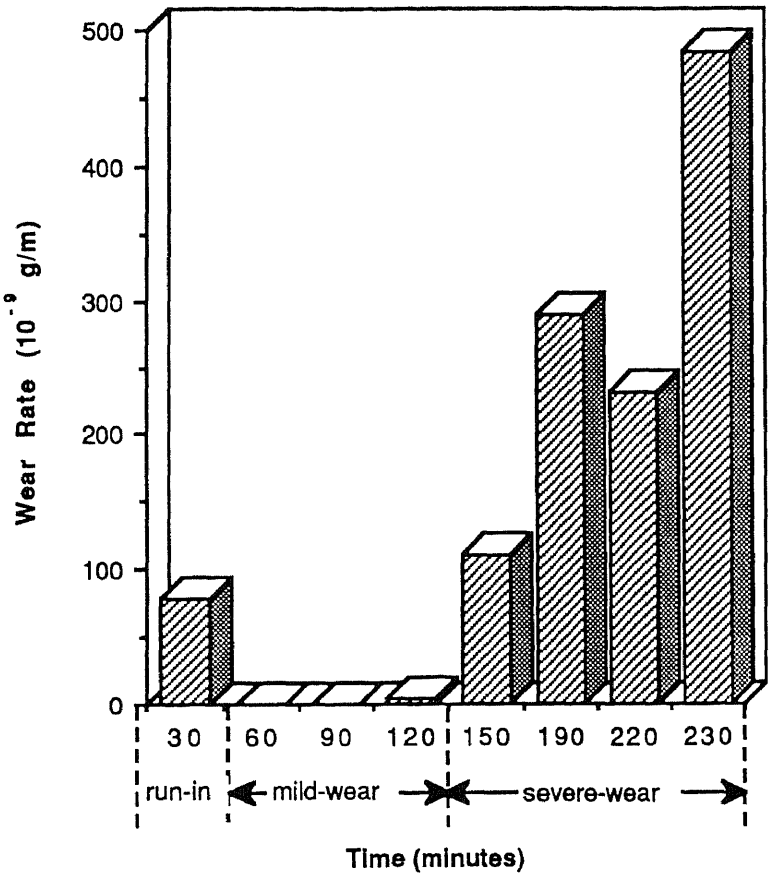

Figure 5-11 The three stages of wear rate

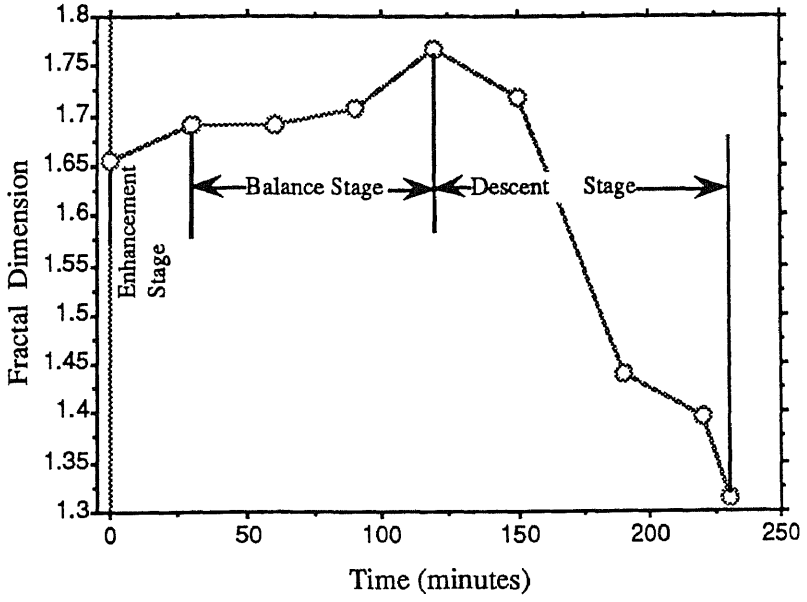

(a)

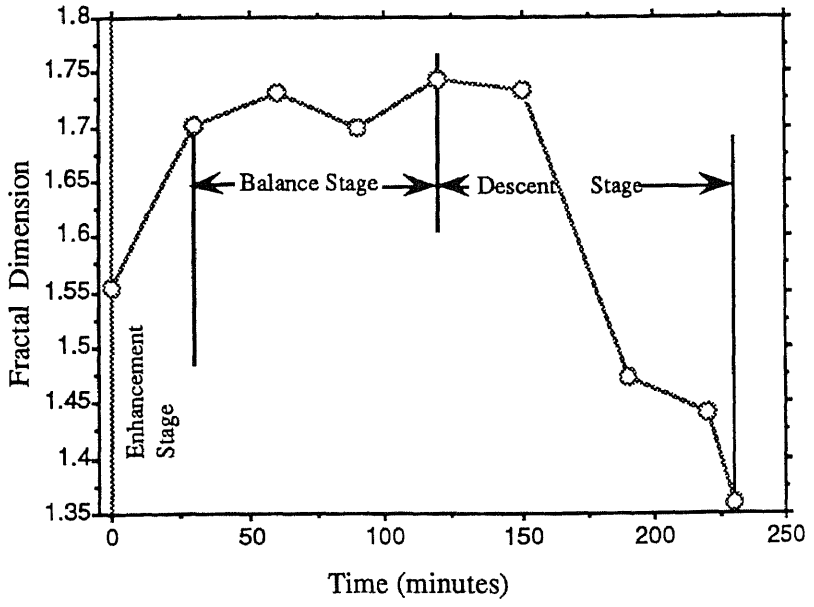

(b)

Figure 5-12 Three stages of variations in the fractal dimensions of (a) roller and (b) shoe

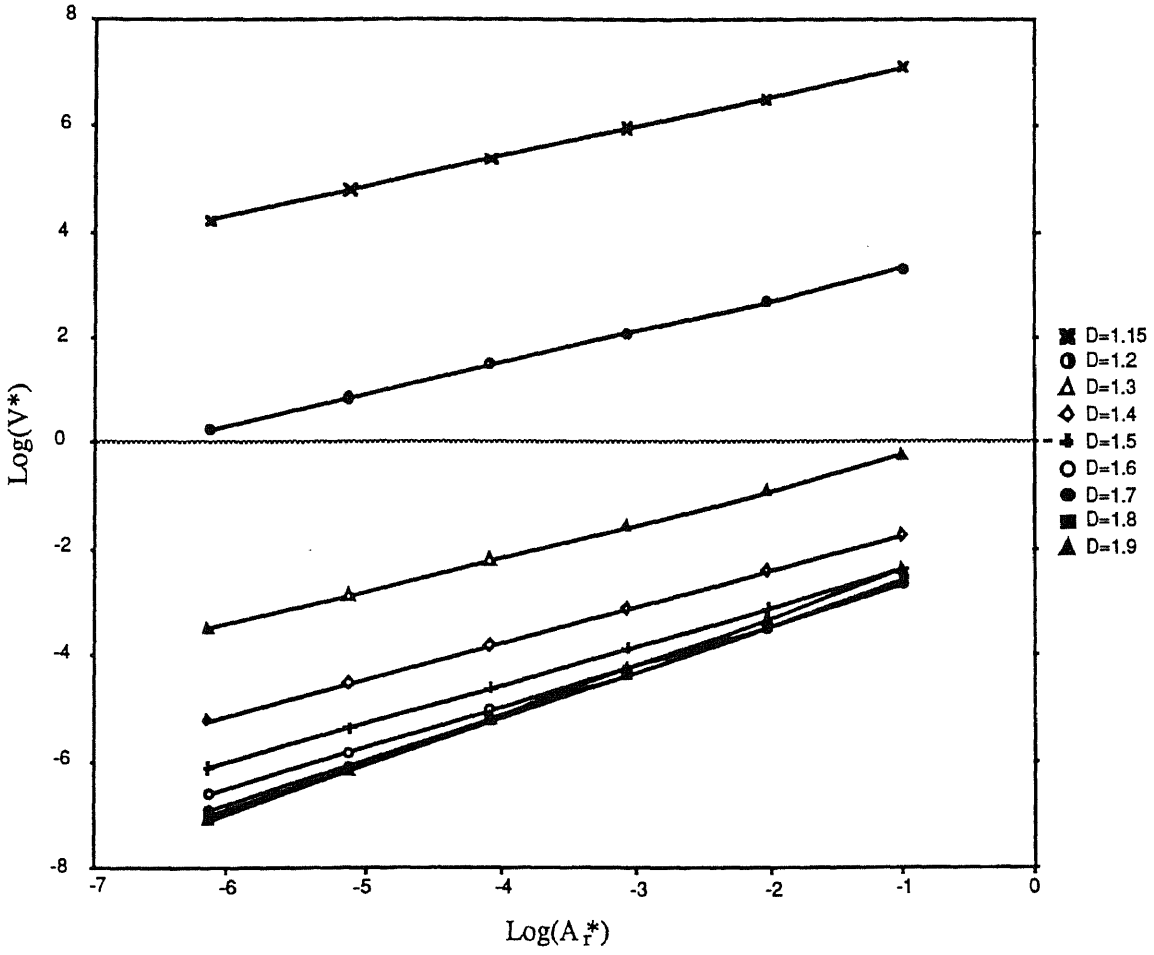

Figure 5-13 The model result based on experimental determined parameters.

thermal, molecular, and physical actions. The surfaces became rougher and rougher, and this led to a significant increase in wear rate as the process continued.

The changes of fractal dimensions associated with the above testing are given in Figure 5-12 (a) and (b) for the roller and shoe, respectively. During the first 30 minutes, the fractal dimensions increased from their initial values. This is referred to as the enhancement stage of fractal dimension in the figure. Apparently when the surfaces first came into contact, the fresh and sharp layers of surfaces were removed; the surfaces became smoother and the surface contact support ability increased. After this stage, from the 30th to the 120th minute, D increased slightly but maintained an overall balance. This is referred to as the balance stage of fractal dimension. From the 120th minute, D decreased greatly as the process continued. This is called the descent stage of fractal dimensions. This clearly implies that the contact support ability of the surfaces become poorer and poorer because the surfaces become rougher and rougher. Comparing Figure 5-11 with Figure 5-12 we see that the three stages of wear rate correlate with the three stages of fractal dimension very well. This suggests that fractal dimension can be used to monitor the wear process. The same observations hold for the other three pairs of wear components.

From our wear testing processes some parameter values for the roller were obtained as follows: μ=0.06, ψ=0.0034, $G^*=65\times10^{-9}$ (average value of the whole process), $K_e=10^{-4}$, and K_p=0.1. For examining the validity of our model, the obtained parameter values of the wear testing are substituted into equation (5.18) and the wear

prediction graph is plotted in Figure 5-13. From the figure it can be seen that the optimum fractal dimension for this specific wear process is around 1.7. This implies that D=1.7 is a change point of wear rate, i.e. if D is less than 1.7, V* decreases with D increasing, and if D is larger than 1.7, V* increases with D decreasing. By using the result in Figure 5-13, the fractal dimension behavior of the roller in Figure 5-12 (a) can be explained according to the following observations. At the first 30 minutes because D is less than 1.7, when D increases from 1.65 to 1.69 V* should decrease. From the 30th to 120th minute because D≈1.7, V* keeps the lowest rate. Between 120 and 230 minutes because D is either higher than 1.7 (from the 120th to 150th minute) or far lower than 1.7 (from the 150th to 230th minute), V* should increase. This prediction analysis which is based on the fractal dimension behavior matches fairly well with the wear rate histogram in Figure 5-11. It should be noticed that the wear prediction model does not account for the temperature increasing and resulted material property changes during the wear process, so it is possible to have some variance between the prediction and practical result.

5.7 Chapter Conclusions

It has been shown in this chapter that fractal geometry can be used to analyze wear processes. The fractal geometry model for wear prediction leads to results which are consistent with experimental observations. Using this model it has been found that there are two regions of D which have different wear rate behavior. In the first region as D increases, for example from 1.15 to 1.5 in Figure 5-1, the

wear rate will decrease greatly, and in the second region as D increases, for example from 1.6 to 1.9 in Figure 5-1, the wear rate will increase slightly. We have explained these phenomena by using surface contact support ability and sharpness of asperities. In addition, the model predicts that the wear rate increases monotonically as scale amplitude G increases or as material constant ψ decreases. Since there is a direct relation between G and topothesy L, the model provides a convenient means for using the fractal parameters D and L to predict wear rates.

Based on the model we have found that there is a relationship between wear rate and true contact area under static loading as $V_r \propto (A_r)^{m(D)}$, with m(D) between 0.5 and 1. This estimation is consistent with Archard's proposed relations of $V_r \propto A_r$ for purely plastic deformation and $V_r \propto (A_r)^{2/3}$ for purely elastic deformation. Our model gives a general and practical expression for V_r and A_r in terms of surface fractal properties.

The optimum fractal dimension, corresponding to a minimum wear rate in a wear process, is derived by using the wear prediction model. It has been found that the optimum fractal dimension is determined by A_r, ψ, and G. In ordinary cases a surface used in engineering practice has an optimum fractal dimension around 1.5, and this value shifts with changes in the three key parameters. When the A_r or ψ increases the optimum D decreases, but when G increases the optimum D increases. This optimum fractal dimension study provides useful information about how to prepare surfaces for wear reduction.

The results of wear testing tend to support our wear prediction

model which leads to the conclusion that our fractal approach has considerable potential for the analysis of wear.

CHAPTER 6
CONCLUSIONS AND FUTURE WORK

6.1 Conclusions

Two methods for surface characterization were studied in this thesis. The conventional method using statistical and random-process techniques was successfully used in classification, identification, and evaluation of AWJ machined surfaces. It was found that the smooth zone of waterjet cut surface has a random, moderately isotropic texture, with the height distribution near Gaussian. With this method the relations between AWJ cutting process parameters and surface roughness were also obtained, which shows that for the smooth zone, surface roughness increases slowly with increase in cutting speed, and it has negligible dependence on depth of cut; for the striation zone, however, surface roughness increases rapidly with increase in cutting speed or depth of cut. Power spectral analysis was used to study the mechanism of striation formation on AWJ cut surfaces. It was found that vibration of machine structure is the main cause of striation in the AWJ system. These results indicate that statistical and random-process techniques are, in general, suitable for identification, evaluation, and comparison of surface topographies.

The conventional method has some shortcomings because it uses a stationary random process to analyze a non-stationary, non-differentiable, and multi-scale surface profile. This may result in errors in the quantitative evaluation of surfaces. Fractal geometry, as a new method, can overcome the shortcomings of the conventional method. In the thesis a Gaussian fractal model for surface

characterization was developed. Based on this model, the relation between the fractal geometry method and the conventional method was revealed through the use of bearing area curve to characterize a surface. It is found that the bearing area curve shifts higher as fractal dimension (D) increases or topothesy (L) decreases. This relation reveals that fractal geometry can be used to characterize the contact support ability of a surface effectively. This led to our subsequent development of using fractal geometry for wear modeling and prediction. By using our wear prediction model it has been found that there are two regions of D which have different wear rate behavior. In one region wear rate decreases greatly with increasing D, and in the second region wear rate increases slightly with increasing D. Based on the model the relationship between wear rate and true contact area was found as $V_r \propto (A_r)^{m(D)}$, with m(D) between 0.5 and 1. The optimum (lowest wear rate) fractal dimension is derived by using the model. It shows that the optimum fractal dimension is only determined by three parameters, A_r, ψ, and G.

Although two different methods have been studied and some shortcomings of the conventional method are mentioned in the text, one should not jump to the conclusion that fractal geometry method will completely replace conventional method in the near future. Fractal geometry apparently has some advantages over conventional method and greater potential comparing with conventional method, but it is in its infant stages, and a lot of research work needs to be done in the future. Conventional method has been utilized for a long time and is widely understood and accepted as a major tool in

surface engineering research and applications. Chapter 2 of the thesis provides an example of the usefulness of the conventional method.

6.2 Future Work

As mentioned above, the fractal geometry is very efficient in the characterization of surface contact support ability, but in the evaluation of surface texture properties such as average surface height, slope, and curvature, up to now fractal geometry cannot provide effective parameters to characterize these properties. It is necessary to find some fractal parameters to represent these surface texture properties. According to the discussion of fractal dimension, topothesy, and ensemble variance in chapter 4, it is possible to relate L with surface average height, D with slope, and a combination of D and L with curvature. For doing this, a mathematical derivation and some experimental proofs need to be done.

In the Gaussian fractal model of surface topography discussed in chapter 4 of the thesis, a Gaussian distribution of surface height was assumed. But a real surface often has skewness, and is not a standard Gaussian distribution, thus a modified fractal model for surface topography needs to be considered. For doing this, a modified height distribution, for example t-distribution, can be used in derivation of the model equations.

In the fractal geometry model for wear prediction discussed in chapter 5, some dynamic factors such as changes of temperature, material properties, friction, and lubrication are not included in the model. For a quantitative prediction of wear rate, these factors must be considered. The possible way is introduce some dynamic

coefficients in the wear prediction model and then determine these coefficients by doing wear testings.

Fractal dimension is the most important aspect in fractal geometry. Finding practical means for computing the fractal dimension of a fractal set is still the subject ongoing study. The process of computing fractal dimension is often made more difficult by fluctuation and multi-stages on the log-log graph, and it is sometimes hard to find a unique value for fractal dimension. In the thesis, the structure function technique is introduced to calculate the fractal dimension, but in its log-log graph different stages of slopes still can be found. A technique that can identify which stage of slope is desired fractal dimension under consideration needs to be developed.

APPENDIX

An interesting fact about Gaussian nonisotropic surfaces is that only certain invariant combinations of the power spectra density (PSD) moments M_{pq} appear in the probability distributions of the surface statistics. Longuet-Higgins (1962) and then Nayak (1973) have shown that for $(p + q) \leq 4$, there are only seven such invariants. They are:

$$
\begin{aligned}
&I_1 = M_{00} ; \\
&I_2 = (M_{02} + M_{20}) ; \\
&I_3 = M_{20}M_{02} - M_{11}^2 ; \\
&I_4 = M_{40} + 2M_{22} + M_{04} ; \\
&I_5 = 2(M_{40}M_{04} - 4M_{13}M_{31} + 3M_{22}^2) ; \\
&I_6 = (M_{40} + M_{22})(M_{04} + M_{22}) - (M_{31} + M_{13})^2 ; \\
&I_7 = M_{40}(M_{22}M_{04} - M_{13}^2) - M_{31}(M_{31}M_{04} - M_{13}M_{22}) + M_{22}(M_{13}M_{31} - M_{22}^2)
\end{aligned}
\qquad \text{(A.1)}
$$

where the surface PSD moments, M_{pq}, are defined by

$$
M_{pq} = \int_{-\infty}^{\infty} \int_{-\infty}^{\infty} \Phi(k_x, k_y)\, k_x^p\, k_y^q\, dk_x dk_y \qquad \text{(A.2)}
$$

where k_x and k_y are frequency vectors in the X and Y directions, $\Phi(k_x, k_y)$ is the surface PSD, and p and q are positive integers. The quantities in eqn. (A.1) are invariants in the sense that they do not depend on the orientation of the X-Y axes, but this orientation

influences the functional form of $\Phi(k_x, k_y)$. A significant relationship between profile moments and surface moments has been derived, see (Nayak 1971); it has the following form

$$M_{n\theta} = M_{n0}\cos^n\theta + C_1^n M_{n-1,1}\cos^{n-1}\theta\sin\theta + \\ + C_2^n M_{n-2,2}\cos^{n-2}\theta\sin^2\theta + \ldots + M_{0n}\sin^n\theta \qquad (A.3)$$

where θ is the angle between measured direction and the X axis, $C_m^n = \frac{n!}{m!(n-m)!}$ and $M_{n\theta}$, the profile nth moment in the θ direction, can be defined as

$$M_{n\theta} = \int_{-\infty}^{\infty} \Phi(k) k^n dk \qquad (A.4)$$

where k is the profile frequency vector in the θ direction, $\Phi_\theta(k)$ is the profile PSD and n is a positive integer.

If we choose $\theta = 0$ in eqn. (A.3) from a profile measured on a Gaussian nonisotropic surface, the surface moment M_{00} can be obtained as

$$M_{00} = M_{0\theta} \qquad (A.5)$$

If three nonparallel profiles are measured in the θ_1, θ_2, and θ_3 directions, the following relation holds

$$\begin{pmatrix} M_{20} \\ M_{11} \\ M_{02} \end{pmatrix} = \begin{pmatrix} \cos^2\theta_1 & 2\cos\theta_1\sin\theta_1 & \sin^2\theta_1 \\ \cos^2\theta_2 & 2\cos\theta_2\sin\theta_2 & \sin^2\theta_2 \\ \cos^2\theta_3 & 2\cos\theta_3\sin\theta_3 & \sin^2\theta_3 \end{pmatrix} \begin{pmatrix} M_{2\theta 1} \\ M_{2\theta 2} \\ M_{2\theta 3} \end{pmatrix} \qquad (A.6)$$

If five nonparallel profiles are measured, the surface moments M_{40}, M_{31}, M_{22}, M_{13} and M_{04} can be calculated in the same manner. Hence the seven statistical invariants in expression (A.1) can be calculated with only five nonparallel profiles. For convenience in our derivation five special angles are chosen:

$\theta = 0, \pi/6, \pi/4, \pi/2$, and $3\pi/4$.

BIBLIOGRAPHY

Abbott, E. J., and F. A. Firestone, 1933. "Specifying Surface Quality." *Mech. Engng.* 55, pp. 569-572.

American National Standard. 1985. *Surface Texture (Surface Roughness, Waviness, and Lay),* ANSI/ASME B46.1-1985, The American Society of Mechanical Engineers.

Archard, J. F. 1953. "Contact and Rubbing of a Flat Surface." *Applied Physics.* Vol. 24, pp. 981-988.

—. 1980. "Wear Theory and Mechanics." in *Wear Control Handbook,* Edited by Peterson, M.B., and W.O. Winer, ASME, New York.

Avnir, D., D. Farin, and P. Pfeifer. 1984. "Molecular Fractal Surfaces." *Nature* Vol. 308, pp. 261-263.

—. 1985. "Surface Geometric Irregularity of Particulate Materials: The Fractal Approach." *Colloid and Interface Science.* Vol. 103, pp. 112-123.

Berry, M. V. 1979. "Diffractals." *Physics A.* Vol.12, pp. 781-797.

Berry, M. V., and Z.V. Lewis, 1980. "On the Weierstrass-Mandelbrot Fractal Function." *Proceedings of the Royal Society,* A Vol. 370, pp.459-484.

Chao, J., E. Geskin, and Y. Chung. 1992. "Investigations of the Dynamics of the Surface Topography Formation During Abrasive Waterjet Machining." *Proceedings of 11th International Conference on Jet Cutting Technology,* St. Andrews, Scotland, Sept. 8-10.

Dauw, D. F., C. A. Brown, J. Griethuysen, and J. Albert. 1990. "Surface Topography Investigations by Fractal Analysis of Spark-Eroded Electrically Conductive Ceramics." *Annals of the CIRP,* Vol. 39/1.

Dubrovsky, R., and I-Tsung Shih, 1988. "Development of the Computer Controlled Seizure Testing Methodology." *In New Materials Approach to Tribology: Theory and Applications, Materials Research Society Symposium Proceedings,* Vol. 140.

Falconer, K. 1990. *Fractal Geometry: Mathematical Fundations and Applications.* John Wiley & Sons.

Gagnepain, J. J., and C. Roques-Carmes, 1986. "Fractal Approach to Two-Dimensional and Three-Dimensional Surface Roughness." *Wear,* Vol. 109, pp. 119-126.

Geskin, E. S., W. L. Chen, S. S. Chen, F. Hu, M. E. H. Khan, S. Kim. 1989. "Investigation of Anatomy of an Abrasive Waterjet." *Proceedings of Fifth American Waterjet Conference.* pp. 217-230.

Goldberger, A. L., D. R. Rigney, and B. J. West, "Chaos and Fractals in Human Physiology." *Scientific Amarican,* February 1990, pp. 42-49.

Greenwood, J. A., and J. H. Tripp, 1970-71. "The Contact of Two Nominally Flat Rough Surfaces." *Proceedings of Institution of Mechanical Engineers.* Vol. 185, pp. 625-633.

Hashish, M. 1984. "A Modeling Study of Metal Cutting with Abrasive Waterjets." *Trans. of ASME, Journal of Engr. Materials and Technology.* Vol. 106, pp. 88-100.

—. 1988. "Visualization of the Abrasive-Waterjet Cutting Process." *Experimental Mechanics.* pp. 159-169.

—. 1991. "Characteristics of Surfaces Machined with Abrasive-Waterjets." *ASME Journal of Engineering Materials and Technology.* Vol. 113, pp. 354-362.

—. 1992 "On the Modeling of Surface Waviness Produced by Abrasive Waterjets." *Proceedings of 11th International Conference on Jet Cutting Technology.* St. Andrews, Scotland, pp. 17-34.

Hunt, D. C., T. J. Kim, and M. Reuber. 1988. "Surface Finish Optimization for Abrasive Waterjet Cutting." *Proceedings of 9th International Symposium on Jet Cutting Technology,* Sendai, Japan, pp. 99-112.

ISO R468. 1966. *International Standard of Surface Roughness.*

Jordan, D. L., R. C. M. Hollins, and E. Jakeman. 1986 "Measurement

and Characterization of Multi-Scale Surfaces," *Wear*. 109, pp. 127-134.

Jost, H. P. 1990. "Tribology — Origin and Future." *Wear*. 136, pp. 1-17.

Kaye, B. H. 1986. "The Description of Two-Dimensional Rugged Boundaries in Fine Particle Science by Means of Fractal Dimensions." *Powder Technology*. 46, pp. 245-254.

—. 1989. *A Random Walk Through Fractal Dimensions*. VCH Verlagsgesellschaft, Weinheim, F.R.G., VCH Publishers, New York.

King, T. G., and Powell, J., (1986), "Laser-Cut Mild Steel-Factors Affecting Edge Quality," Wear, Vol. 109, pp. 135-144.

Korcak, J. 1938. "Deux Types Fondamentaux Dedistribution Statistique." *Bulletin de l'Institut International de Statistique*. III, pp. 295-299.

Kovacevic, R. 1991. "Surface Texture in Abrasive Waterjet Cutting." *Journal of Manufacturing Systems*, Vol. 10, No. 1, pp. 32-40.

Kruschov, M. M. 1957. "Resistance of Metals to Wear by Abrasion; Related to Hardness." *Institution of Mechanical Engineers, Conference of Lubrication and Wear*. London, pp. 655-659.

Kubo, M., and J. Peklenik. 1968. "An Analysis of Micro-Geometrical Isotropy for Random Surface Structures." *Annals of the C.I.R.P.* Vol. 16, pp. 235-242.

Ling, F. F. 1987. "Scaling Law for Contoured Length of Engineering Surfaces." *J. Appl. Phys.* Vol. 62(6), pp. 2570-2572.

—. 1990. "Fractals, Engineering Surfaces and Tribology." *Wear*. Vol. 136, pp. 141-156.

Longuet-Higgins, M. S. 1957. "The Statistical Analysis of a Random Moving Surface." *Phil. Trans. of the Royal Society*. Vol. A249, pp. 321-387.

Longuet-Higgins, M. S. 1962. "The Statistical Geometry of Random Surfaces." *in Hydrodynamic Stability, Proceedings of 13th Symposium on Applied Mathematics*. American Math. Society, pp. 105-143.

Majumdar, A. 1989. "Fractal Surfaces and Their Applications to Surface Phenomena." Dissertation University of California, Berkeley.

Majumdar, A., and B. Bhushan, 1990. "Role of Fractal Geometry in Roughness Characterization and Contact Mechanics of Surfaces." *ASME Journal of Tribology*. Vol. 112, pp. 205-216.

—. 1991. "Fractal Model of Elastic-Plastic Contact Between Rough Surfaces." *ASME Journal of Tribology*. Vol. 113, pp. 1-11.

Mandelbrot, B. 1967. "How Long Is the Coast of Britain? Statistical Self-Similarity and Fractional Dimension." *Science*. Vol. 155, pp.636-638.

Mandelbrot, B., and J. W. Van Ness. 1968. "Fractional Brownian Motions, Fractional Noises and Applications." *SIAM Review*. Vol. 10, No. 4, pp. 423-437.

Mandelbrot, B. 1982. *The Fractal Geometry of Nature*. Freeman, New York.

Mandelbrot, B., D. E. Passoja, and A. J. Paullay, 1984. "Fractal Character of Fracture Surfaces of Metals." *Nature* 308, pp. 721-722.

Mandelbrot, B. 1985. "Self-Affine Fractals and Fractal Dimension." *Physica Scripta*. Vol. 32, pp. 257-260.

Matsui, S., H. Matsumura, Y. Ikemoto, K. Tsujita, and H. Shimizu. 1990. " High Precision Cutting Method for Metallic Materials by Abrasive Waterjet." *10th. Int. Symp. on Jet Cutting Technology*. Amesterdam, paper no. G3.

McCool, J. I. 1987. "Relating Profile Instrument Measurements to the Functional Performance of Rough Surfaces." *ASME Journal of Tribology*. Vol. 109, pp. 264-271.

Nayak, P. R. 1971. "Random Process Model of Rough Surfaces." *ASME J. Lub. Tech.* Vol. 93F, pp. 398-407.

—. 1973. "Some Aspects of Surface Roughness Measurement." *Wear*. Vol. 26, pp. 165-174.

Neusen, K. F., P. K. Rohargi, C. Vaidyanathan, and D. Alberts. 1987. "Abrasive Waterjet Cutting of Metal Matrix Composites." *Proceedings of the 4th United States Waterjet Conference.* Berkeley, CA, pp. 175-182.

Peitgen, H. O., and D. Saupe. 1988. *The Science of Fractal Images.* Springer-Verlag, New York.

Peklenik, J. 1967. "Investigation of the Surface Typology." *Annals of the C.I.R.P.* Vol. 15, pp. 381-385.

Rice, S. O. 1944. "Mathematical Analysis of Random Noise." *Bell Syst. Tech.* J. 23, pp. 282-332. 1945. *Bell Syst. Tech.* J. 24, pp. 46-156.

Richardson, L. F. 1961 in *General Systems Yearbook* 6, Vol. 139.

Roques-Carmes, C., D. Wehbi, J. F. Quiniou, and C. Tricot. 1988. "Modelling Engineering Surfaces and Evaluating Their Non-integer Dimension for Application in Material Science." *Surface Topography.* Vol. 1, pp. 435-443.

Sayles, R.S ., and T. R. Thomas, 1978. "Surface Topography as a Non-stationary Random Process." *Nature* 271, pp. 431-434.

—. 1979. "Measurements of the Statistical Microgeometry of Engineering Surfaces." *ASME J. Lub. Tech.* Vol. 101, pp. 409-418.

Souda, V. 1991. "Implementation of an Integrated High Energy Beam Workcell." Master Thesis, New Jersey Institute of Technology, Newark, NJ.

Stolarski, T. A. 1990. "A Probabilistic Approach to Wear Prediction." *Journal of Physics, D: Applied Physics.* Vol. 24, pp. 1143-1149.

Sun, N. P. 1973. *Wear.* Vol.25, pp. 111-124.

Tabor D. 1959. "Junction Growth in Metallic Friction: The Role of Combined Stresses and Surface Contamination." *Proceedings of the Royal Society.* A251, pp. 378-389.

Tan, D. K. M. 1986. "A Model for the Surface Finish in Abrasive Waterjet Cutting." *Proceedings of 8th International Symposium*